Civil Engineering ETDs   Engineering ETDs

9-1-2015

Wellbore Microannulus Characterization and Seal Repair: Computational and Lab Scale Modeling

Steven Gomez

Follow this and additional works at: https://digitalrepository.unm.edu/ce_etds

Steven Gomez
Candidate

Civil Engineering
Department

This thesis is approved, and it is acceptable in quality and form for publication:

Approved by the Thesis Committee:

John Stormont, PhD, PE , Chairperson

Mahmoud Taha, PhD, PEng

Edward Matteo, PhD

Steve Sobolik, MSME

Wellbore Microannulus Characterization and Seal Repair: Computational and Lab Scale Modeling

by

Steven Paul Gomez

B.S., Civil Engineering, University of New Mexico, 2012

THESIS

Submitted in Partial Fulfillment of the

Requirements for the Degree of

Master of Science

Civil Engineering

The University of New Mexico

Albuquerque, New Mexico

July, 2015

Dedication

To an unparalleled network of family and friends who continually provide bountiful amounts of love, support, and positive energy.

"And, when you want something, all the universe conspires in helping you to achieve it." – Paulo Coelho, The Alchemist

Acknowledgments

The work of this thesis would have not been possible without the help and support of many individuals in my life.

To my committee, Dr. John Stormont, Dr. Ed Matteo, Mr. Steve Sobolik, and Dr. Mahmoud Reda Taha, your suggestions, assistance, and constructive criticism have allowed me to expand my field of knowledge and approach to identify problems. To my adviser, Dr. John Stormont, I thank you for the conglomeration of tools and opportunities I was fortunate enough to acquire along the way.

To the Sierra Solid Mechanics team and analysts including, but not limited to, Joe, Kendall, Mike, Nate, Mark(s), Gabriel, Jesse, Vicki, San, Pania and Jim. Your guidance, support, and bottomless supply of coffee has provided immeasurable benefits.

To my parents, Tess, Casey, and David, and my historic clan of McGough/-Gomez/Gadbury grandparents, aunts, uncles, and cousins for showing me that the world is full of unique people, places, and things all of which should be treated with a level of respect that you would like to receive in return. It goes without saying that your unconditional love and support has made it possible for me to be where I am today.

To my brothers and sister, David Matthew, Blake, and Brittany, who will continue to grow by my side, make a positive impact on those around them, and be brilliantly unique.[1]

To my long time partner Janea for being there for me day in, day out, from the moment I asked you to dance in 6th grade. The amount of love and encouragement you and your family have brought into my life often gave me motivation to push forward.

To my friends and classmates for hitting the books or enjoying life with me until we hit a wall.

To my mother Tess and grandmother Sofia for teaching me respect and selflessness.

---

[1]To Tommy and Harry, who were really cool.

Wellbore Microannulus

Characterization and Seal Repair: Computational and Lab Scale Modeling

by

Steven Paul Gomez

B.S., Civil Engineering, University of New Mexico, 2012

M.S., Civil Engineering, University of New Mexico, 2015

Abstract

Subsurface geologic formations used for extracting resources such as oil and gas can subsequently be used as a storage reservoir for the common greenhouse gas CO_2, a concept known as Carbon Capture and Storage (CCS). Pre-existing wellbores penetrate the reservoirs where supercritical CO_2 is to be injected. These wellbores can potentially be a pathway for contamination if CO_2 leaks through wellbore flaws to an overlying aquifer or the atmosphere. Characterizing wellbore integrity and providing zonal isolation by repairing these wellbore flaws is of critical importance to the long-term isolation of CO_2 and success of CCS.

This research aims to characterize the microannulus region of the cement sheath-steel casing interface in terms of its compressibility and permeability, as well as understand the mechanical behavior of a flaw upon repairing it with an epoxy nano-composite material. Numerical models are used to analyze stress and displacement

conditions along the casing-cement interface. These numerical results provide excellent agreement with closed-form elastic solutions. Models with flaws of varying dimensions along the casing-cement interface were then developed to describe the microannulus region. The mechanical response of the microannulus region is studied under flawed and repaired conditions; repair materials including an epoxy repair material and cement. A joint model is used to describe the hydraulic aperture of the microannulus region, whose mechanical stiffness is altered in response to the imposed stress state across the joint interface. The aperture-stress behavior is based upon laboratory measurements of hydraulic aperture (interpreted from flow measurements) as a function of imposed stress conditions.

This investigation found that the epoxy wellbore seal-repair material exhibits a mechanical response desired in the behavior of a flawed wellbore repair material, that microannulus permeability can satisfactorily be described by a joint model, and that the constitutive model imposed in a numerical simulation can play a significant role in the solution behavior and agreement to experimental data. Recommendations for future work include an application of the joint model with a thermally active large-scale reservoir coupled with pore pressure caused by dynamic CO_2 injection and subsequent microannulus region affects.

Contents

Contents

Contents

Contents

List of Figures

List of Figures

xvi

List of Tables

Chapter 1

Problem Statement

1.1 Introduction

This work is directed toward one of the key challenges in geological storage of CO_2, wellbore seal integrity. Under ideal conditions a low-permeability cement sheath is perfectly bonded to the casing and formation and provides an effective barrier against potential hydrocarbon leakage into aquifers or release on the surface (Bois et al., 2012). The integrity of high-pressure high-temperature (HPHT) oil and gas wells can be compromised in numerous ways as shown in figure 1.1. The potential for flow along the interface of the steel casing and cement sheath is the focus of this research.
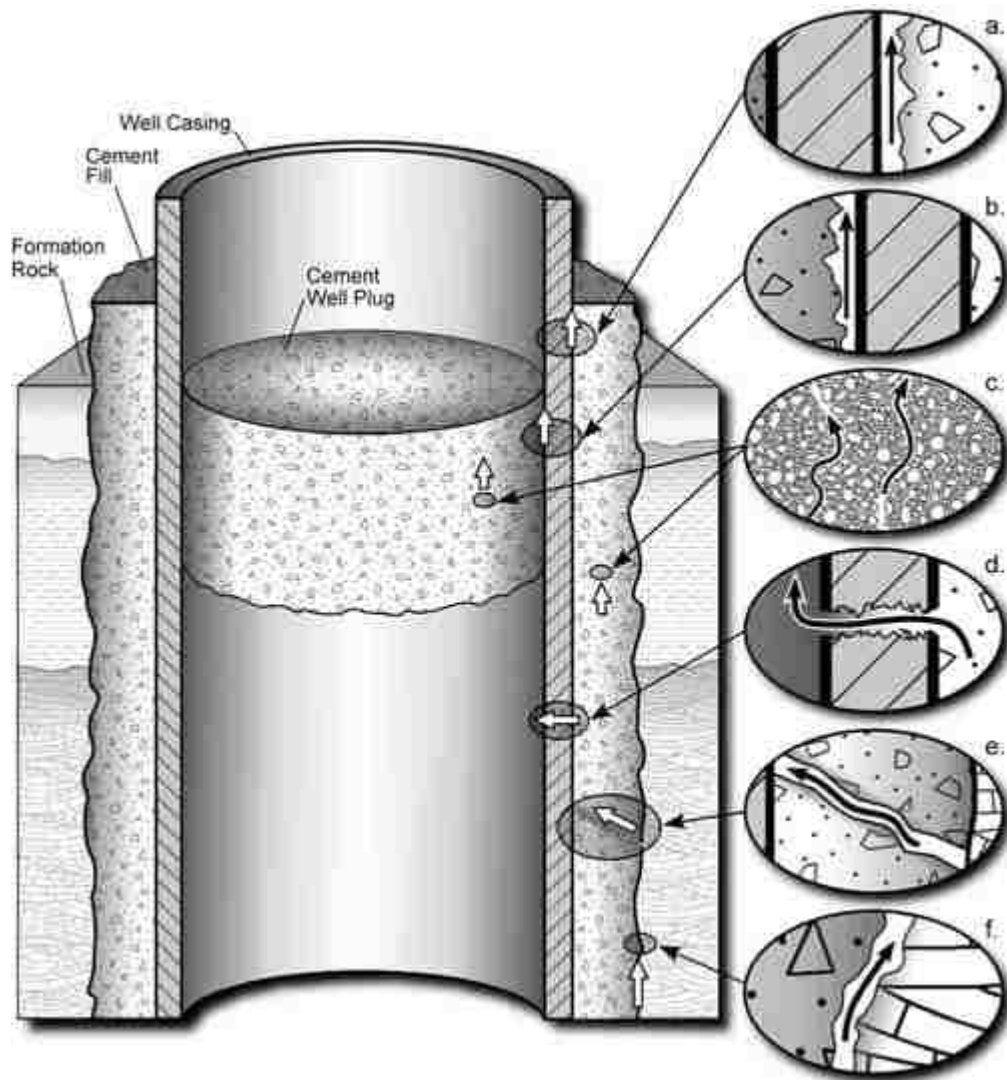
Figure 1.1: Wellbore leakage pathways of concern: (a) and (b) between cement and casing, (c) through the cement, (d) through the casing, (e) through fractures, and (f) between cement and formation (Gasda et al., 2004)

Factors that can cause flaws in wellbore systems include load combinations from imposed tectonic and mechanical operating stresses, thermal fluctuations presented by both fluid injection and in-situ temperatures, fluid injection induced pore pressure changes in the reservoir, varying mechanical properties of the casing and cement sheath, and bond integrity between surfaces of the wellbore (Carey et al., 2013; Bois

et al., 2012). These loading conditions can effect wellbore integrity in isolation or simultaneously, resulting in a complex framework of scenarios where zonal isolation can be lost.

To repair existing wells that leak, new composite materials are being developed. These composite materials utilize nanomaterials to achieve properties and behavior appropriate for the environment expected for wellbores that penetrate geological formations used for CO_2 storage. This research utilizes bench top experiments of a laboratory scale wellbore and Finite Element Method (FEM) computational techniques to better understand how a flawed wellbore mechanically behaves and the effectiveness of the proposed repair material to seal a flaw.

1.2 Research Scope

This research is directed at characterizing and modeling the compressibility and permeability of wellbore microannuli at the cement-casing interface. The following actions are undertaken to accomplish this:

1. Evaluate the significance of material parameters on the behavior of a laboratory scale wellbore test configuration through closed-form solutions and various numerical models. The focus of these studies is on stresses and displacement of casing-cement interface and epoxy repair material.

2. Implement a model for the microannulus that utilizes a mechanical stiffness that is consistent with the hydraulic aperture changes of microannuli measured in laboratory tests; the stiffness is described as a function of the normal stress acting on the microannulus elements.

1.2.1   Approach

The first task is to develop a computational model representative of a laboratory wellbore bench top experiment. The model is evaluated both by comparing numerical results with closed form analytical solutions from the published literature, as well as by comparison with laboratory measurements wellbore behavior. Also, the cement material model used in portions of this study is verified to the stress-strain response under uni-axial compression presented in literature.

This verified and validated laboratory wellbore model serves as a benchmark to determine the mechanical response of a laboratory wellbore system with a microannulus. Parametric studies are conducted to analyze models implementing perfect bonds, friction, varying flaw types, confining pressure, internal pressure, varying casing thicknesses, and varying constitutive material models. The development of a benchmark via a finite element model will assist in predicting the stress between a steel casing and cemented wellbore.

The development of a continuum model containing a wellbore microannulus will allow the comparison of laboratory test specimens with an explicit microannulus. The analytically predicted hydraulic aperture of a uniformly open wellbore microannulus when subjected to internal and external pressure boundary conditions is compared to the hydraulic aperture interpreted from flow measurements, suggesting if the hydraulic aperture is due to a truly open microannulus. Elements that define the stiffness behavior of the microannulus joint are inserted into the flawed region and compared to the hydraulic aperture.

Chapter 2

Background

2.1 Introduction

There are numerous methods being actively pursued to limit atmospheric levels CO_2, which are broadly categorized as efficiency and conservation, decarbonization of electricity and fuels, and natural sinks (Pacala and Socolow, 2004). Geological Carbon Dioxide Capture and Sequestration (CCS) is one emerging technology for reducing greenhouse gases in the atmosphere. Benson and Cole (2008) suggest that increasing CCS rates to a billion metric tons per year, 250 times the current rate, will be needed to achieve a perceptible reduction in levels of atmospheric CO_2. Although sufficient storage capacity is currently available (Litynski et al., 2006), there remain formidable challenges for CCS such as the significant amount of energy required to capture, process, and inject CO_2. Effective CO_2 sequestration requires ensuring leakage does not occur by maintaining the integrity of wellbores that connect with the storage formation. Inadequate wellbore performance with respect to its ability to provide isolation and containment of CO_2 could threaten water supplies, human

health, and introduce wellbore repair costs (Mainguy et al., 2007).

Wellbores typically have steel casing surrounded by a cement sheath intended to seal or isolate formations that the wellbore penetrates. Wellbore integrity is compromised by flaws that arise from a number of different causes, including inadequate cement-formation and cement-casing bonds, cement shrinkage, formation of a microannulus at the casing-cement interface, fracture formation within the cement, poorly emplaced cement, incomplete removal of drilling mud from casing prior to cementing, clay washouts at caprock interfaces, and others (Bois et al., 2012; Carey et al., 2013). The cement sheath is also susceptible to acid degradation introduced by carbonate brine flowing from the formation and either onto the bottom of the cement plug or into the annular space of the cement sheath-steel casing interface (Matteo and Scherer, 2012; Kutchko et al., 2007).

If the cement sheath becomes damaged, it is essential to evaluate the risks of potential leakage pathways that have developed (Bois et al., 2012). If warranted, repair of wellbore flaws may be required to establish a desired level of wellbore performance. Understanding the state of stress and strain in the wellbore system can be related to the expected permeability of the wellbore system as well as aid in understanding of the conditions that are encountered during repair of a leaky wellbore.

2.2 Wellbore Integrity

2.2.1 Importance to CO_2 sequestration

Wellbores that penetrate storage locations (as shown in figure 2.1) must maintain their integrity; that is they cannot be excessively leaky. If CO_2 leaks, the objective to

6
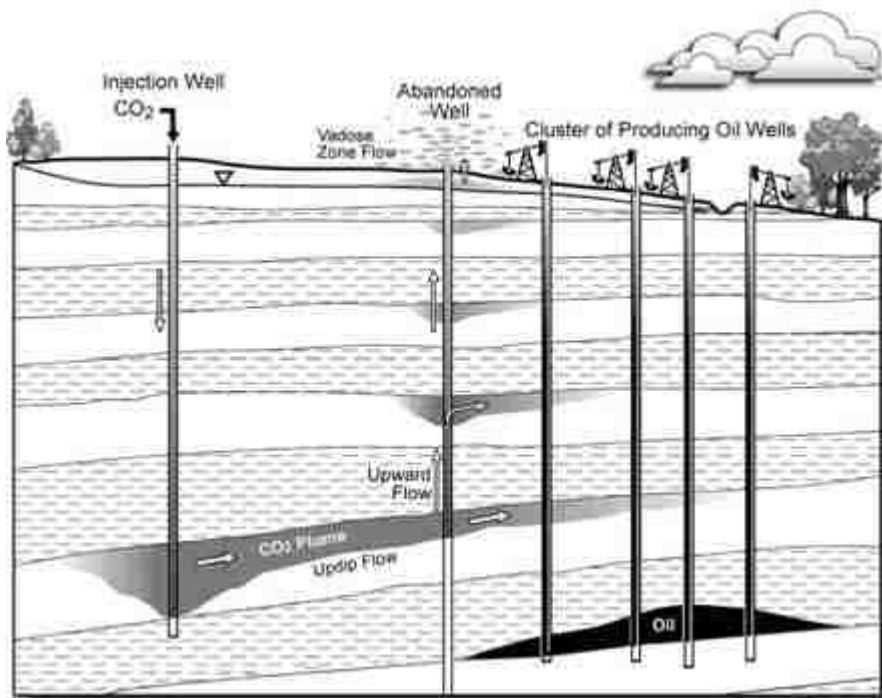
Figure 2.1: Schematic of injection, migration, and leakage along abandoned wells (Gasda et al., 2004).

mitigate CO_2 is plausibly made worse than if no attenuation efforts were performed. Studies performed by Kang et al. (2015) found that the number of abandoned wellbores in Pennsylvania range between 300,000 and 900,000. A random study was performed on 19 of these abandoned wellbores, all of which showed fluid leakage into the atmosphere. It was concluded that the level of methane leakage from abandoned wellbores could account for more than 10% of emissions caused by human activities in the state (Kang et al., 2015; Kang, 2014; Jackson, 2014).

Analytic solutions for single injection well and abandoned wellbore leakage rates have been expanded to characterize complex systems of multiple abandoned wells, aquifers, and aquitards (Nordbotten et al., 2004). These solutions can be applied to CO_2 injection problems of abandoned wellbores in layered stratigraphical systems,

7

where an increasing number of leaky wells surrounding an injection well is shown to cause a progressive reduction in the leakage per well. Nordbotten et al. (2005a) subsequently shows that the transport of CO_2 is dominated by viscous forces and CO_2 sequestration into saline aquifers can be modeled for cold, warm, deep, and shallow basins. These additional dependencies provide the capability to more accurately represent impaired wellbores affect on CCS facilities. Furthermore, Nordbotten et al. (2005b) expand the characterization of the sequestration process with analytic solutions that model the leakage pathways by which CO_2 travels from an injection plume and towards abandoned wells and into overlying aquifers over time, given suitable boundary conditions. Together, these models provide the means to model reservoir behavior when subjected to CO_2 injection at a high level analysis (e.g. policy). However, due necessary assumptions inherent in these models, including homogeneous rock formations and axisymmetric plume distributions, more accurate models are used for regulatory approval of a CCS operation. For example, the Nordbotten models would fail to capture an injection plume flowing in preferential pathways through highly heterogeneous rock formations.

Carey et al. (2013) modeled elevated pore pressure via CO_2 injection in computational simulations. These simulations of occured at a depth of 1000 m with a constant overburden pressure and formation confining stress of 25 MPa and 13 MPa respectively, where the minimum horizontal stress is proportion to half the overburden pressure. Carey et al. (2013) saw failure induced in the reservoir at $P_{inj} \geq 6MPa$; the fracture occurring at the orientation allowing maximum shear. Carey found that pressure is relieved in the injection reservoir with subsequent flow of water and/or CO_2 and that sequestration operations can cause failure along the wellbore. Shear failure is created by differential displacement of steel, cement, and caprock considered via Mohr-Coulomb slip criterion. Carey also concluded increasing cement cohesive strength causes slower failure propagation, a time dependent phe-

nomenon of the pressure relief upon failure (Carey et al., 2013). Further discussion is given in section 2.5 on this criterion's usage in numerical modeling.

2.2.2   Detection and Repair of Leaky Wells

Techniques have been developed to detect flaws in wellbore systems, as they can have significant consequence for reservoir production and zonal isolation. Some of the more common measuring devices include acoustic and ultrasonic sound technology of cement bond logs (CBLs) and variable density logs (VDLs). A CBL determines the integrity of the bond between the cement sheath and steel casing based on the attenuation of a signal amplitude that is transmitted through a casing section. The acoustic wave emitted by the transmitter is sent at 10 to 20 kHz (Bellabarba et al., 2008). Figure 2.2 illustrates how these ultrasonic imaging tools determine fracture aperture.

Sustained casing pressure (SCP) is a phenomena of increased casing pressures imposed by causes other than that of applied pressure or temperature fluctuation of the operator or artificial method. It is described that gas leakage can lead to SCP when a poor cement - formation or cement - casing bond is present (Rocha-Valadez et al., 2014). Horton et al. (2005) discusses a process to remediate SCP by injecting high density fluids at the top of an annulus which subsequently sink below lower density fluids that can be bled off. Horton describes this as a substitute method to the typical practice of injecting the annulus space with high density brine, where difficulties exist in accessing the annulus space for brine injection. Rusch et al. (2005) discusses a method which fixes SCP issues using Seal-Tite techniques; a differential pressure activated sealant consisting of a flexible polymer that is squeezed into the leak paths, where the sealant is allowed to cure. Rusch et al. (2005) described this
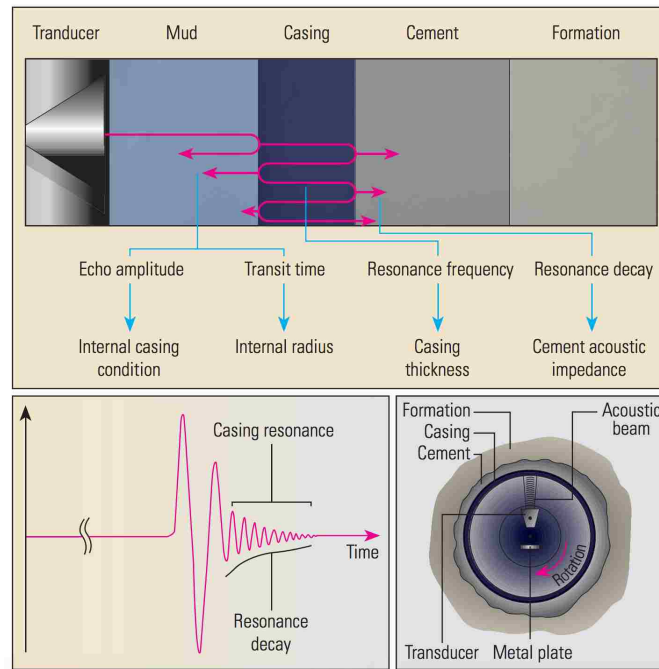
Figure 2.2: Principle of ultrasonic tools: Flaws are detected when resonance decay from an acoustic impedance extends over a long period, while good bonding results in a faster resonance decay (Bellabarba et al., 2008), (Illustration copyright Oilfield Review, used with permission of Schlumberger).

method applicable in repairing microannulus leaks, casing packers, and wellhead valves, amongst others.

In an effort to maintain the integrity of a wellbore throughout its lifetime, including re-entry into abandoned wellbores and dysfuncitonal producing wellbores, various methods are practiced to seal and repair the wellbore casing. A common repair method processes is described by Metcalf et al. (2009), where a smaller outer diameter casing is cemented inside of an existing wellbore space. Metcalf explains the disadvantages of this multi-stage process being that reduced flow during stimulation can manifest as a result of decreasing inner diameter, while poor cementing operations can lead to shortcomings as discussed in section 2.3.1. Running new casing can lead to excessive surge pressure, a displaced fluid effect due to moving pipe

inside the wellbore (PetroWiki, 2012a). This technique has potential to fracture the formation, hindering production rates of a producing wellbore or the integrity of an abandoned wellbore repair.

Rusch and Romano (2004) describes a method where polymer sealants are used to repair leaky pipes without reducing the internal pipe diameter. This is accomplished by method of pigs, which involves a tool that is run along the inside of the pipe for the purpose of cleaning, hydrostatic testing, or applying protective coating (PetroWiki, 2012b). Rusch and Romano (2004) used a pigging technique to develop a seal (using the developed poylymer) in the presence of a differential pressure. Disadvantages of this method include the possibility of losing a seal when the pipe is subjected to pigging operations (scraper or wiper), particularly when the pipe is corroded.

PetroWiki (2012c) describes squeezing as a process to repair damaged wellbore areas, where small to large cavities, including microannuli, are filled by forcing a cement slurry into their void space; various squeezing techniques include running, hesitation, high pressure, low-pressure (most common technique), packer, and bradenhead. PetroWiki discusses that void size, slurry quality, and fracturing pressure as some of the criteria evaluated to determine the repair process. Additionally, wellbore plugging is a method used in abandoned wellbores as means to provide zonal isolation to fluid-pathways, sometimes combined with the squeezing process. Wellbore plugging also has use in direction drilling, well control (i.e. lost circulation), and wellbore stability (PetroWiki, 2012c).

2.3   Nature of Wellbore Leakage

2.3.1   Types of Flaws

Flaws in a wellbore can take many forms including formation of a microannulus region at the casing-cement interface, formation of microannulus region at the formation-cement interface, channelization, an incomplete cementing job which can be particularly precarious between the formation and cement sheath, plastic deformation and failure in the cement sheath (Carey et al., 2013; Bois et al., 2012; Wang, 2014). If failure of the cement sheath occurs, preferential flow path can develop through a combination of these channels as shown by arrows in figure 2.3. When the flaws allow flow through the wellbore, zonal isolation is lost and the wellbore may no longer functions as intended.

(a) Debonding: Steel Annulus

(b) Debonding: Formation Annulus

(c) Radial cracking

(d) Bad Cement Pour

(e) Plastic Deformation, Shear Failure
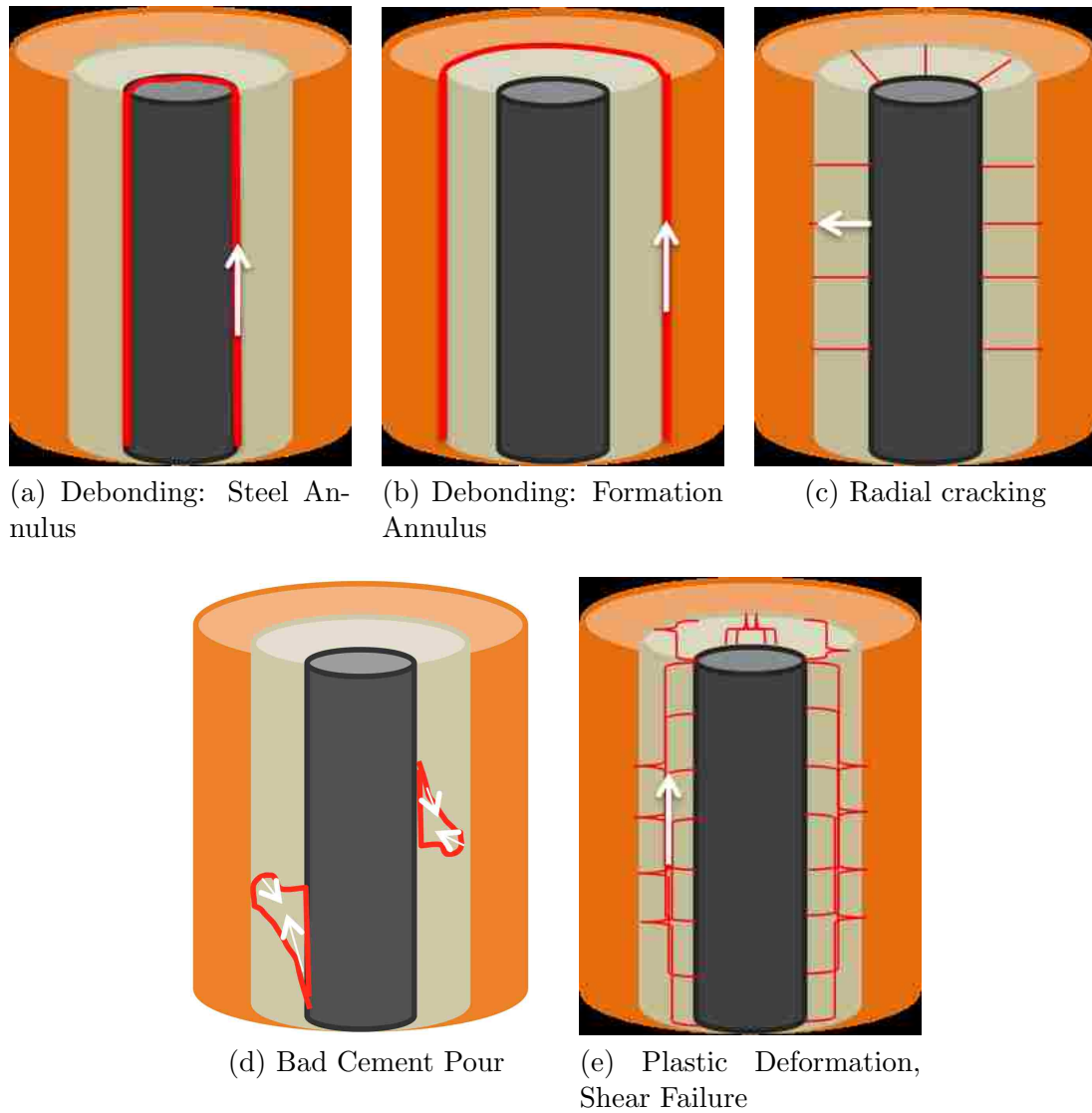
Figure 2.3: Wellbore failure modes and potential flow paths (indicated by arrows).

2.3.2   Causes of Flaws

Wellbore integrity starts with a well-constructed cement sheath. This requires proper cement property selection, cleaning of the wellbore, and successful placement of cement (Wang, 2014; Bellabarba et al., 2008).

Cement properties must be tailored for the particular conditions of the wellbore. Plastic deformation of the cement can occur if it is more soft than the outer rock (Bois et al., 2011). On the contrary, in the instance that the formation surrounding the cement sheath is less stiff than the cement itself, the probability of radial cracking inside of the cement sheath is increased (Brearden and Lane, 1961).

Proper wellbore construction must take place to increase the odds of a well-constructed cement sheath. For example, high inclination, wellbore eccentricity, and poor centralization can cause air pockets that are difficult to fill during cementing operations. The drilling mud introduced in wellbore construction operations can have a significant effect on bond integrity (Bellabarba et al., 2008). Residual contamination along the wellbore caused by drilling mud and fluids can pollute the cement slurry, occurring for instance when inadequate chemical agents are used for mud removal (Bois et al., 2011).

Gas channels can also develop in unset cement columns resulting in annular gas flow in the wellbore system. Bonett and Pafitis (1996) state that gas migration can occur in the cement by bubble flow, slug flow, interfacial flow, or a rising plume. Bonett and Pafitis (1996) also notes that gas can enter the cement in various manners depending on the evolving state of the setting cement and that residual gases can further propagate an initially existent fracture.

After the cement has set in place, flaws can be created from variations in the casing pressures and temperatures, changes in stress of the rock, and compaction

14

and expansion of the wellbore. Fluctuations in wellbore temperature and pressure conditions can perturb the cement sheath to pull way from the steel casing if the bond strength is exceeded (Shakirah, 2008). Compressive failure of the cement sheath occurs when compressive stresses acting on the cement sheath exceed the cement sheath's compressive strength. Tensile failure can result in radial cracking of the cement sheath occurring under large internal casing pressures and under under high confinement pressure, such as creep of salt formations, the cement sheath can be crushed under shear failure (Teodoriu et al., 2013).

One of the most common forms of debonding between the cement sheath and outer rock formation occurs from cement bulk shrinkage, where a lack of available excess water causes autogenous shrinkage of cement during curing. Here, a microannulus can be formed on the order of 100-300 microns (Shakirah, 2008). Additionally, de-bonding between the cement sheath and steel casing can occur when the steel casing is under internal pressure (Teodoriu et al., 2013).

2.3.3 Importance of Flaws

Flow Through Open Fractures

Zonal isolation is obtained when the cement is intact, fills the annular space, and bonds to the casing and formation. Flaws through the cement or interfaces with the casing and/or formation can result in large, rapid flows through a wellbore. Intact hardened class G oil well cement paste exhibits a permeability on the order of $10E\text{-}17m^2$ ($10E\text{-}3$ mD) (Ghabezloo et al., 2009). This value is on the same order of magnitude with an initial cement permeability of $10E\text{-}17m^2$ used by Carey et al. (2013). Bear (2013) indicates highly fractured rock and microannuli exhibit permeability on the order of $10E\text{-}6m^2$ to $10E\text{-}9m^2$, similar to that of well sorted sand and

gravel (note: 1 Darcy = 10E-12 m^2).

Sarkar et al. (2004) presents various alternatives for modeling fluid flow in fractures and the subsequent simplifications which can be made under given conditions. The most common description of fracture aperture is known as the "cubic law", shown in equation 2.1 in terms of transmissivity:

$$T \equiv kA = \frac{wh^3}{12} \tag{2.1}$$

where the cube of the aperture (h^3) is proportional to transmissivity (T), fracture permeability (k) equals $\frac{h^2}{12}$, and A is wh, or the void's cross sectional area. This relationship defines a mediums ability to transmit flow, where fracture walls are assumed to be parallel plates with smooth surfaces and is generally only applicable for Darcy level flow (Sarkar et al., 2004). This relationship can equivalently be written in terms of aperture (h) as shown in equation 2.2,

$$h = \sqrt[3]{\frac{12Q\mu l}{(P_i - P_o)w}} \tag{2.2}$$

where the fracture length (l), uni-axial volumetric flow rate through the system (Q), dynamic viscosity (μ), and the pressure difference ($\Delta P = P_i - P_o$) across the fracture are proportional to the aperture cubed.

Lomize (1951) studied flow through smooth and rough open fractures, where he generalizes the cubic law for laminar flow in terms of Reynolds number (Re) as $\psi = \frac{96}{Re}$ (Lomize, 1951; Witherspoon et al., 1980), where ψ is the friction factor. The

surface roughness (ϵ) describes the absolute height of an asperity in equation 2.3.

$$\psi = \frac{96}{Re}[1 + 6.0(\frac{\epsilon}{2b})^{1.5}] \tag{2.3}$$

where 2b is the fracture aperture and is valid for $\frac{\epsilon}{2b} > 0.065$. If the right hand side of equation 2.3 is rewritten where roughness is grouped in the term "f" such that $\psi = \frac{96}{Re}f$, the cubic law is expressed in equation 2.4.

$$\frac{Q}{\Delta h} = \frac{C}{f}(2b)^3 \tag{2.4}$$

where C is a constant incorporated in Darcy's law and varies between radial and straight flow as described in Witherspoon et al., 1980.

As natural fractures are not smooth walled, Klimczak et al. (2010) looked to expand current solution methods by idealizing the opening-mode of the fracture as having an elliptical or "Penny-shape" shown in figure 2.4. Klimczak goes on to propose the "Quintic law" in equation 2.5, suggesting a higher degree of nonlinearity is present between flow and aperture than what previously represented in the cubic law.

$$Q = -\frac{4\rho g}{3\mu(\pi\alpha)^2}b^5 \bigtriangledown h \tag{2.5}$$

where α is a proportionality coefficient dependent material coefficients such as fracture toughness, Young's modulus, and Poisson's ratio, μ is the fluid viscosity, ρ is the fluid density, g is gravitational acceleration, and $\bigtriangledown h$ is the hydraulic gradient.

17
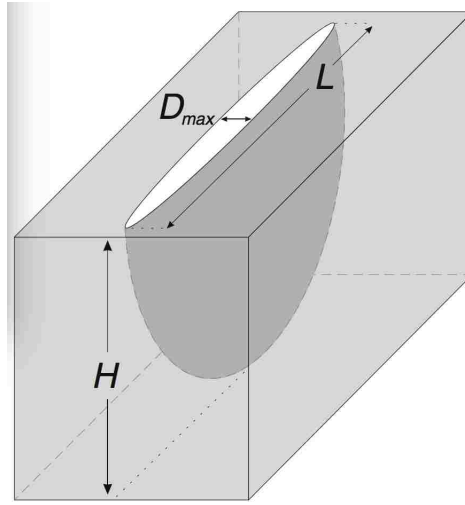
Figure 2.4: Elliptical or "Penny-shaped" opening mode of fracture (Klimczak et al., 2010).

Fracture dependencies

If the wellbore flaw is fracture-like, then it may be appropriate to describe its permeability (which is controlled by its aperture) as a function of stress using models developed for other geomaterials. The size of an aperture depends upon the stresses that are acting to close or open it and these stresses are affected by the contact of asperities on the fracture surface; the general behavior of a fracture under normal stress exhibits a non-linear response.

Bandis et al. (1983) describe a hyperbolic relationship relating aperture to the state of stress. The normal stress is first defined in equation 2.6.

$$\sigma_n = \frac{u_n K_{ni} V_m}{V_m - u_n} \tag{2.6}$$

where σ_n is the normal stress, u_n is the normal joint displacement, V_m is the maximum joint closure and the joint normal stiffness is represented as K_{ni}. The

equation can equivalently be expressed in terms of u_n by:

$$u_n = \frac{V_m \sigma_n}{V_m K_{ni} + \sigma_n} \tag{2.7}$$

The tangent of the normal stress (σ_n) vs. the normal joint displacement (u_n) yields a hyperbolic relationship for the joint tangent normal stiffness shown in equation 2.8.

$$K_n = K_{ni}(1 - \frac{\sigma_n}{K_{ni}V_m})^2 \tag{2.8}$$

The hyperbolic models shown in equation 2.8 has shown to provide an accurate description of rock and fractured joint deformation (Souley et al., 1995; Martinez et al., 2013) and is used to predict aperture size of the microannulus which can be used to estimate permeability of the microannulus. The relationship between fracture closure and the joint normal stress allows for forthright numerical model implementation. Other aperture-stress relationships exist that show agreement with an assortment of porous and fractured rock, such as a volumetric stress-strain approach based on Hooke's law to define the fracture aperture dependence on normal stress (Liu et al., 2009).

2.4 Closed Form Solutions for Wellbore Systems

2.4.1 Bi and Tri Material Hollow Cylinder Solutions

The wellbore system can be approximated by bi-material hollow cylinders (cement sheath-casing; or formation-cement sheath) or tri-material hollow cylinders (formation-cement sheath-casing). Closed form solutions exist for both bi-material and tri-material hollow cylinders (Ugwu, 2008). Figure 2.5 shows the geometrical assumptions needed to define a bi-material set-up.
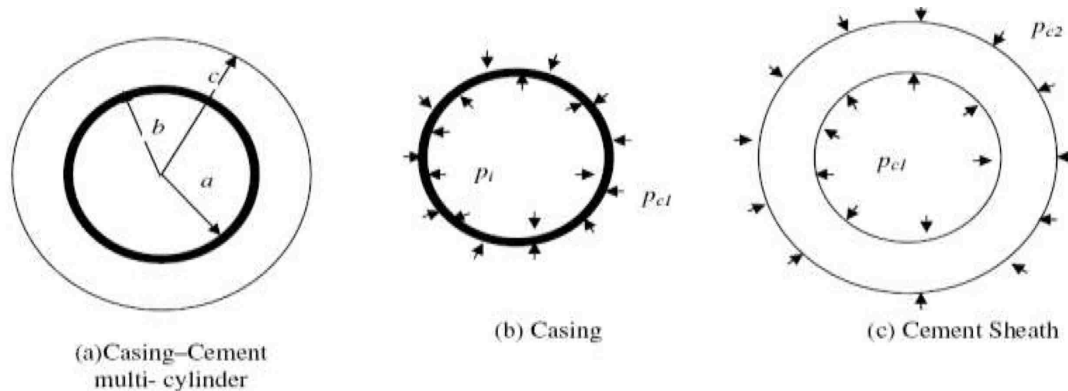
Figure 2.5: Radial dimensions and pressure distribution assumptions on the laboratory wellbore cylinder(s) (Ugwu, 2008).

where a is the internal casing radius, b is the internal cement sheath radius, c is the external cement sheath radius, Pi is the internal casing pressure, PC1 is the interfacial pressure between the casing and cement sheath, and PC2 is the external pressure on the cement sheath.

The radial, hoop, and axial strain given in equations 2.9, 2.10, and 2.11 represent a single isotropic and linear elastic material of cylindrical shape. Under plane strain condition the axial strain is deduced to equation 2.12 and the axial stress can be

written as equation 2.13.

$$\epsilon_{rr} = \frac{1}{E}[\sigma_{rr} - \nu(\sigma_{\theta\theta} + \sigma_{zz})] + \alpha\Delta T \tag{2.9}$$

$$\epsilon_{\theta\theta} = \frac{1}{E}[\sigma_{\theta\theta} - \nu(\sigma_{zz} + \sigma_{rr})] + \alpha\Delta T \tag{2.10}$$

$$\epsilon_{zz} = \frac{1}{E}[\sigma_{zz} - \nu(\sigma_{\theta\theta} + \sigma_{rr})] + \alpha\Delta T = constant \tag{2.11}$$

$$\epsilon_{zz} \approx 0 \tag{2.12}$$

$$\sigma_z = \nu_c[\sigma_r + \sigma_\theta] - \alpha E \delta T \tag{2.13}$$

Using the plane strain condition of equation 2.13 in equation 2.10 yields the hoop strain of equation 2.14 and radial expansion in equation 2.15.

$$\epsilon_{\theta\theta} = \frac{1}{E}[\sigma_\theta(1 - \nu^2) - (\nu - \nu^2)\sigma_r + (1 + \nu)\alpha E \Delta T] \tag{2.14}$$

$$\delta_r = \frac{r}{E}[\sigma_\theta(1 - \nu^2) - (\nu + \nu^2)\sigma_r + (1 + \nu)\alpha E \Delta T] \tag{2.15}$$

It is important to note the steel casing is considered a thin wall pressure cylinder, satisfying the general rule of thumb in equation 2.16.

$$\frac{2b}{t} \approx \frac{2 \cdot 0.05}{0.00235} \geq 20 \tag{2.16}$$

This allows equations 2.17 and 2.18 to be written at casing-cement interface

$$\sigma_r = -p \tag{2.17}$$

$$\sigma_\theta = \frac{pD_m}{2t_s} \tag{2.18}$$

where r_m is the mean casing radius and t_s is the casing thickness. Substituting equation 2.18 into the radial expansion in 2.15 yields,

$$\delta_{rCasing} = \frac{a(Pi - PC1)}{E_s}[\frac{r_m}{t_s}(1 - (\nu_s)^2) + (\nu + (\nu)^2)] + [(1+\nu_s)a\alpha_s E\Delta T] \tag{2.19}$$

a variation of reference temperature through ΔT in equations 2.9, 2.10, and 2.11 is neglected by assuming $\frac{\partial(\Delta T)}{\partial r} = 0$, yielding,

$$\sigma_r = \frac{PC1b^2 - PC2c^2}{c^2 - b^2} - \frac{b^2c^2}{r^2(c^2 - b^2)}(PC1 - PC2) \tag{2.20}$$

$$\sigma_\theta = \frac{PC1b^2 - PC2c^2}{c^2 - b^2} + \frac{b^2c^2}{r^2(c^2 - b^2)}(PC1 - PC2) \tag{2.21}$$

$$\sigma_z = 2\nu\left[\frac{PC1b^2 - PC2c^2}{c^2 - b^2}\right] \tag{2.22}$$

or represented in terms of radial and hoop stress,

$$\begin{aligned}
\sigma_z &= \nu_c[\sigma_r + \sigma_\theta] - \alpha E\delta T \\
&= \nu_c[\sigma_r + \sigma_\theta] \quad at \ \ T = 0
\end{aligned} \tag{2.23}$$

The radial, axial, and tangential stresses are functions of the internal casing pressure, PC1, and are defined in equations 2.20, 2.21, and 2.22 using thick walled cylinder formulation for the cement sheath (Ugwu, 2008). Where the steel casing interface touches the inner surface of the cement sheath, equations 2.20 and 2.21 are simplified to $\sigma_r = -PC1$.

Constants required to define the internal casing pressure located between the cement sheath and steel casing can be found in equations 2.24, 2.25, and 2.26 and the internal casing pressure is obtained by equation 2.27 as presented by Ugwu (2008). These constants are utilized to describe the three tri-axial principal stresses which are termed in this analysis as radial (normal), axial (longitudinal), and tangential (hoop or circumferential) stresses.

$$A = \frac{b}{E_c} \cdot \left[(1 - v_c{}^2)\frac{b^2 - c^2}{c^2 - b^2} + (v_c + v_c{}^2)\right] + \frac{a}{E_s} \cdot \left[(1 - v_s{}^2) + (v_s + v_s{}^2)\right] \tag{2.24}$$

23

$$B = -\frac{b}{E_c} \cdot [(\frac{2c^2}{c^2 - b^2}(1 - v_c{}^2)] \tag{2.25}$$

$$C = \frac{p_i \cdot a}{E_s} \cdot [\frac{r_m}{t_s}(1 - v_s{}^2 + (1 + v_s - v_s{}^2)] \tag{2.26}$$

$$PC1 = \frac{C - B \cdot PC2}{A} \tag{2.27}$$

A tri-material solution can easily be derived using a similar approach of the bi-material solution; taking radial displacement continuity along the formation-cement sheath interface and considering the formation as a thick walled pressure vessel (Ugwu, 2008).

2.4.2 Other Wellbore solutions

Other analytic solutions describing pressure vessels and wellbores have been developed (Haider et al., 2012; Teodoriu et al., 2013; Boresi et al., 1993). The solutions vary due to differences in the imposed boundary conditions and simplifying assumptions.

Thick-wall pressure vessel solutions as described in Boresi et al. (1993) combined with thin wall theory for the steel casing described in Roylance (2001) are the basis of which linear elastic multi-material wellbore solutions are derived. With simplifying assumptions, equations 2.20, 2.21, and 2.22 used to derive a bi-material solution can be directly related to the uni-material body in equations 2.28, 2.29, and 2.30, where

PC1 is the direct internal pressure experienced in the cement sheath in contrast to the pressure between the steel casing and cement sheath.

$$\sigma_r = \frac{P1a^2 - P2b^2}{b^2 - a^2} - \frac{a^2b^2}{r^2(b^2 - a^2)}(P1 - P2) \tag{2.28}$$

$$\sigma_\theta = \frac{P1a^2 - P2b^2}{b^2 - a^2} + \frac{a^2b^2}{r^2(b^2 - a^2)}(P1 - P2) \tag{2.29}$$

$$\sigma_z = \frac{P1a^2 - P2b^2}{b^2 - a^2} + \frac{P}{\pi(b^2 - a^2)} \tag{2.30}$$

Shown in equation 2.31, Haider et al. (2012) use a similar approach to derive axial stress as in equation 2.30.

$$\sigma_z = \frac{PC1b^2 - PC2b^2}{c^2 - b^2} \tag{2.31}$$

Haider's representation of the wellbore encompasses the external pressure load being applied around the closed endcaps, subsequently affecting the plain strain assumption of an infinitely long cylinder. The radial and tangential stresses remain the same for Haider et al. (2012) and Ugwu (2008), while dissimilarities were determined to exist in the analytic formulation of axial stress by a factor of $V_c(\frac{1}{r^2} + 1)$.

Theoretical solutions for uni-material cylinders such as shown in equation 2.32 were expanded by Shi et al. (2007) by demonstrating analytic solutions for elastic hollow cylinders of "n" layers. Shi identified that radial displacement decreases with

25

increasing layers for both externally and internally applied pressure combinations.

$$u_r = \frac{1-\nu}{E} \frac{(p_i r_i^2 - p_o r_o^2)r}{r_o^2 - r_i^2} + \frac{1+\nu}{E} \frac{(p_i - p_o)r_i^2 r_o^2}{(r_o^2 - r_i^2)r} \tag{2.32}$$

2.5 Numerical Models of the Wellbore System

Characterizing material parameters with constitutive models is a complex field in solid mechanics; the end-goal being to adequately define material properties such that the mechanical response represents the true system. The interest in understanding the in-situ geomechanical response of wellbores has led to a number of efforts to model their behavior.

Using homogeneous, isotropic, and linearly elastic material properties for the cement sheath, rock formation, and steel casing, the wellbore system was modeled by Thiercelin et al. (1997). This finite element model included a Mohr-Couloumb criterion for cement, debonding, and traction for failure criterion (Bois et al., 2011).

Cement sheath behavior has been modeled using Finite Element Analysis (FEA) which includes the elastic-plastic cement behavior, formation imposed far field stresses, cement shrinkage and expansion, hardening, interfacial debonding, and Von Mises type failure criterion (Gray et al., 2009; Ravi et al., 2002). The time history of the reservoir system including the setting of the cement sheath slurry, hardening, and shrinkage are wellbore life characteristics modeled to understand the cumulative effects on prospective damage and fracture (Gray et al., 2009). More complex constitutive laws have have been used to simulate the viscoplasticity rate dependence and non-linear hardening effects of geological rocks, cement, and other brittle materials (Martinez et al., 2013; Brannon et al., 2009).

Cement sheaths in offshore wellbore systems require a modeling approach to represent the atypical loading conditions. Tables of data have been developed to characterize long and short term cement properties, wellbore geometry, pressure and temperature of the casing, and moments at which the cement sheath can be subject to damage (Ravi et al., 2003). Probabilistic tools have been developed to assess the severity of failure that result from thermal stresses caused by surface fluid injection (sea H_2O, CO_2, steam) into hydrocarbon reservoirs (Ferla et al., 2009). Numerical modelers are now endeavoring to represent cement slurry hardening, shrinkage, pore pressure effects on dynamic CO_2 injection process as well as subsequent rock fracture (Martinez et al., 2013; Carey et al., 2013; Gray et al., 2009).

Kayenta Parameters

Finite Element codes require numerous specifications to uniquely define a model including options of various solvers, element formulations, contact definitions, boundary condition enforcement options and more. A critical addition to these finite element techniques is the constitutive material model imposed, which can have a significant effect when characterizing mechanical response to an imposed stress condition.

Kayenta is a constitutive model that can be used to model complex features of a material including nonlinear elasticity, porosity, rate-dependence and more. However, the Kayenta material model can be reduced to linear elasticity when only a constant bulk modulus (K) and constant shear modulus (G) are defined; G and K can be determined from Young's modulus and Poisson's ratio (equations 2.33 and 2.34). With the additional specification of yield strength, Von Mises plasticity can also be characterized. A brief description on stress characterization fundamentals is

provided in Appendix B.

$$K = \frac{E}{3(1 - 2\nu)} \tag{2.33}$$

$$G = \frac{E}{2(1 + \nu)} \tag{2.34}$$

Appendix C displays linear elasticity implementation when B1 and B2 of equation 2.35 and G1 and G2 of equation 2.36 parameters are set to zero. Hydrostatic data are used to obtain the nonlinear bulk modulus parameters and triaxial compression data are used to obtain the shear modulus parameters.

$$K = b_o + b_1 e^{-\frac{b_2}{|I_1|}} \tag{2.35}$$

$$G = g_o\left[\frac{1 - g_1 e^{(-g_2 J_2^{0.5})}}{1 - g_1}\right] \tag{2.36}$$

Various features available within the Kayenta material model used for material parametrization including the cement sheath and flawed interfacial fracture elements are described in chapters 3 and 4. The Kayenta constitutive model discussed herein was principally developed by Rebecca Brannon (Brannon et al., 2009) and the model capabilities discussed herein reflect the user-guide documentation. Yield surfaces that can be achieved within a given stress state are:

1. Yield surface = boundary of elastically attainable stress states

2. Limit surface = boundary of attainable stress states

3. They coincide if there is no strain hardening

Chapter 3

Development of Laboratory Wellbore Model

3.1 Introduction

A numerical model was created of the laboratory configuration used to test wellbore samples (cement sheaths cast on steel pipe). The purpose of the model is to estimate the stresses and strains that the casing-cement system experiences under different loading conditions and with different material properties. The model includes a 100 μm wide microannulus region adjacent to the casing which can be open or can have properties of a specified material (i.e., cement or repair material). A model verification and convergence study was conducted by comparing the results from the model with analytical solutions. The analytical solutions are for a linearly elastic material in a uni-, bi- and tri-hollow cylinder configuration.

Different model versions are implemented based on how the microannulus region and the casing-cement interface are considered. The simplest version uses a per-

fectly bonded casing-cement interface. This model version is the one that can be compared to analytical solutions. Another model version is realized if the microannulus adjacent to the casing-cement interface is modeled as open, either around the entire circumference or over a portion of it. The imposed voids are intended to be representative of the flaws which could be experienced after a microannulus develops between the cement sheath and steel casing. If these flaws do not initially compromise wellbore integrity, perturbation of the wellbore system may eventually cause loss of integrity. This model can be useful in describing the bounding case of a microannulus that is literally an open space between the cement and casing. Assuming a frictional casing-cement interface yields another model version. The frictional model was used in a parametric study of the wellbore system response under different loading conditions and with different material properties. Both cement and repair materials were modeled in the microannulus region.

3.2   Lab Scale Wellbore System

Physical tests conducted in the lab simulate conditions of intact specimens of a wellbore system (perfect bond between the cement and casing), flawed specimens, and those containing an injected nanocomposite epoxy repair material. The types of microannulus flaws between the casing-cement interface in the specimens are intended to represent flaws that are developed by wellbore loading conditions described in section 2.3.2. The specimens are tested in a pressure vessel capable of applying both confining and internal casing stresses on the specimen that can open and close the flaws (Stormont et al., 2015). The lab-scale seal system testing configuration is shown in figure 3.1. The pressure vessel apparatus is capable of applying internal casing pressures up to 20 MPa and confining pressure up to 35 MPa.
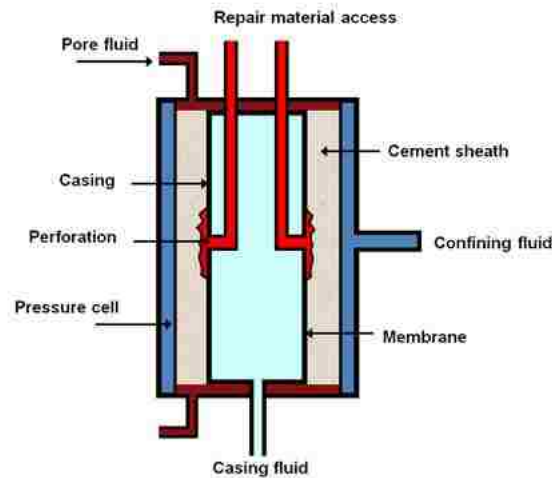
Figure 3.1: Schematic of the lab-scale seal system testing apparatus (Stormont, 2014)

Microannulus flaws of varying size ($\approx$ 10 µm to 150 µm wide) were created in the specimens. Beginning with an intact specimen, small microannuli were created by cooling the steel casing with liquid nitrogen or dry ice. Large microannuli are created by removing the steel casing from the cement sheath after 24 hours of curing time. This is accomplished by applying a release film around the steel casing prior to setting the cement sheath. Discrete voids (600 µm wide) were created by inserting a steel shim wrapped in release film into a section of the cement - steel casing contact; the laboratory wellbore mold and steel shim are shown in figure 3.2. The release film is removed after 24 hours of curing and the sample continues to cure for six addition days (one week total curing time).

The cement material used to create samples was Type G (API Class G) oil well cement (OWC). As a basic well cement, it is known for its high degree of fineness and flowability and is comparable to ASTM Class II and V cements (water/cement ratio of 0.3). The cement is obtained by grinding clinker, consisting of hydraulic calcium silicates with calcium sulfate additive. The laboratory specimens were cured in a humid environment for a minimum of 14 days under 55 °C (Stormont et al., 2015).

Figure 3.2: Laboratory wellbore mold of for lab-scale seal system

The testing consisted of measuring gas flow along the axis of specimens under different external (confining) and internal (casing) pressures. Some samples with flaws were subsequently re-tested after being repaired. Repair material polymers of interest include novolac epoxy, low modulus polysulfide-siloxance epoxy, microfine cement, and Styrene-butadiene rubber (SBR) polymer latex. The nanomaterials of interest to be loaded into these repair materials include multiwall carbon nanotubes (MWCNTs), nanoclay, nanosilica, and nanoalumina particles. Characteristics desired for the nanocomposite sealant repair material include high bond strength to casing and cement interfaces, low permeability, and high fracture toughness. From all candidate nanocomposites, those with the most promising material properties are chosen for testing in wellbore system specimens (Stormont et al., 2015).

The epoxy material properties utilized in this finite element model are those of novolac epoxy with MWCNT at 0.5 % nano content (by weight). The MWCNTs

33

are added to the epoxy resin and mixed by mechanical (magnetic) and sonification techniques as shown in figure 3.3. These processes occured under temperatures ranging from 65-110°C and for up to two hours on a given batch. Figure 3.4 shows the repair material being injected into a flawed laboratory wellbore sample.

(a) Mechanical stirring   (b) Sonification
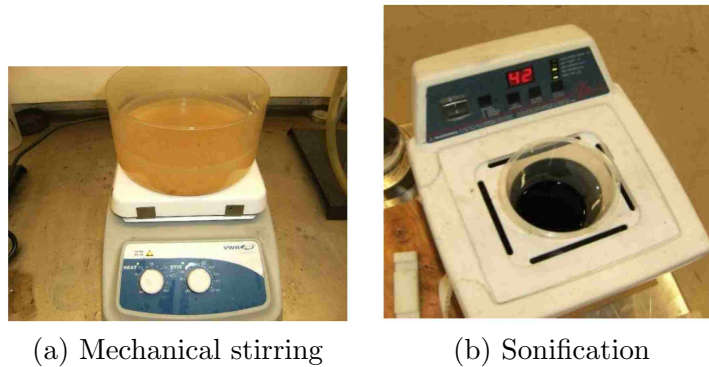
Figure 3.3: Various mixing methods for the polymer nanocomposite are shown (Stormont, 2014)

Figure 3.4: A flawed specimen is shown undergoing injection with an epoxy repair material (Stormont, 2014)

Flow through the flaws was interpreted as a hydraulic aperture size based on the so-called cubic law. The hydraulic aperture tended to close as stresses acting across the casing-cement interface increased.

While some flaws are relatively large - hydraulic apertures in excess of 100 μm

- they do not appear to be completely open. The rate of closure of the hydraulic aperture with stress increase is less than what is expected for the closure of the cement sheath alone from analytic (elastic) solutions. Stormont et al. (2015) concluded that the microannulus behavior is not consistent with a fully open microannulus. Figure 3.5 demonstrates this phenomenon by comparing the analytic elastic response of the thick-walled cement sheath without a casing presented in equation 2.32 to laboratory measurements of hydraulic aperture. Section 4.2 describes how hydraulic aperture is acquired from laboratory data.
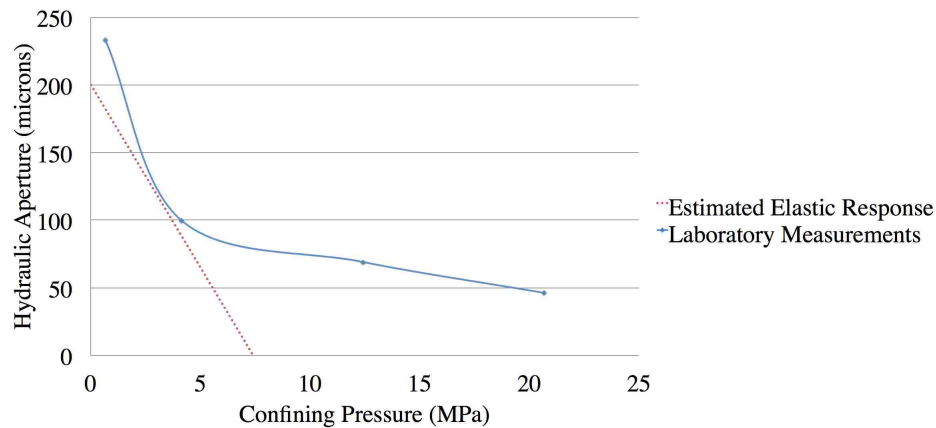
Figure 3.5: Laboratory and analytic hydraulic aperture response to increasing confinement

The FEM model discussed herein is used to describe loading conditions for the lab-scale system for which an analytical solution is not defined, substantiate results obtained from bench-top experiments, and obtain material relationships that can be scaled up to a reservoir system.

3.3   Laboratory Wellbore Finite Element Model

3.3.1   Software Used

For the computational tasks of this project, Sandia National Laboratories' Sierra simulation software was used. Sierra/SolidMechanics is a general purpose massively parallel nonlinear solid mechanics finite element code for explicit transient dynamics, implicit transient dynamics and quasi-static analysis of structures. It is based on an extensive suite of element, material, contact and solver libraries for analyzing the nonlinear mechanical response of solids subjected to loadings. Sierra/Solid Mechanics VOTD User's Guide (SIERRA Solid Mechanics Team, 2011) describes these capabilities in detail.

Mean quadrature, linear midpoint-increment integrated hex-8 elements were used for the model mesh generation. This element was chosen due to its ubiquitous use and reputability in 3-Dimensional FEA analysis in addition to an ability to capture the simple/uniform laboratory wellbore curvature upon refinement of the brick geometry. Modeling the joint interface between materials, such as for the cement-casing interfacial contact, required development of similar meshes for both frictional and non-frictional simulations. To accomplish this, surfaces remained un-merged during mesh generation and contact was specified as an input model parameter.

During simulations where a perfect bond was desired between two interfaces, such as convergence study to a closed-form solution, tied joints were implemented between conjugate node pairs. Subsequent simulations for the laboratory wellbore model convergence study implemented tied contact or an appropriate friction model. Finite Element Taring and Interconnecting Linear equation Solver (FETI) was used as an implicit equation solver for these simulations.

Material models used for this analysis include elastic, elastic-plastic, and the "Kayenta" constitutive model. Kayenta has the ability to model porosity, material softening, nonlinear elasticity and more as described in section 2.5 (Brannon et al., 2009). The material parameters for all constitutive models implemented in this study are shown in Appendix C.

3.3.2 Loading and Boundary Conditions

An isometric view of the wellbore specimen mesh can be seen in figure 3.6 with the hex element type class implemented upon mesh generation.
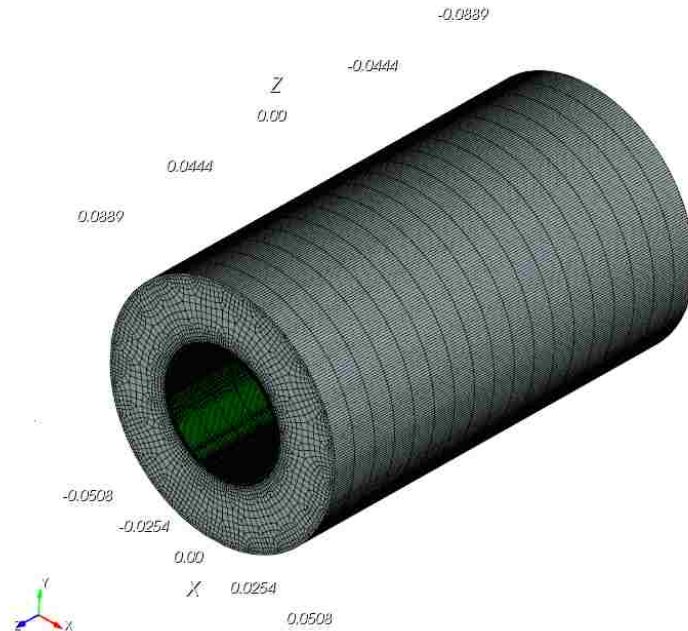
Figure 3.6: Isometric view of the laboratory wellbore model (unit: meters)

The baseline loading scenario involved linearly increasing the internal casing pressure up to maximum load of 20 MPa, while the external casing pressure was increased to 30 MPa over the simulation. Material specification alternatives for the laboratory

wellbore and the baseline loading condition are shown in figure 3.7. All nodes on the top and bottom laboratory wellbore surfaces, including cement, steel, and epoxy, are defined as fixed in the axial z-direction to obtain a plane-strain condition.
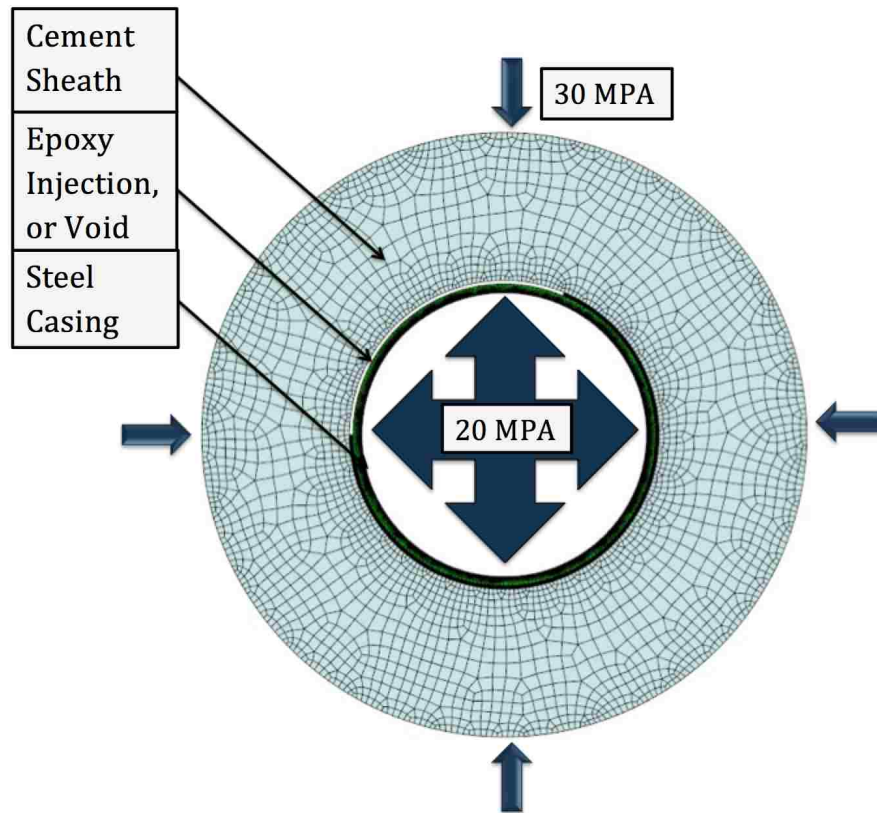
Figure 3.7: Viable loading configuration and material designation of the laboratory wellbore

An example of the linear rate at which specimens are loaded is shown in figure 3.8 for a 30 MPa confining and 20 MPa internal stress over 0.5 seconds. Therefore, the boundary conditions initiate at a stress free condition and linearly increase to the desired load. Intermediate pressure conditions can easily be interpolated under these constraints. The laboratory wellbore pressure vessel apparatus can apply a range of internal and external pressure conditions, further described in section 4.2. The loading rate applied to the FEA implementation of the laboratory wellbore is

not intended to simulate the loading rate in the laboratory.
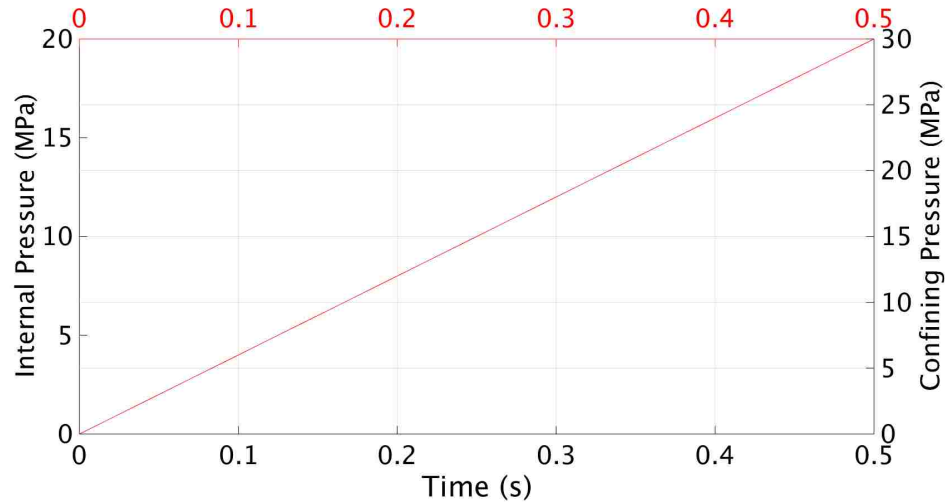
Figure 3.8: Arbitrary pressure condition to denote the linear loading scheme implemented for pressure boundary conditions

The first flawed model was developed to represent a specimen with a slotted flaw. This model contains a set of elements between the steel casing and cement sheath, spanning along the length of the laboratory wellbore, that have varying material properties. This span of elements is approximately 113° along the casing-cement interface, equivalent to a 5 cm wide by 600 µm thick slot. The elements of this microannulus can be assigned to represent epoxy or cement. Alternatively, the elements can be removed to resemble a flawed microannulus that is open, as shown in figure 3.9.

The slotted flaw configuration was seldom used in preliminary laboratory testing; only a limited number of specimens implemented this design. Rather, the focus of the experimental program shifted to specimens that were created and tested with a microannulus (flaw) along the entire circumference of the cement-casing interface. This configuration allows for axisymmetric geometry. The axisymmetric mesh in-

39

(a) Lab specimen with slotted flaw   (b) Mesh with slotted flaw
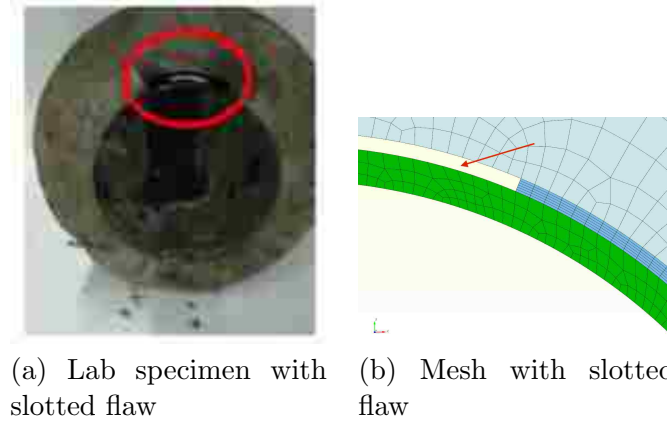
Figure 3.9: Flaw highlight shown on the lab specimen and finite element mesh

cludes a uniform microannulus space between the steel casing and cement sheath. The two laboratory wellbore geometrical dimensions implemented in this study are illustrated by figure 3.10 and table 3.1.
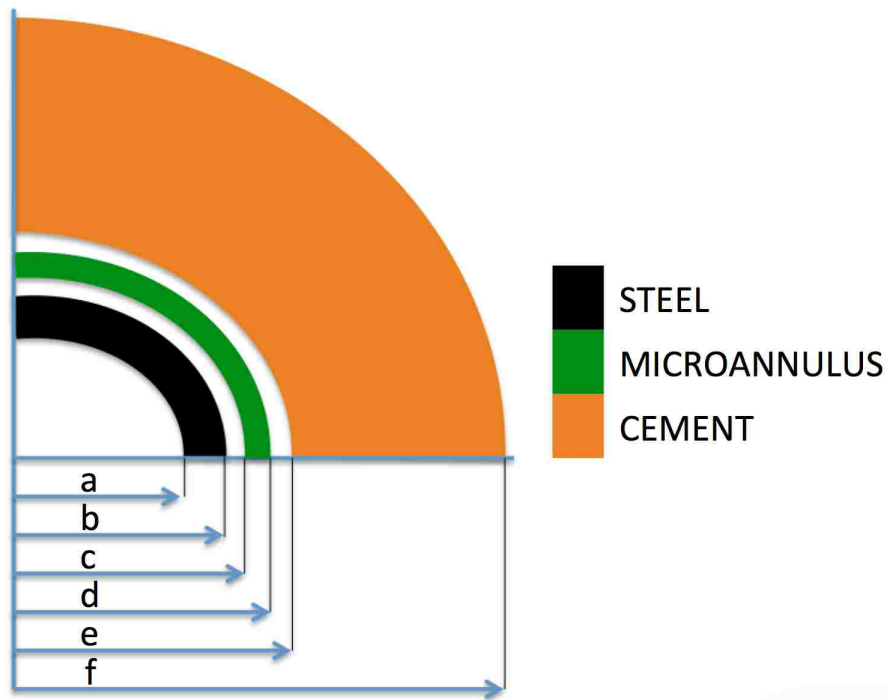
Figure 3.10: An exploded view of the laboratory wellbore model used for parametric study. Dimensions for models utilizing this configuration are shown in table 3.1

Table 3.1: Laboratory wellbore radial dimensions shown for a 2.35 mm and 3.25 mm steel casing

Point of Interest	Tag	Unit	Casing Thickness: 2.35 mm	Casing Thickness: 3.25 mm
Internal Steel Casing	a	m	0.026475	0.026975
External Steel Casing, Internal Microannulus	b,c	m	0.028825	0.030225
External Microannulus, Internal Cement Sheath	d,e	m	0.028925	0.030325
Outer Cement Sheath	f	m	0.0508	0.0508

Figure 3.11 displays the microannulus space as pink interfacial fracture elements around the circumference the wellbore between the cement sheath and steel casing.

These elements can be assigned properties of epoxy, cement, or removed as a flaw that is open.

(a)   (b)   (c)
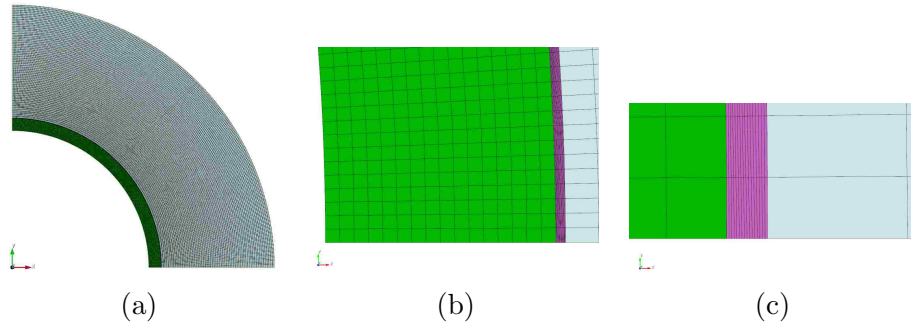
Figure 3.11: Various views of the axisymmetric mesh

A description of how these elements are referred to throughout this study is shown in figure 3.12. The full scale and axisymmetric laboratory wellbore models use this naming convention.
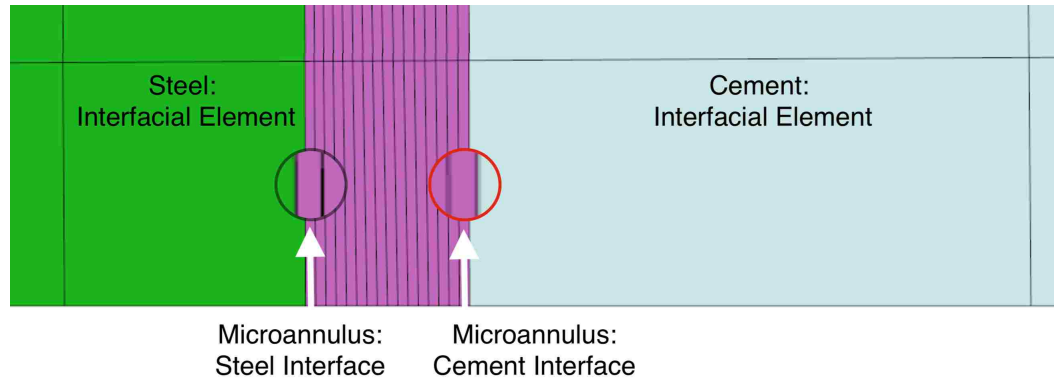
Figure 3.12: Interfacial element detail of the laboratory wellbore ("Cement: Outer Cement Sheath" is located as the outer most element along the cement sheath radius).

Material properties were obtained from laboratory testing efforts at The University of New Mexico (Stormont, 2014). The properties used for the modeling of the elastic and elastic-plastic laboratory wellbore systems are given in table 3.2.

Table 3.2: Laboratory wellbore properties used in numerical simulations

Parameter	Symbol	Unit	Value
Young's Modulus: Cement	E_c	Pa	4.00×10^9
Young's Modulus: Steel	E_s	Pa	2.00×10^{11}
Young's Modulus: Epoxy	E_e	Pa	19.0×10^9
Poisson's Ratio: Cement	v_c	Dimensionless	0.19
Poisson's Ratio: Steel	v_s	Dimensionless	0.30
Poisson's Ratio: Epoxy	v_e	Dimensionless	0.22
Yield Stress: Cement	Ey_c	Pa	4.28×10^6
Yield Stress: Epoxy	Ey_e	Pa	8.00×10^7

3.3.3 Verification: Convergence Study

The appropriate mesh size was determined by mesh refinement studies on five meshes ranging from a course mesh of 114 elements to a fine mesh consisting of 4,670,000 elements. Convergence was established with a mesh consisting of 466,000 elements, and this model was used for subsequent analysis of the laboratory wellbore conditions. A perfectly bonded casing-cement interface was enforced through tied contact in convergence testing. Assumptions in this derivation include a tri-axial stress state with no initial state of stress present in the cement. The cement sheath is treated as a thick walled pressure vessel and the steel casing as a thin walled pressure vessel (Ugwu, 2008). The elastic material properties for convergence studies are shown in table 3.2. As shown in figure 3.13, the radial stress at the outer cement sheath shows convergence within less than 1% error against the analytic bi-material solution.

Further mesh discretization beyond this element size does not improve the solution accuracy.
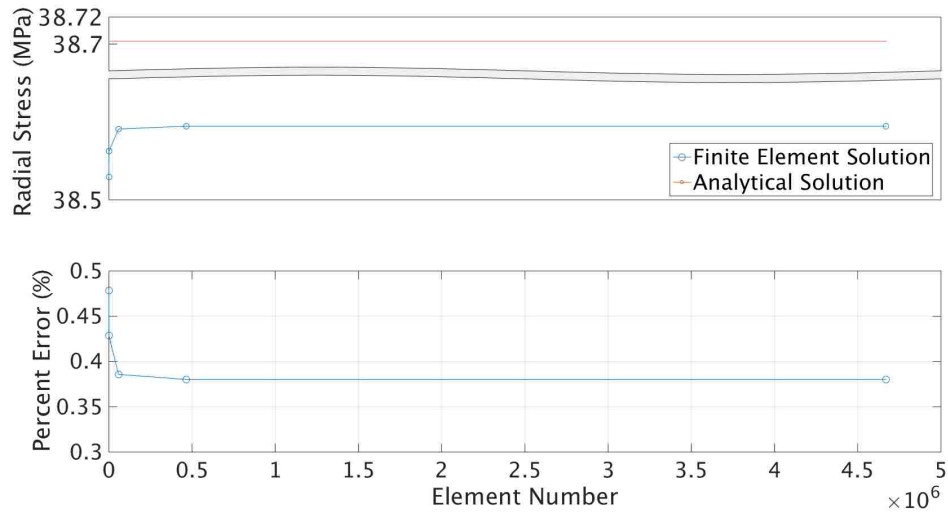
Figure 3.13: Radial stress plotted over the number of elements during mesh refinement for the bi-material laboratory wellbore subjected to an internal pressure of 20 MPa and an external pressure of 30MPa. Convergence within 1% error is obtained upon mesh refinement.

To evaluate convergence along the radial distance of the laboratory wellbore, elements were chosen from the inner surface of the cement sheath and outer radius of the cement sheath wall, denoted as radius "e" and "f" respectively in figure 3.10. To succinctly define the state of stress experienced in the numerical model, the radial, hoop, and axial stresses of equations 2.20, 2.21, 2.22 were taken to derive the Von Mises equivalent stress. Figure 3.14 shows the results of the convergence study along with the analytical solution as function of distance in the cement sheath.

It can be seen in figure 3.14 that analytical convergence was obtained within less than 1% error for the Von Mises stress. To obtain convergence to a closed form solution, these convergence studies are presented using linear-elastic material models for the cement sheath and steel casing. Parametric studies are subsequently

44
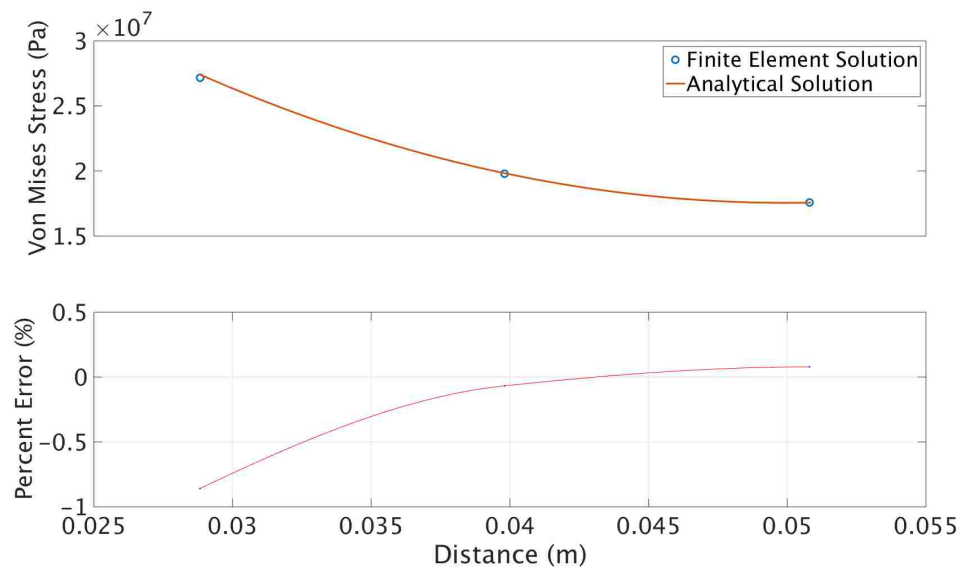
Figure 3.14: Von Mises stress along the inner edge to outer edge of the cement sheath of a bi-material laboratory wellbore subjected to an internal pressure of 20 MPa and an external pressure of 30MPa. Convergence within 1% error is shown along this radius.

conducted using an identical converged mesh, but with both linear and non-linear material models.

To ensure that the pressure distributions are being loaded in the appropriate direction and magnitude, surface normal vectors are plotted on the laboratory wellbore configuration in figure 3.15.
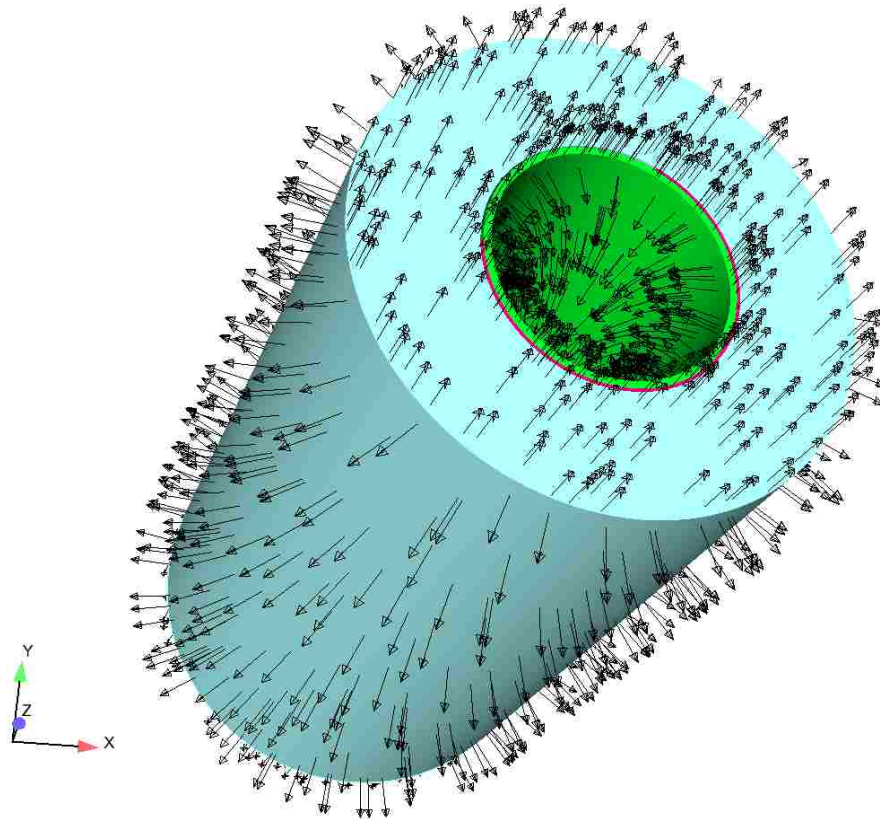
Figure 3.15: Surface normal vectors shown on the full scale laboratory wellbore

3.3.4   Validation: Cement Constitutive Model

The constitutive model assigned to a material has a significant impact on a model's response. The complexity of a constitutive model depends on numerous factors, some of which include the heterogeneous micro-structure of a material, creep behavior, material softening, modal response to varying frequencies, and much more. The brittle nature of cement and other geomechanic materials exhibit complex material properties such as material softening that make describing its behavior analytically difficult. While commercial finite element codes have made progress in modeling the response of such materials to given boundary conditions, significant challenges remain to perform this task accurately and efficiently (both in computation cost and ease of data parametrization).

To model the cement material used throughout this analysis, a constitutive model developed by Brannon et al. (2009), called Kayenta, is used. In the most minimalist sense, Kayenta can model simple linear elastic behavior, but with more detailed parametrization can also model complex behavior such as material softening and rate dependence of viscoplastic materials; hydrostatic and triaxial testing are base testing requirements to parametrize more complex behavior. An overview of cement and concrete response under uni-axial compression in Figure 3.16 shows material softening behavior. This data is from Philippacopoulos and Berndt (2001) and Taha (2015).

Because the testing required to parametrize a material such as cement was beyond the scope of this project, a pre-parametrized Portland cement material model in the Kayenta material repository was used as base parameters to the constitutive model in this analysis. Slight modifications to values such as bulk modulus (K), shear modulus (G) and the meridional profile constants (a1, a2, a3, and a4) which

47
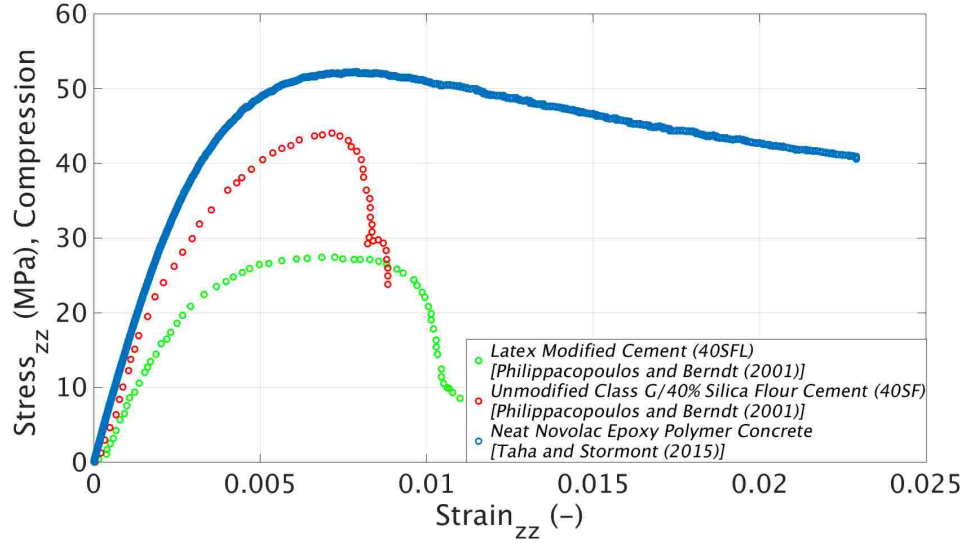
Figure 3.16: Cement uniaxial compression specimen stress-strain response shown for various data in the literature

describe the shear limit surface behavior, were performed to obtain behavior similar to that given by Philippacopoulos and Berndt (2001). The unmodified class G, 40 % Silica Flour Cement denoted as (40SF) by Philippacopoulos and Berndt (2001) was chosen to calibrate the Kayenta constitutive model. Equation 3.1 shows Kayenta's formulation of the shear limit surface behavior in tri-axial compression as a function of I_1.

$$F_f(I_1) = a_1 - a_3 e^{(-a_2 I_1)} + a_4 I_1 \tag{3.1}$$

The mesh used for the uni-axial compression consisted of 20,700 eight-node hexahedra elements (figure 3.17). The cylinder has a radius of 38 mm, height of 76 mm, and was loaded under a displacement control of 3.81E-6 m/sec (final axial displacement of 1.798 mm over 472 seconds). The maximum axial stress and strain of the cylinder block was obtained at each time-step.

48
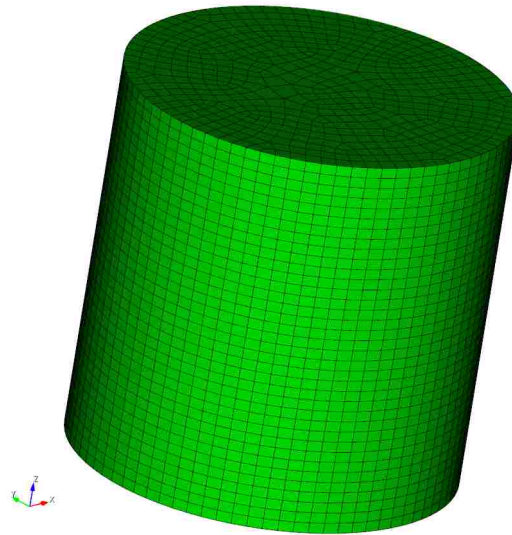
Figure 3.17: Cement uniaxial compression specimen mesh

To obtain a best fit to the cement behavior, Portland cement parameters obtained from the Kayenta materials database were altered from the original to final values (all else held constant) as shown in table 3.3. The cement sheath is assumed uniform and therefore characteristics such as the "wall effect" are not accounted for in this numerical model. Additionally, eight material softening parameters were defined as briefly described in section 4.3.2 and values referenced in Appendix C.

Table 3.3: Altered Portland cement parameters used in the Kayenta constitutive model

Symbol	Initial Value	Final Value	Units
B	2.2E9	6.0E9	Pa
G	1.7E9	4.0E9	Pa
a1	4.26455E8	4.347E8	Pa
a3	4.19116E8	4.20E8	Pa

The comparison of Philippacopoulos' experimental data and the finite element results are shown in figure 3.18. It is recognized that the Kayenta FEA constitutive

model portrays a moderately higher peak axial stress than the laboratory testing of Philippacopoulos and Berndt (2001). Additionally, the Kayenta model post peak behavior softens with a slightly varied response of laboratory testing, but within close range of the absolute strain value. As previously mentioned, to more accurately model behavior of a material, in this case a mix of Portland cement, hydrostatic and triaxial testing should be performed for constitutive model parametrization.
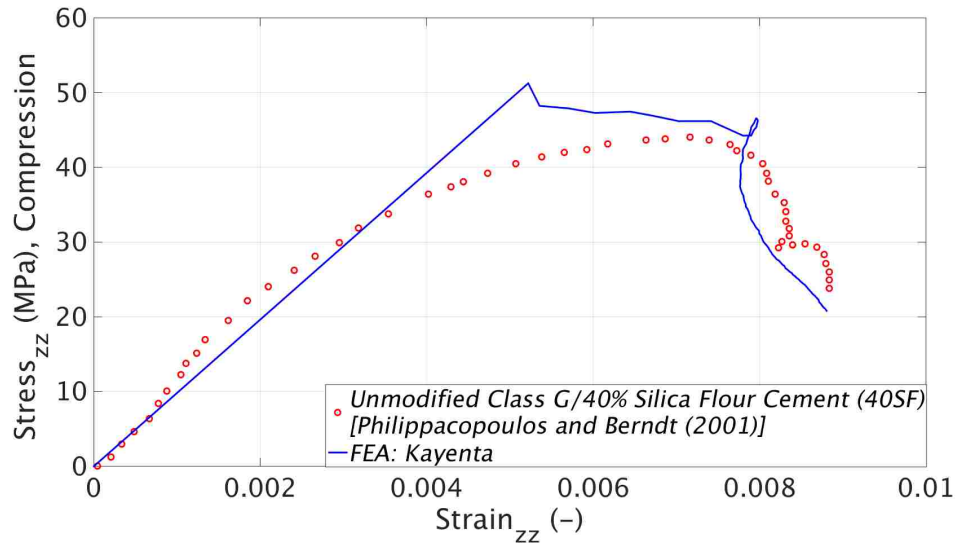
Figure 3.18: FEA constitutive model fit to experimental data for a cement specimen undergoing uni-axial compression

3.3.5 Gap Model

A wellbore specimen with an open microannulus can be represented as two uni-material bodies separated by some space. This uni-material representation is satisfied up to the point at which contact is initiated between the cement sheath and steel casing. Figure 3.19 displays convergence of this process within 1% for the 2.35 μm steel casing and elastic cement sheath. Contact is initiated at 4.85 MPa, the required pressure to close an equivalent gap space of 100 μm analytically.
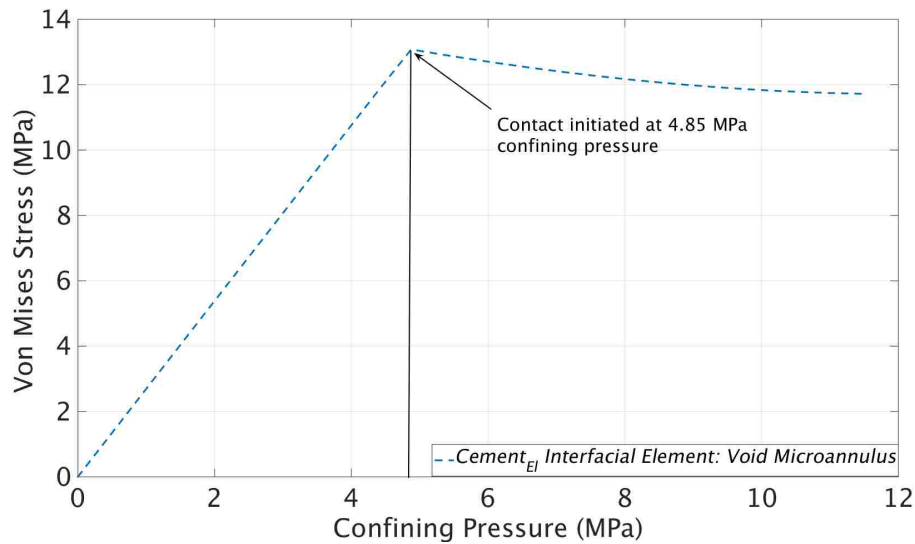
Figure 3.19: Contact initiation of a 2.35 mm steel casing with an initial void
interface using the following framework:
Loading: σ_{conf} = 12 MPa & σ_{int} = 0.0 MPa

3.3.6 Frictional Model

Both frictional and tied (perfectly bonded) contact models were implemented for the axisymmetric laboratory wellbore configuration. Figure 3.20 demonstrates that no variation is recognized in the Von Mises, radial, tangential, and axial stress at the

"microannulus: steel interface" element (as shown in figure 3.12) for friction and tied models. The similarity in tied and frictional contact is due to the axisymmetric loading conditions imposed on the model. That is, the internal and external pressures on the surface of the laboratory wellbore are applied normal, resulting in infinitesimal shear deformation along material interfaces. A cohesive traction model should be considered to describe the bond between steel and cement in future work.
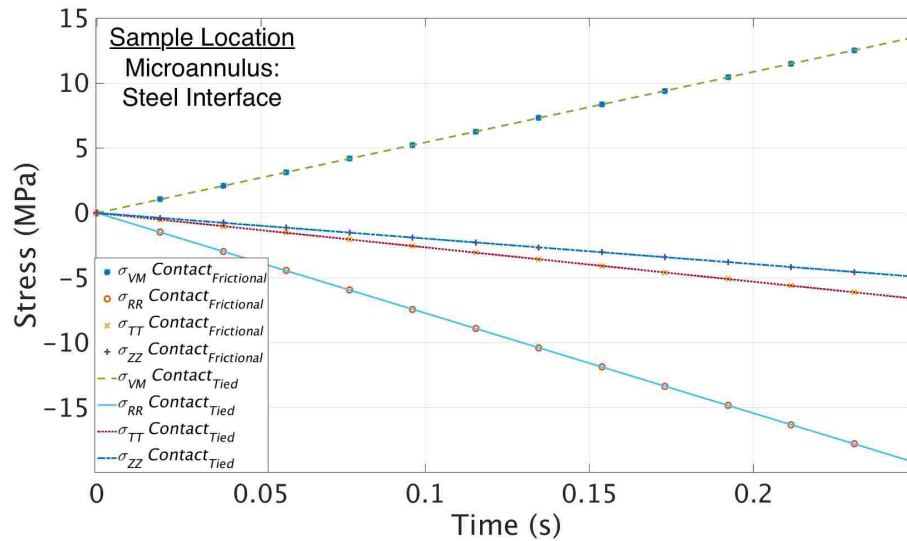
Figure 3.20: Frictional and tied contact models using the following framework:
Unimpaired wellbore & 2.35 mm casing;
Loading: $\sigma_{conf} = 15$ MPa & $\sigma_{int} = 10.0$ MPa

Figure 3.21 shows elastic and Kayenta (plasticity constitutive model discussed in sections 2.5 and 4.3.2) material models definitions on a frictional interface, with all other simulation boundary conditions held constant.

It can be concluded that the varying states of stress in the Kayenta and elastic models arise from contrasting material model definitions, not the contact definition. The subsequent use of a tied contact model for the parametric studies that involve axisymmetric conditions is justified by this result. The benefit of this assumption is
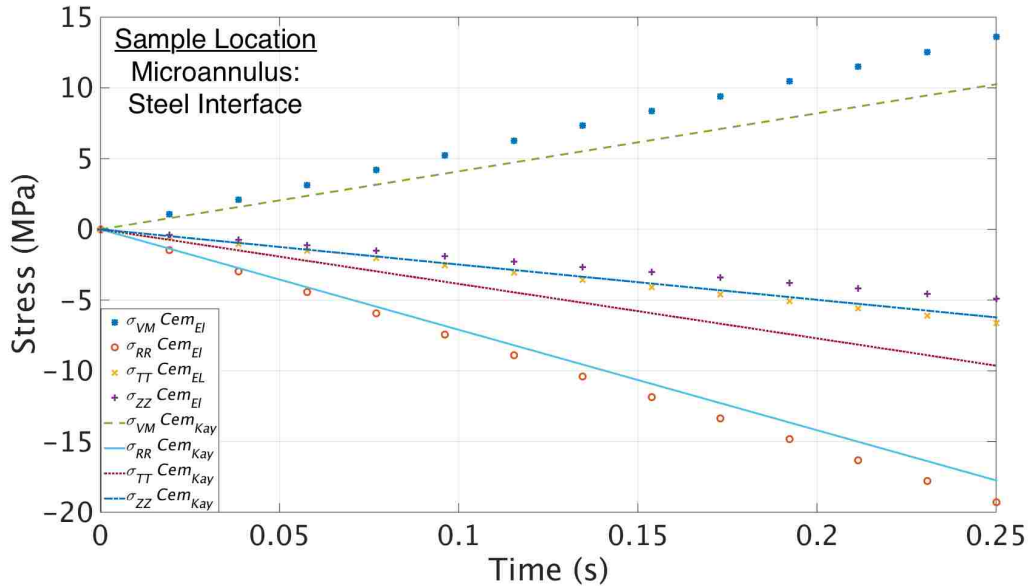
Figure 3.21: Elastic and Kayenta models with frictional contact enforcement using
the following framework:
Unimpaired wellbore & 2.35 mm casing;
Loading: $\sigma_{conf} = 15$ MPa & $\sigma_{int} = 10.0$ MPa

predominately seen in computational efficiency.

3.4   Parametric Study

Full Scale Laboratory Wellbore

Following convergence studies, the cement and epoxy filled microannulus laboratory
wellbores were analyzed for mechanical integrity by examining the Von Mises stress
and equivalent plastic strain (EQPS) over various loading cycles. The mechanical
integrity metric in this study is defined to represent the external formation and
internal casing pressure loading conditions that are present in a wellbore system.
This metric is not representative of thermal (e.g. formation temperature flux) or

chemical (e.g. cement shrinkage) stresses that could be present in a wellbore system. For the following examination, cement was defined as elastic perfectly plastic, where specific material properties can found in the input deck located in table 3.2 and Appendix C.

Stress and strain are provided as a function of distance in the wellbore configuration in figures 3.22 and 3.23. The results are labelled as the elemental material property and location prior to the colon, followed by the material interface this element is in contact with. For example, "Cement$_{ElPl}$ Interfacial Element: Cement$_{ElPl}$ Microannulus" defines an elastic-plastic cement element that is in contact with an elastic-plastic cement microannulus and "Epoxy$_{ElPl}$ Microannulus Element (Cement Interface): Cement$_{ElPl}$ Sheath" defines an elastic-plastic epoxy element that is in contact with an elastic-plastic cement sheath. For simplicity, material failure is interpreted at the time a material no longer has the ability to sustain an increasing Von Mises equivalent stress.

The cement sheath filled microannulus stress and strain analysis for an elastic perfectly plastic constitutive model can be found in figures 3.22 and 3.23. The material parameters used in these simulations are defined in table 3.2. The Von Mises stresses are nearly identical at each location in microannulus region, where a maximum stress of approximately 4.28×10^6 Pa is reached at 0.1 seconds. This is consistent with an ≈ 4.28 MPa cement yield stress. The largest magnitude of plastic strain at 0.5 seconds, a confining pressure of 30 MPa, internal pressure of 20 MPa, and a Von Mises stress of 4.28×10^6 Pa was approximately 7.27×10^{-3} and was seen in cement microannulus at the interface to the steel casing.

Figure 3.22: Cement repaired microannulus showing Von Mises stress vs. time
using the following framework:
Loading: $\sigma_{conf} = 30$ MPa & $\sigma_{int} = 20.0$ MPa
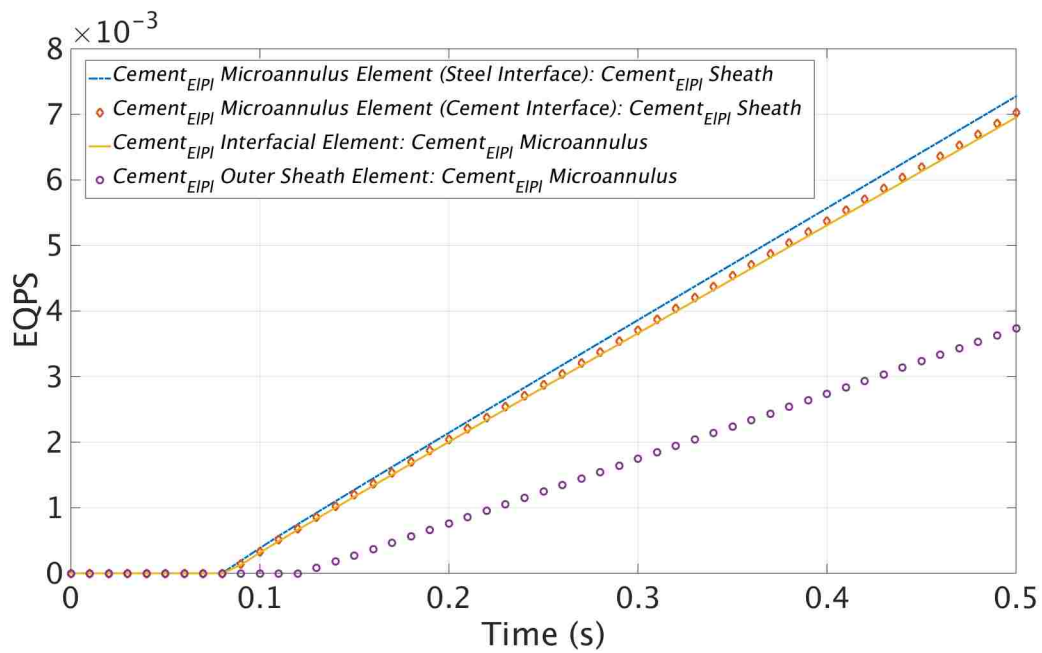
Figure 3.23: Cement repaired microannulus showing equivalent plastic strain vs. time using the following framework:
Loading: $\sigma_{conf} = 30$ MPa & $\sigma_{int} = 20.0$ MPa

Figures 3.24 and 3.25 provide results from the epoxy filled microannulus simulation. The cement sheath interfacial element reaches the same yield stress as in the cement filled microannulus and maintains this 4.28×10^6 Pa state of stress while going into plastic strain of similar magnitude. The epoxy microannulus continually supports higher stress levels throughout the simulation reaching approximately 1.7×10^7 Pa and exhibiting no plastic strain. The largest magnitude of plastic strain was seen in the cement interfacial element at 0.5 seconds, a confining pressure of 30 MPa, internal pressure of 20 MPa, and a Von Mises stress of 4.28×10^6 Pa was approximately 7.2×10^{-3} and was seen in cement interfacial element.
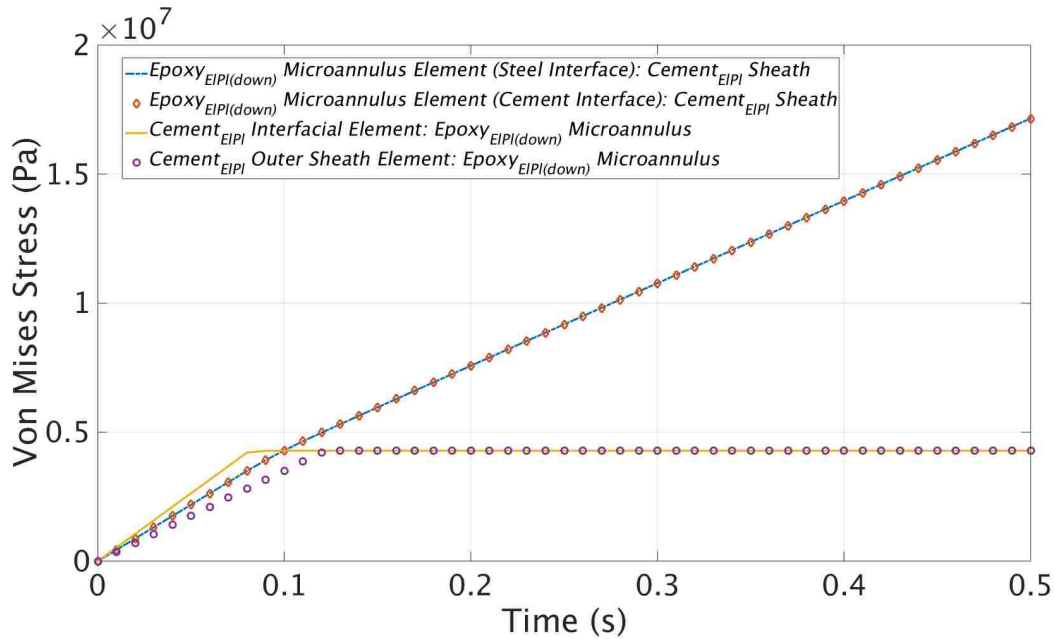
Figure 3.24: Epoxy repaired microannulus showing Von Mises stress vs. time using the following framework:
Loading: $\sigma_{conf} = 30$ MPa & $\sigma_{int} = 20.0$ MPa
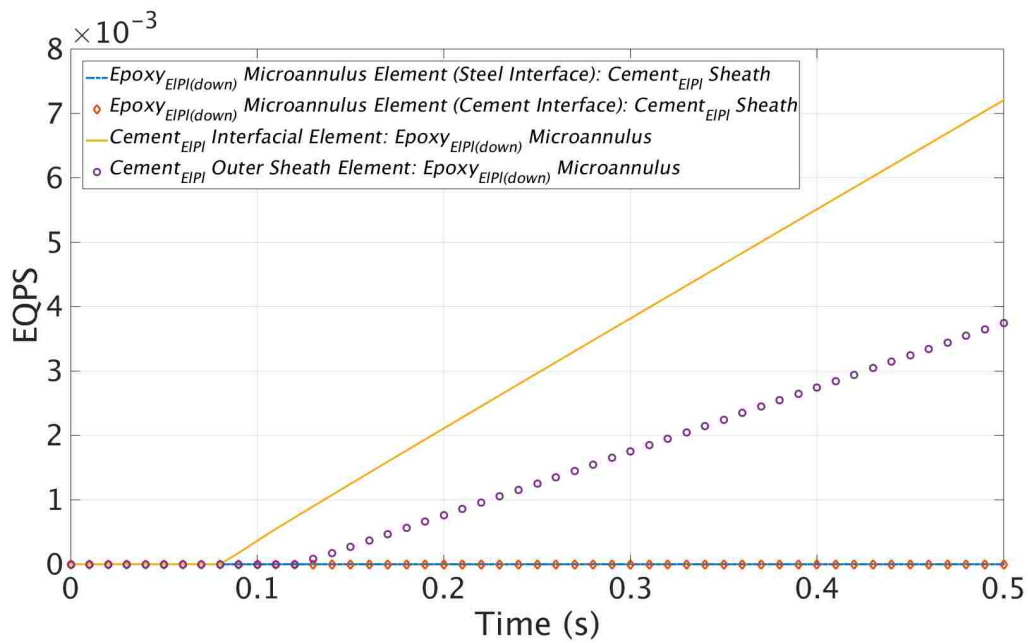
Figure 3.25: Epoxy repaired microannulus showing equivalent plastic strain vs. time using the following framework:
Loading: $\sigma_{conf} = 30$ MPa & $\sigma_{int} = 20.0$ MPa

Also shown in figure 3.26 is the equivalent plastic strain distribution across the cross section of the laboratory wellbore (elastic steel casing block not shown). It is noticed that plastic strain concentrations of 9.7×10^{-3} occur in the cement sheath at the edges of the repair material. These levels are higher than that reported in figure 3.25 along the slotted flaw microannulus mid-plane in the laboratory wellbore.
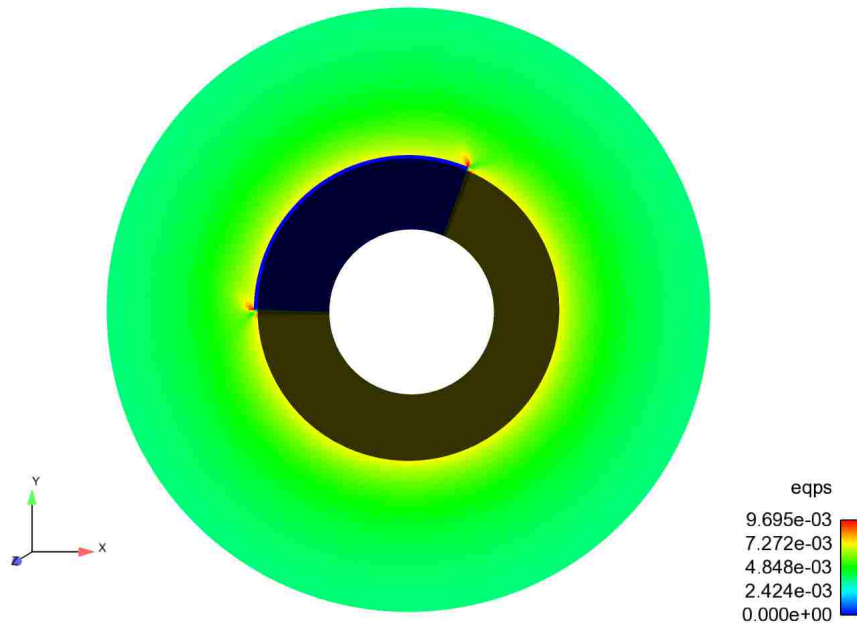
Figure 3.26: Epoxy repaired microannulus showing equivalent plastic strain at the final time-step:
Loading: $\sigma_{conf} = 30$ MPa & $\sigma_{int} = 20.0$ MPa

The material properties of the epoxy were obtained by using samples mixed with polymer concrete due to an inability to mold a pure and/or un-blended epoxy sample. To account for this possible discrepancy, figures 3.27 and 3.28 provide results from the epoxy filled microannulus simulation with the Young's modulus of the epoxy set at 1.9 GPa (decreased by one order of magnitude) and yield stress of 80 MPa (as prior). The cement sheath interfacial element reaches the same yield stress as in the cement filled microannulus and maintains this 4.28×10^6 Pa state of stress while going into plastic strain of similar magnitude. The epoxy microannulus continually supports higher stress levels throughout the simulation reaching approximately 2.2×10^7 Pa and exhibiting no plastic strain. The largest magnitude of plastic strain was seen in the cement interfacial element at 0.5 seconds, a confining pressure of 30 MPa, internal pressure of 20 MPa, and a Von Mises stress of 4.28×10^6 Pa was approximately 6.9×10^{-3} and was seen in cement interfacial element.

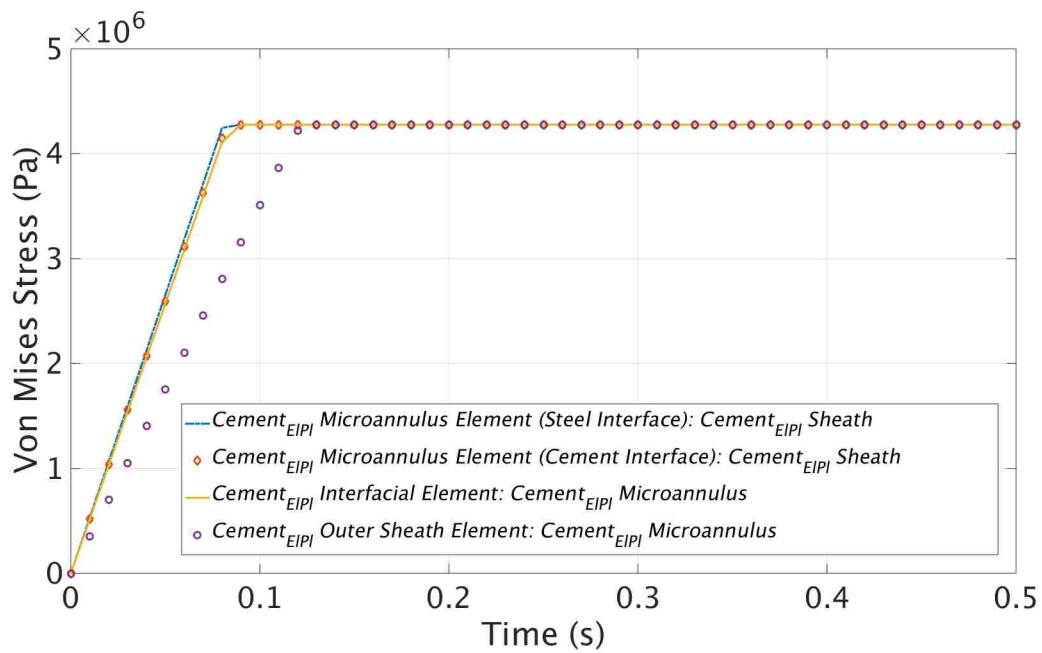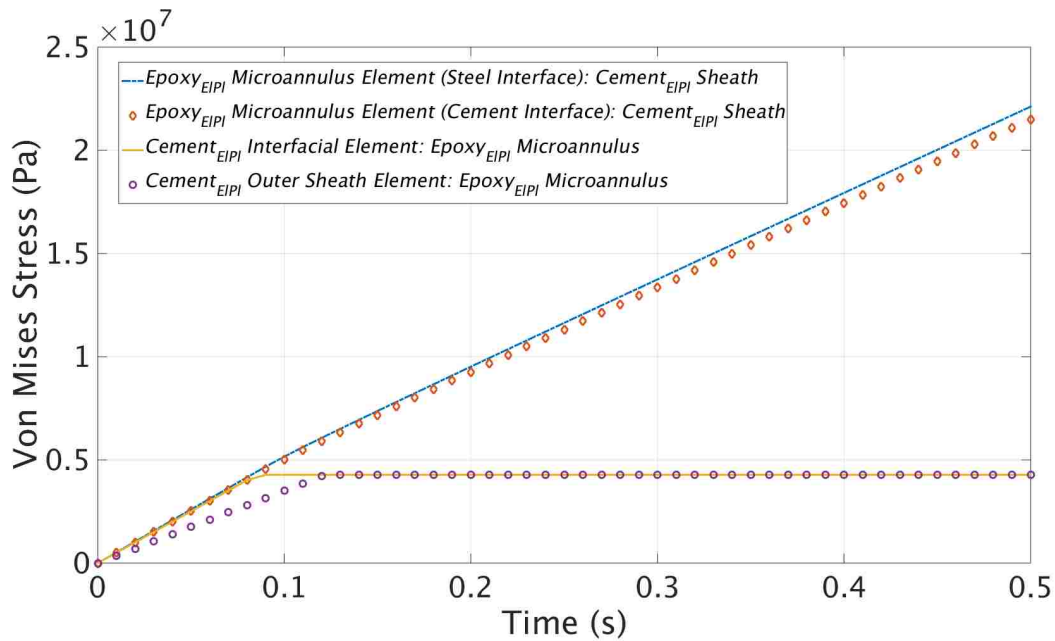Figure 3.27: Epoxy (E = 1.9 GPa) repaired microannulus showing Von Mises stress vs. time using the following framework:
Loading: $\sigma_{conf} = 30$ MPa & $\sigma_{int} = 20.0$ MPa
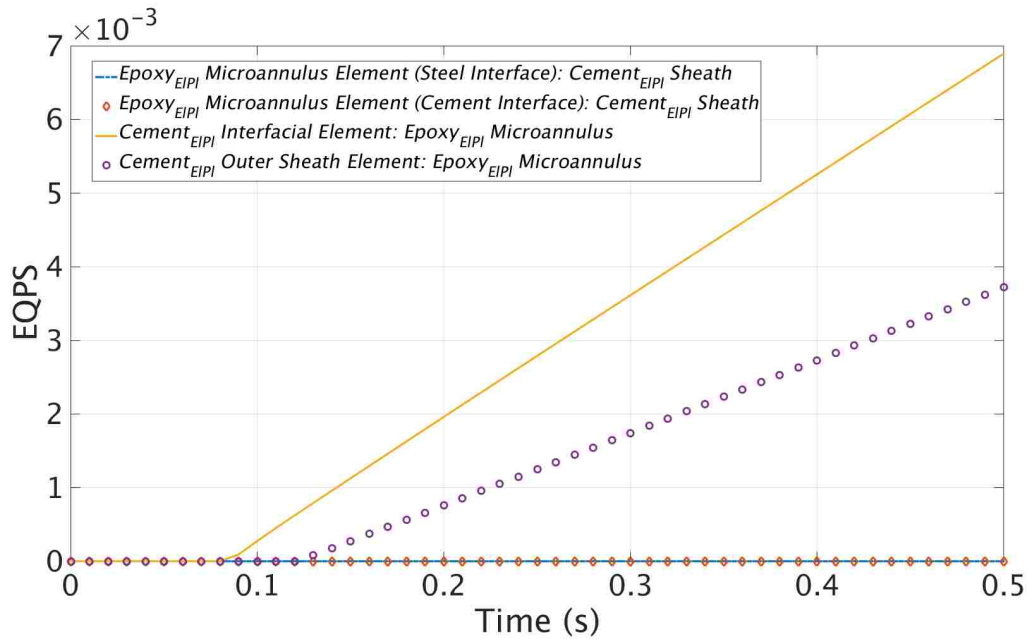
Figure 3.28: Epoxy (E = 1.9 GPa) repaired microannulus showing equivalent
plastic strain vs. time using the following framework:
Loading: $\sigma_{conf} = 30$ MPa & $\sigma_{int} = 20.0$ MPa

The ability to withstand high stress levels without failing is a favorable wellbore sealant repair material property. The wellbore seal repair material continues to sustain load beyond the preliminary yielding of cement. The continued increase in plastic strain is consistent with sealing materials that can better adapt to the changes that occur in the wellbore system after abandonment (Mainguy et al., 2007).

Axisymmetric model

An initial gap of the laboratory wellbore necessitates a frictional model such that material interfaces are appropriately described upon contact. Results from simulations with an initial 100 μm gap closing with varying casing thickness, confining pressures, and internal pressures are given in figure 3.29. Figure 3.8 shows how these pressures are ramped linearly with time.
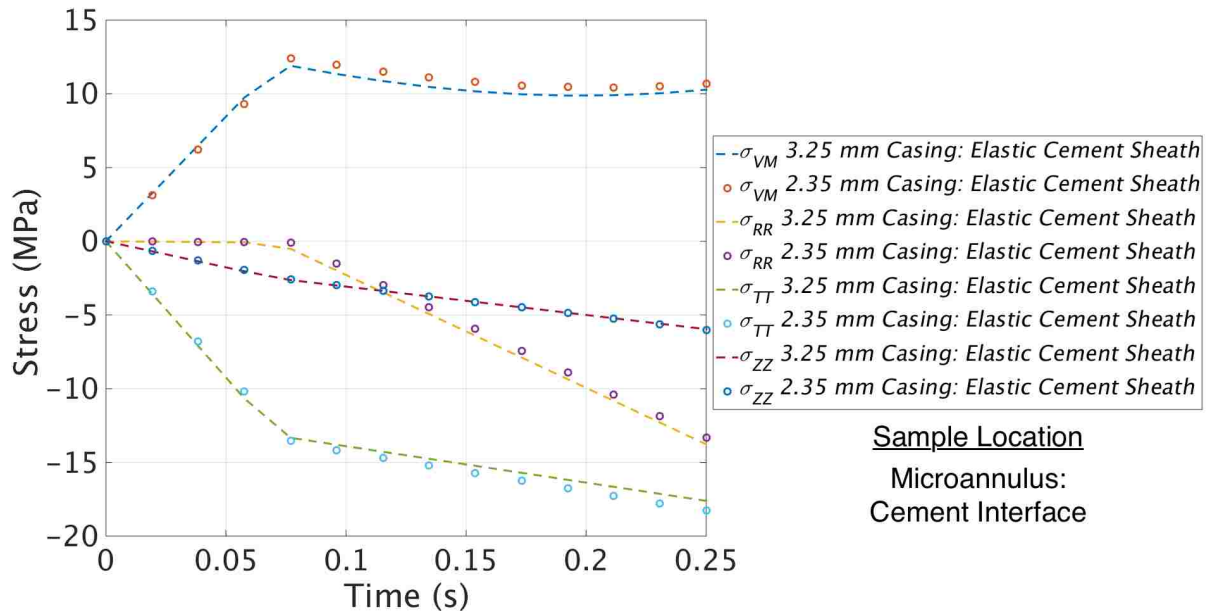
Figure 3.29: Sensitivity of varying casing sizes using the following framework: Frictional interface, 100 μm microannulus flaw, & 2.35/3.25 mm casings; Loading: $\sigma_{conf} = 15$ MPa & $\sigma_{int} = 10.0$ MPa

It is observed that contact is initiated at similar times for the 3.25 and 2.35 mm casings. A higher compressive radial stress occurs in the cement sheath for the 3.25 mm casing while the Von Mises stress is slightly lower when compared to the 2.35 mm casing. The closed form solutions presented in section 2.4.1 do not account for a cylindrical specimen with an initial flaw. However, the mechanical behavior of a cylindrical specimen in uniform contact (e.g. without flaws) described by these

equations can be used to help explain the states of stress witnessed in a flawed specimen.

The elastic solution for the radial stress in a bi-material cylinder (equation 2.28) indicates that the radial stress increases when the radial point of interest, r, decreases in value (holding all else constant); the radial dimensions for the 2.35 mm and 3.25 mm casing laboratory wellbores being 0.028825 mm and 0.030225 mm respectively as shown in table 3.1. In contrast, the hoop stress (equation 2.29) increases at greater values of r. The culmination of complex stress states for a bi-material solution is presented in terms of Von Mises stress to capture the model behavior. The perturbation in stresses at approximately 0.075 seconds in figure 3.29 is attributed to contact initiation.

The calculated Von Mises stress for an interfacial flaw repaired with cement and epoxy are shown in figures 3.30 and 3.32. Similar to the full scale model, material failure is interpreted at the time a material no longer has the ability to sustain an increasing Von Mises equivalent stress. Considering the elastic-plastic material models, it is recognized that epoxy sustains load far beyond that of the cement sheath for the 30 MPa confining pressure and 20 MPa internal pressure conditions in figure 3.30, where failure occurs at a confining pressure of 4.6 MPa and internal pressure of 3.1 MPa, yielding a 4.2 MPa Von Mises stress. When the cement properties are described by the Kayenta model, the epoxy filled microannulus sustains a higher load than when the cement sheath is characterized with elastic plastic parameters. However, a slightly higher load is sustained by the microannulus upon instituting the Kayenta cement model as a repair material as shown in figure 3.30.
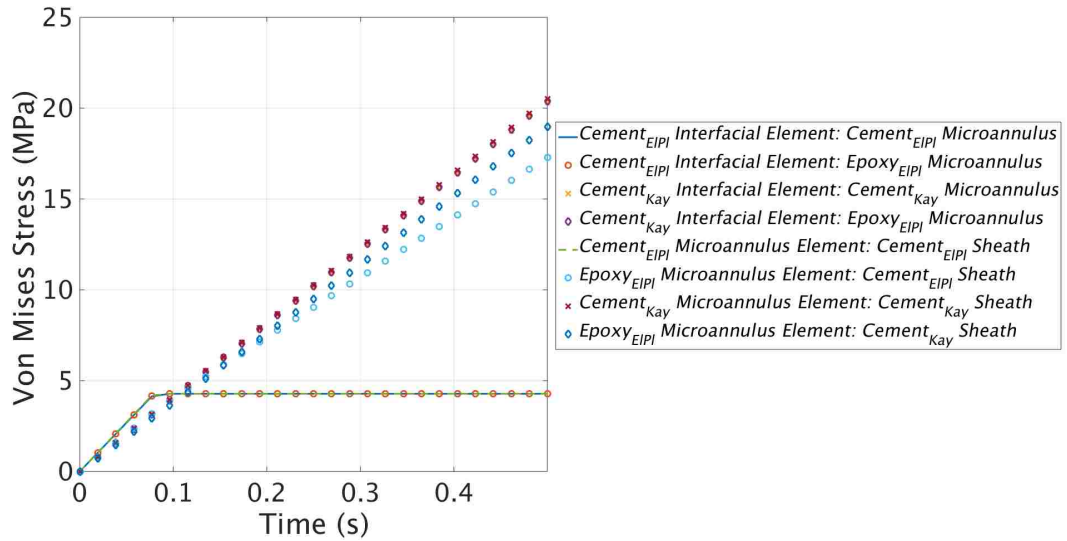
Figure 3.30: Elastic plastic cement and epoxy under confining and internal pressure
showing Von Mises Stress over time using the following framework:
Tied interface, 100 μm microannulus flaw, & 2.35 mm casing;
Loading: $\sigma_{conf} = 30$ MPa & $\sigma_{int} = 20.0$ MPa
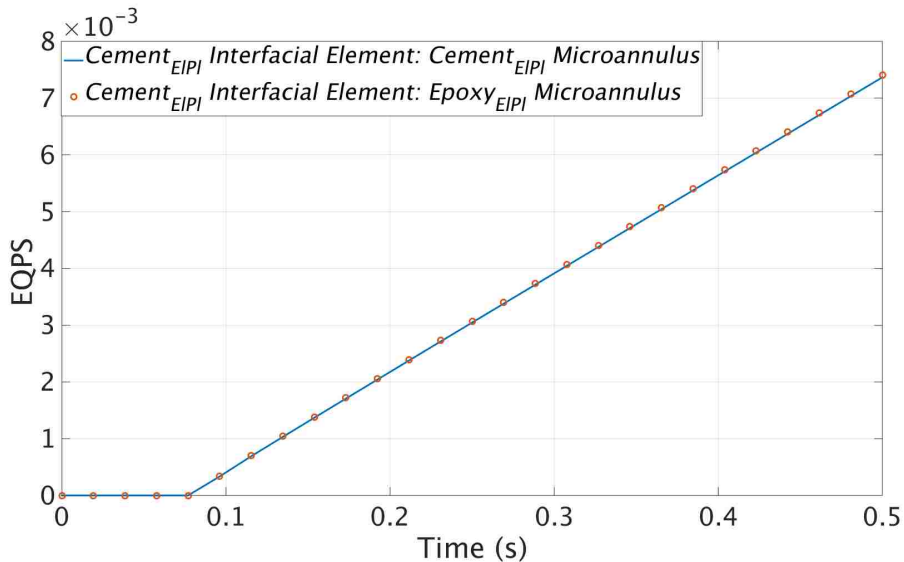
Figure 3.31: Elastic plastic cement and epoxy under confining and internal pressure
showing EQPS over time using the following framework:
Tied interface, 100 μm microannulus flaw, & 2.35 mm casing;
Loading: $\sigma_{conf} = 30$ MPa & $\sigma_{int} = 20.0$ MPa

Similarly, the 50 MPa confining pressure with no internal pressure in figure 3.32 shows the elastic-plastic cement failure occurring at a confining pressure of ≈ 5.8 MPa, yielding a Von Mises stress of 4.2 MPa. Consequently, when the laboratory wellbore is solely under confinement, a higher confining pressure is required to produce a similar Von Mises stress compared to the combined internal and external pressure scenario. These results imply that internal stress affects the stress state in cement, where an internally pressurized wellbore produces a higher Von Mises stress at the same level of confinement.
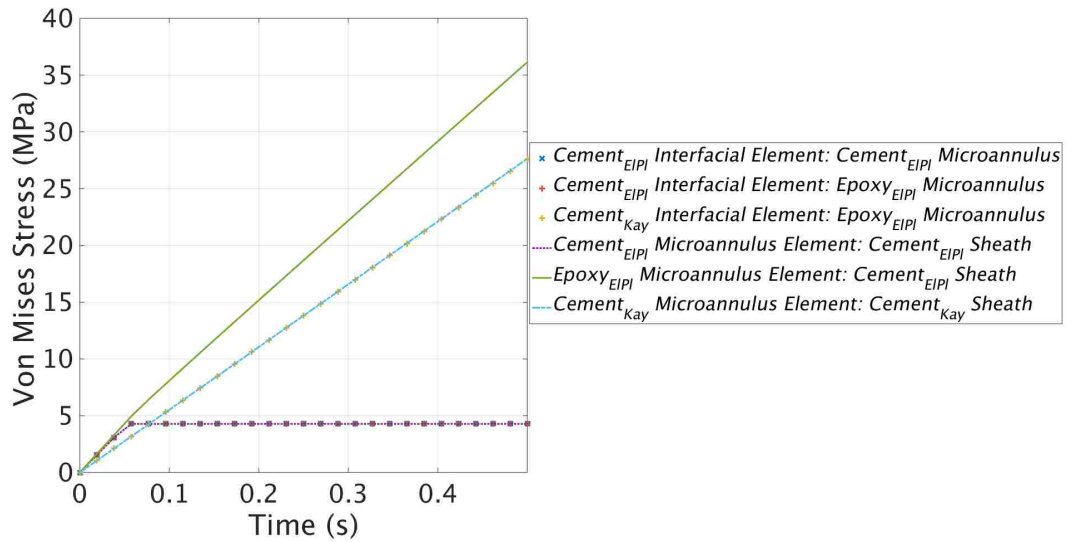
Figure 3.32: Elastic plastic cement and epoxy under confining pressure using the following framework:
Tied interface, 100 μm microannulus flaw, & 2.35 mm casing;
Loading: $\sigma_{conf} = 50$ MPa & $\sigma_{int} = 0.0$ MPa

Parametric Study Conclusions

Elastic plastic cement models show a similar Von Mises stress along the radius of the casing when the slotted flaw is repaired with a similar cement constitutive material model. The highest plastic strain occurs at the surface of the steel casing, decreasing towards the outer edge of the cement sheath. Upon repairing the slotted flaw with an elastic-plastic epoxy material, the epoxy is shown to continually support levels of stress almost an order of magnitude beyond that of cement, which is accompanied with increased levels of plastic strain. Cement sheath plastic strain concentrations occur at the edges of the repair material.

Similarly, the microannulus region of the axisymmetric model shows the elastic-plastic epoxy sustaining a significantly higher state of stress that the elastic-plastic cement counterpart. Additionally, the cement interfacial element adjacent to the microannulus shows a similar state of failure regardless if the microannulus is repaired with cement or epoxy. These results are observed consistently in the slotted flaw and microannulus models for varying internal casing and external confining pressures.

The axisymmetric model demonstrated the elastic-plastic cement material microannulus produces higher levels of Von Mises stress when subjected to an internal state of stress as opposed to being solely loaded in confinement. Upon characterizing the cement sheath with the Kayenta plasticity constitutive model in the axisymmetric loading cases, a stiffer response than that of the elastic-plastic cement constitutive model was observed; the Kayenta constitutive model portrays behavior similar to that of epoxy repair material for combined internal and external pressures. However, upon loading solely in confinement, the elastic-plastic epoxy filled repair material maintains a higher state of stress than that of a Kayenta cement repaired microannulus.

Specification of frictional interfaces between two material interfaces is only necessary when materials are initially separated by a gap. Otherwise, tied contact between the nodes of dissimilar materials accurately simulates the material boundary under axisymmetric loading conditions. Also, thin and thick steel casings have a minor effect on the state of stress between in the microannulus region, where a thinner steel casing forces the microannulus region to hold a slightly higher equivalent stress than that of a thicker casing.

Chapter 4

Modeling the Microannulus as Fracture

4.1 Introduction

Flow measurements through microannuli between cement and a steel casing were conducted by others (Stormont et al., 2015) using the experimental configuration described in chapter 3. These flow measurements were interpreted in terms of hydraulic aperture of the microannulus using the so-called cubic law defined by equation 2.1, and rewritten as equation 4.1.

$$h = (\frac{12kA}{w})^{\frac{1}{3}} \tag{4.1}$$

The hydraulic aperture vs. confining pressure data were found to be reasonably well fit with a joint closure model of Bandis et al. (1983). The same joint closure model was implemented in finite element simulations involving microannuli, but

using the applied stress acting normal to the fracture plane. Simulation results revealed that laboratory estimations of hydraulic aperture upon loading of the cement sheath and closure of the microannulus can be reasonably represented via numerical simulation. The hydraulic aperture is approximately equivalent to the mechanical aperture, which is the average deformation across an aperture. The mechanical aperture was not directly measured in this study, but could be obtained by measuring the arithmetic average aperture (Renshaw, 1995).

4.2 Experimental Data and Interpretation

4.2.1 Flow Measurements on Wellbore Samples with Flaws

Large and small microannulus flaws were created along the casing and cement interface of laboratory wellbore specimens. The large microannulus flaws on the order of 100 μm and were created by wrapping the casing in release film before the cement was cast, which was subsequently removed upon setting. Small microannulus flaws were created on a cured specimen by using liquid nitrogen or dry ice to cool the interior of the steel casing, thereby causing the steel casing to contract and debond from the cement sheath (Stormont et al., 2015). The small microannulus is on the order of 10's of μm.

The wellbore specimens were placed in the pressure vessel apparatus described in chapter 3 figure 3.1. This pressure vessel is capable of applying a range of internal casing pressures up to 20 MPa and confining pressure up to 35 MPa. Steady state and transient flow measurements were made for gas pressures of up to 15 MPa using a permeameter that connects on the upstream and downstream end of the pressure vessel; this method allowed for flow measurements along the axis of the laboratory

wellbore (Stormont et al., 2015).

4.2.2 Interpretation

Because large flows through the microannuli were sometimes measured, the flow measurements were interpreted by using the Forchheimer's equation which accounts for both viscous and inertial flow (Forchheimer, 1901). This relationship is shown in equation 4.2.

$$-\Delta P = \frac{u}{kA}Q + \frac{\beta\rho}{A^2}Q^2 \tag{4.2}$$

or commonly written in the form:

$$-\frac{\Delta P}{Q} = \frac{u}{kA} + \frac{\beta\rho}{A^2}Q \tag{4.3}$$

where ΔP is the pressure gradient, μ is the viscosity, k is the permeability, A is the cross sectional area of flow, Q is the volumetric flowrate, β is the inertial coefficient, and ρ is the density.

The Forchheimer analysis allows permeability to be interpreted from the flow measurements. The permeability values, in turn, were interpreted in terms of hydraulic aperture using the cubic law. The cubic law is widely used as an idealization for fracture flow, e.g., it does not account for fracture roughness in its simplest form. The cubic law can be used to estimate fracture aperture when permeability measurements are known and flow is assumed to occur predominately through the microannulus region.

By using hydraulic aperture data from experiments, the aperture or closure of the microannulus is taken to be equivalent to the hydraulic aperture. This hydraulic aperture is obtained as a best-fit parameter dependent on laboratory measurements described in the section 4.2.3. For example, a joint listed as 136 μm would be derived from the best fit to a series of laboratory measurements.

The flow data did not exhibit any gas-slip or Klinkeberg effects; the Klinkenberg method generally applies to low permeability media under low gas pressure.

4.2.3   Data

Assuming the fracture network is parallel to the axis of flow, the closure (ΔV) response to normal stress (σ_n) shown in equation 4.4 is plotted as shown in figures 4.1 and 4.2. The laboratory test configuration did not allow for measurement of the joint normal stress. Therefore, the instantaneous normal stress across the joint was assumed to be equivalent to the current state of confinement applied by the pressure vessel configuration.

$$\frac{\Delta V_j}{\sigma_n} = a - b\Delta V_j \tag{4.4}$$
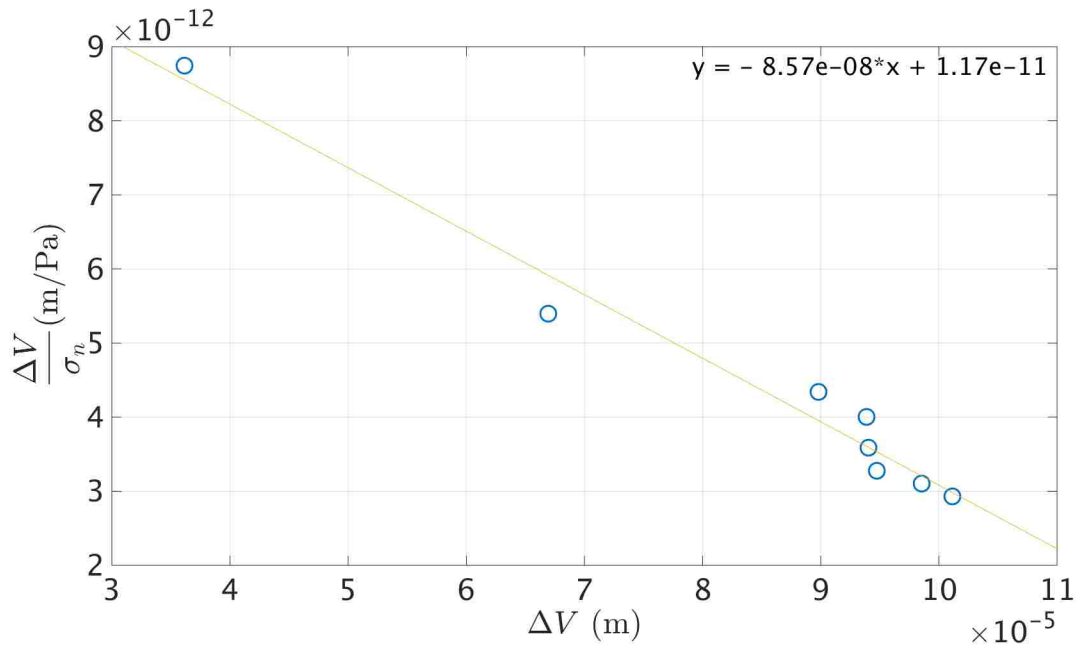
Figure 4.1: Linear fitting of a 136 μm microannulus for V_{max} and K_n determination
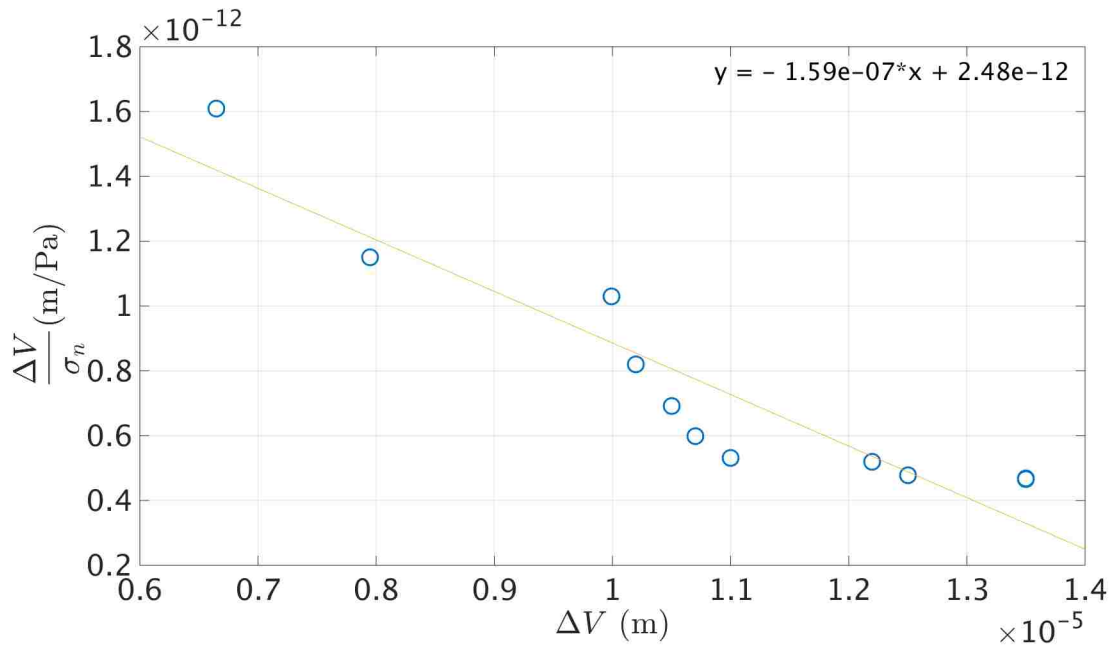
Figure 4.2: Linear fitting of a 19 μm microannulus for V_{max} and K_n determination

Stiffness and maximum closure are obtained from figure 4.1 using the linear interpolated equation $y = -8.57 \cdot 10^{-8}x + 1.17 \cdot 10^{-11}$, where $a = 1.17E - 11$ and $b = -8.57E - 8$. The maximum joint closure (V_m) is obtained when $\sigma_n \to \infty$, where $\frac{a}{b}$ is asymptotically reached in equation 4.5. The tangent joint stiffness (K_n) can also be inferred as $\frac{1}{a}$ as shown in equation 4.6 (Bandis et al., 1983).

$$\sigma_n = \frac{1}{\frac{a}{\Delta V_j} - b} \quad \equiv \quad \Delta V_j = \frac{\sigma_n a}{1 + \sigma_n b} \tag{4.5}$$

$$K_n = \frac{1}{a} = K_{ni} \tag{4.6}$$

The change in closure (ΔV) is calculated using equation 4.7. Given ΔV, theoretical aperture is calculated as $h_o - \Delta V$, or the difference between initial aperture and closure. Figure 4.3 and 4.4 compare the theoretical hydraulic aperture and laboratory measured hydraulic aperture for the $136\mu m$ and $19\mu m$ microannulus models respectively.

$$\Delta V = \frac{\sigma_n V_m}{K_n V_m + \sigma_n} \tag{4.7}$$
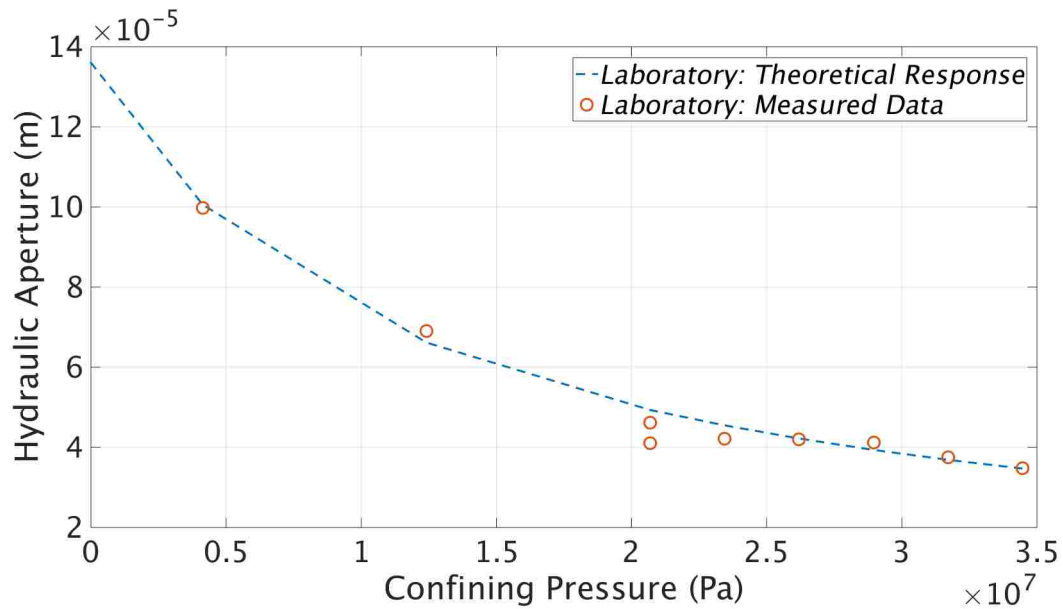
Figure 4.3: 136 μm microannulus joint relationship of hydraulic aperture and normal stress
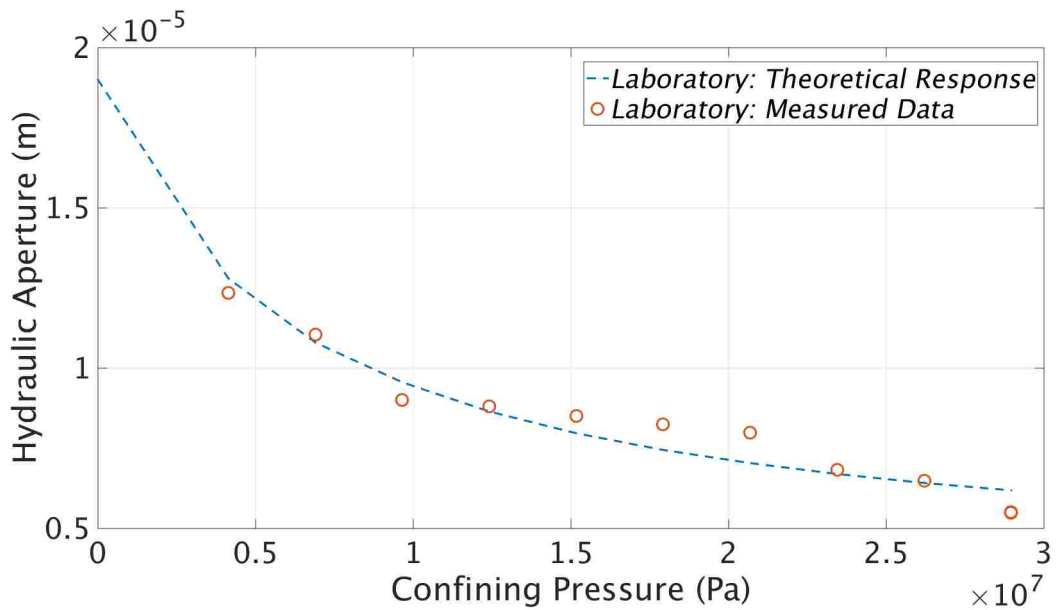
Figure 4.4: 19 μm microannulus joint relationship of hydraulic aperture and normal stress

4.3   Numerical Model

4.3.1   Approach

Stiffness elements (i.e. interfacial fracture elements) are assigned to the microannulus regions, which are intended to capture the change in aperture of the microannulus as a function of normal stress across the microannulus. These elements are shown as the mid-circumferential region in figure 4.5. Twenty microannulus interfacial fracture elements span the circumference between the steel casing (red) and cement sheath (yellow), where a local coordinate system belonging to the Kayenta material model defines a unique orthogonal system for each interfacial block; including a normal joint direction (U), orientation along the joint (V), and direction perpendicular to both of these (W). The consitutive models used to describe the geometrical specification of the joint location and the hydraulic aperture behavior of the microannulus is described in section 4.3.2.
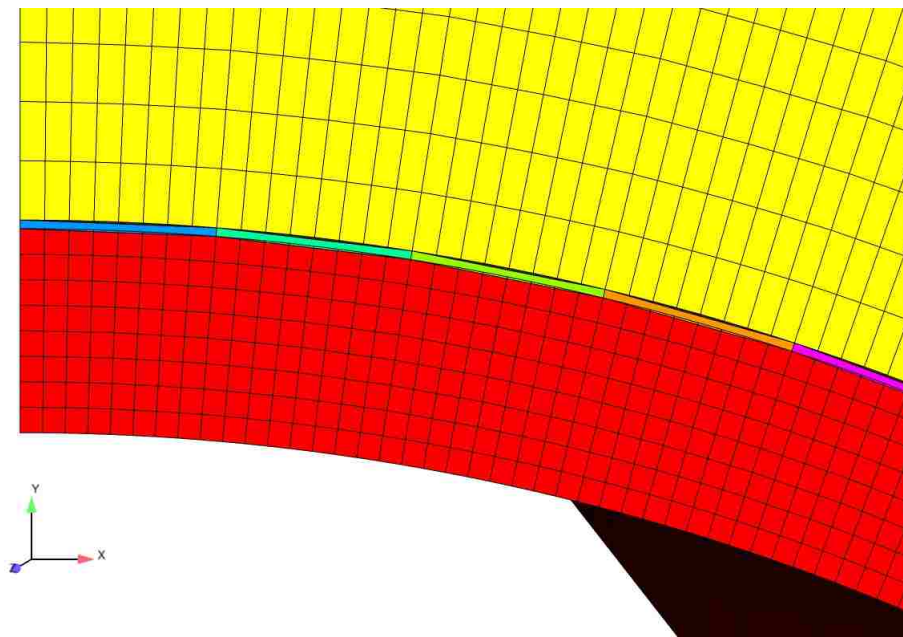
Figure 4.5: Circumferential interfacial fracture elements of the joint set

4.3.2 Material Specification

The joint specific material parameters described below contain laboratory derived parameters (CKN, VMAX, and SPACE) and geometric defined parameters (U, V, and W). Table 4.1 relates the Kayenta joint constitutive model parameters to those described by Bandis et al. (1983).

Table 4.1: Parameter equivalents of the Kayenta joint constitutive model from the equations presented by Bandis et al. (1983). The geometric joint characterization required by Kayenta (U, V, and W) allows for multiple joints to be modeled on arbitrary planes. The Bandis formulation is derived for a planar joint and therefore an approximation of these joint rotations are not required.

Kayenta Symbol	Bandis Symbol	Description	Units
CKN	K_{ni}	Initial joint normal stiffness	$\frac{stress}{length}$
VMAX	V_m	Maximum joint closure	length
SPACE	h_o	Joint spacing	length
U	N/A	Direction normal to the joint	N/A
V	N/A	Direction along the joint	N/A
W	N/A	Perpendicular to both U and V	N/A

Framework specific to interfacial joints are highlighted in figure 4.6, where the labels 01, 02, and 03 indicate the joint direction for U, V, and W. The U, V, and W joint directions are obtained from translations on the X, Y, and Z model's cartesian coordinates, respectively. This method was used to calculate unique normal directions for joints spanning along the circumference of the microannulus region. For example, U2 describes the X cartesian joint coordinate whose normal component lies in the Y' plane. Appendix C.1.2 provides an example of an arbitrary joint characterized with the joint model parameters. It should also be noted that the SPACE parameter describes the initial hydraulic aperture of the microannulus, where the meshed geometry of this flaw is explicitly generated as the width of a single element

block. Therefore, the "SPACE", "width", and "length" expressions are synonymous when describing the hydraulic aperture in this study.
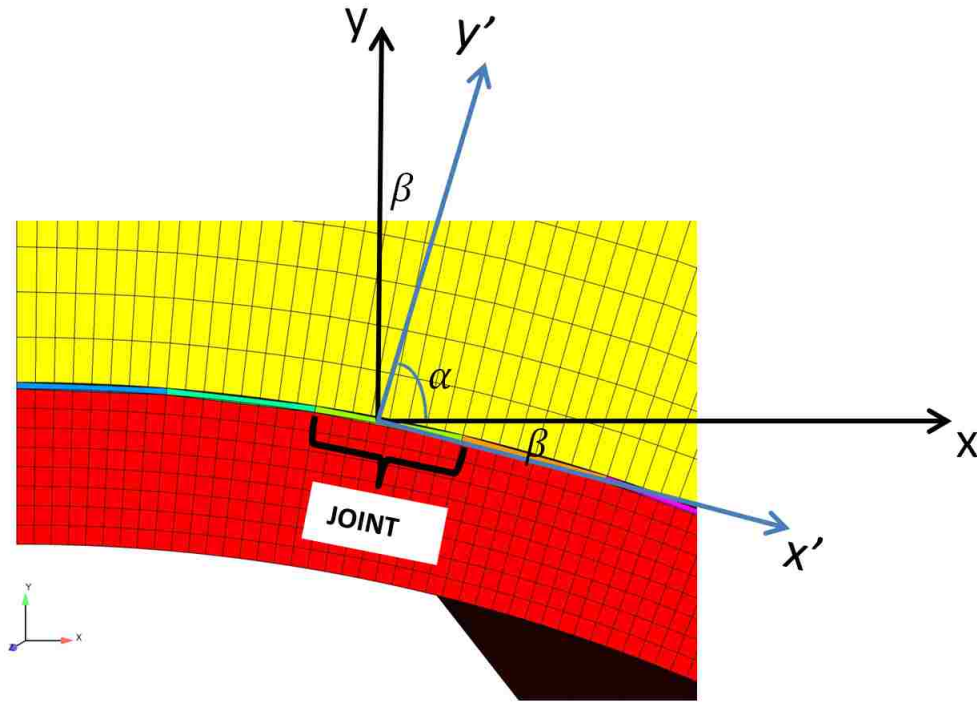
Figure 4.6: Geometrical assumptions shown for a unique interfacial fracture element of the joint set

Kayenta material properties used for modeling the cement sheath and joint set can be found in Appendix C.

4.3.3 Results

The joint parameters derived from laboratory tests were used to populate the numerical model of the microannulus. Figures 4.7 and 4.8 compare the laboratory results for the large (136 μm) and small (19 μm) microannuli with the numerical results. Both microannulus sizes were analyzed with the cement sheath parametrized with

an elastic and Kayenta constitutive model using the parameters defined in Appendix C. Numerical implementation reveals the finite element joint behaving slightly stiffer than the laboratory measured values in the 136 μm microannulus model. Figure 4.7 also displays the large microannuli with an initial stiffness at 80% of its laboratory derived value.
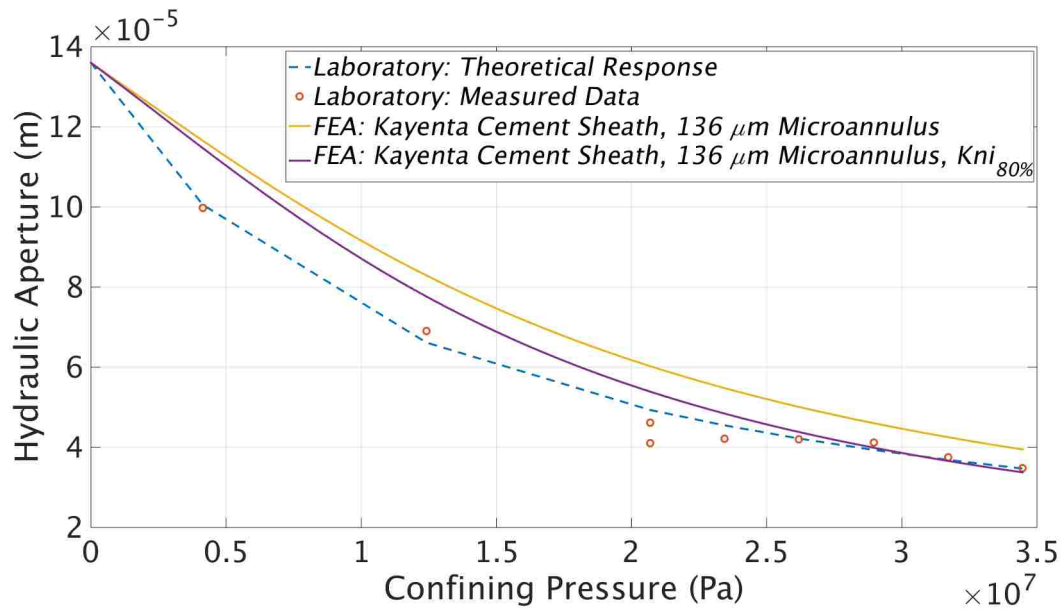
Figure 4.7: Laboratory measurements and numerical model comparison for the 136 μm microannulus joint
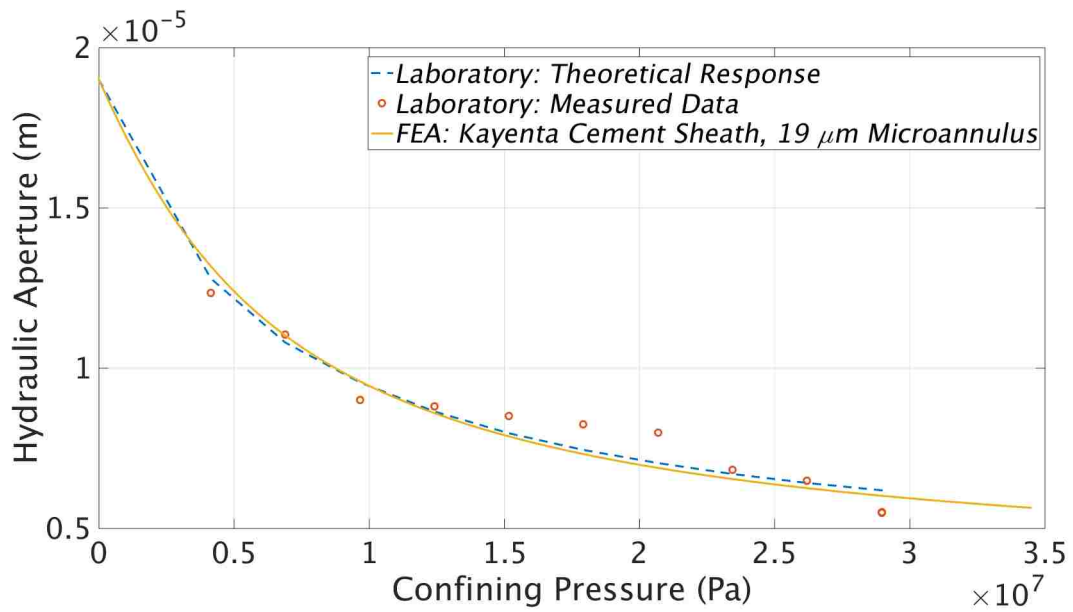
Figure 4.8: Laboratory measurements and numerical model comparison for the 19 μm microannulus joint

Given these apertures, permeability can be back calculated using equation 4.1. Figure 4.9 shows an initial permeability on the order of 3.2E-13 m^2 for the 136 μm microannulus model and 6.8E-16 m^2 for the 19μm microannulus model, where microannuli or less significant fractured rock exhibit permeability on the order of 10E-6m ^{2} to 10E-9m ^{2} (note: 1 Darcy = 10E-12 m^2). After 34 MPa confinement the permeability is reduced to 7.8E-15 m^2 and 1.8E-17 m^2 for the 136 μm and 19 μm microannulus models respectively, where permeability of intact cement is approximately 10.0E-18 m^2 (Bear, 2013). Therefore upon applied confinement of 34 MPa, an unrepaired wellbore microannulus can exhibit permeability approximately one to two orders of magnitude higher than that of intact cement. The permeability values presented assume a parallel-type plate flow model.
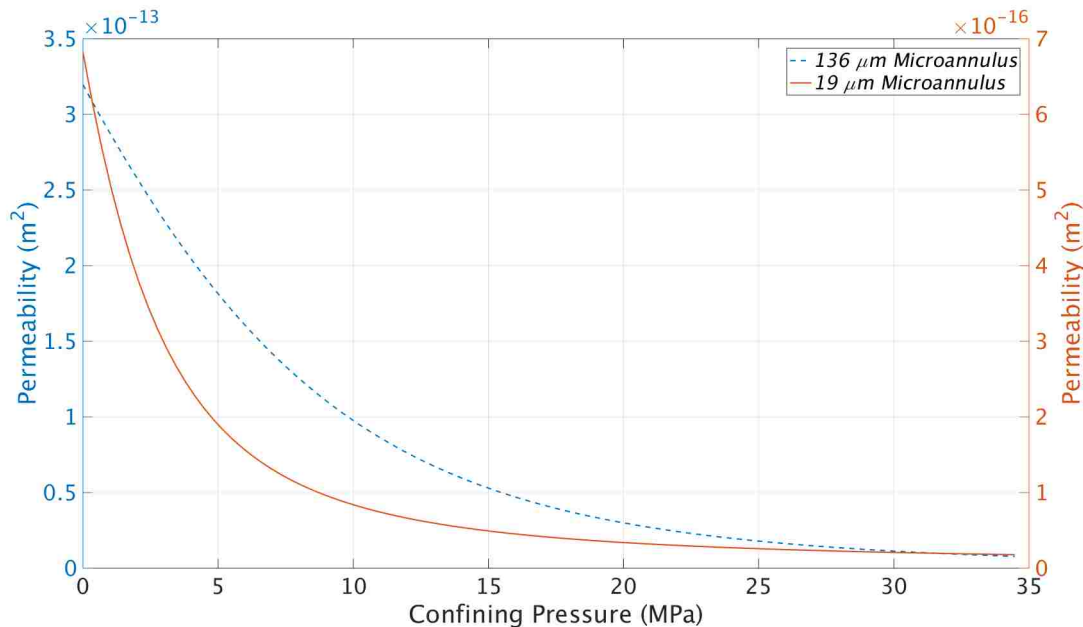
Figure 4.9: 136 μm and 19 μm microannulus joint permeability shown upon increasing confinement pressure

The contact normal stress across the face of the microannulus is shown against confining pressure in figure 4.10. The behavior between these two parameters are

non-linear due to the hyperbolic nature of stiffness changing over the contact stress as shown in figure 4.11. The 136 μm joint aperture shows to be less stiff than the 19 μm joint aperture with increasing normal stress applied to the microannulus. The hydraulic aperture is represented as a function of contact stress for the 136 and 19 μm joints in figure 4.12.
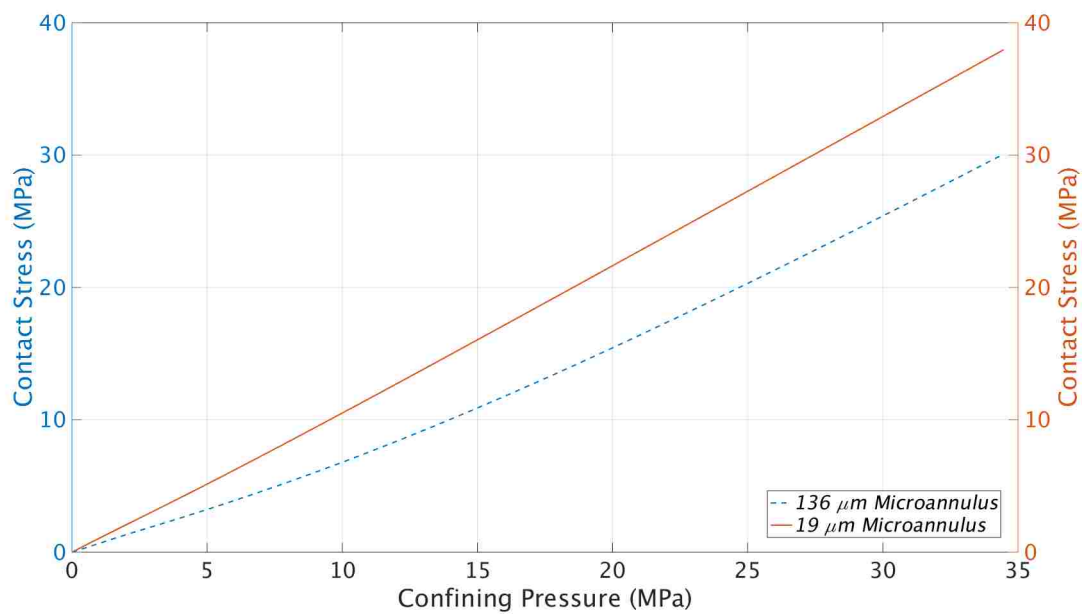
Figure 4.10: 136 μm and 19 μm microannulus joint contact stress and confinement pressure relationship
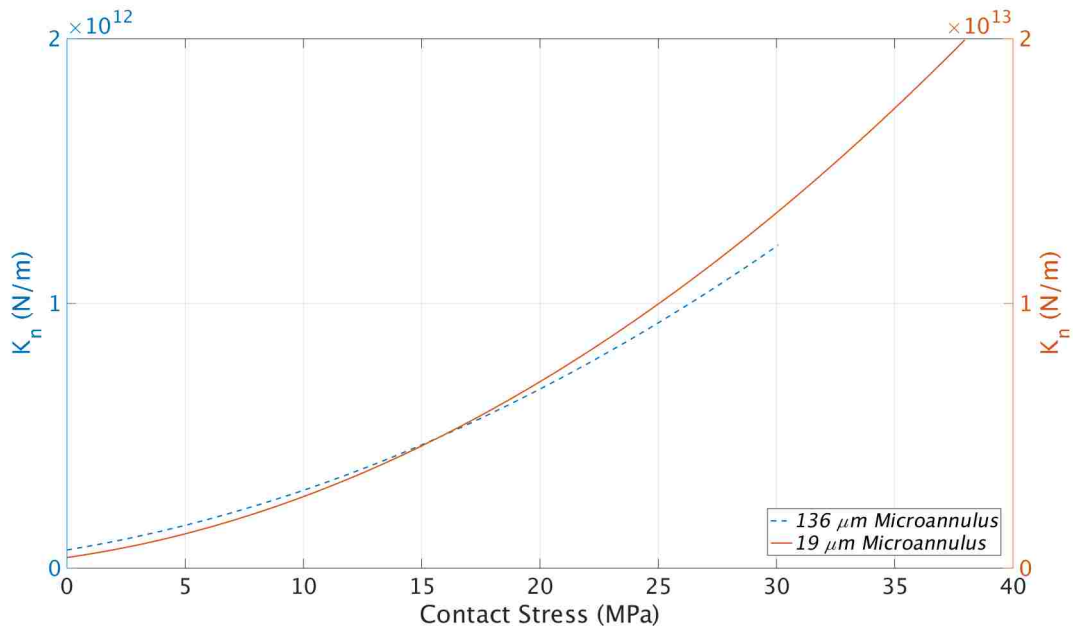
Figure 4.11: 136 μm and 19 μm microannulus joint stiffness and contact stress relationship
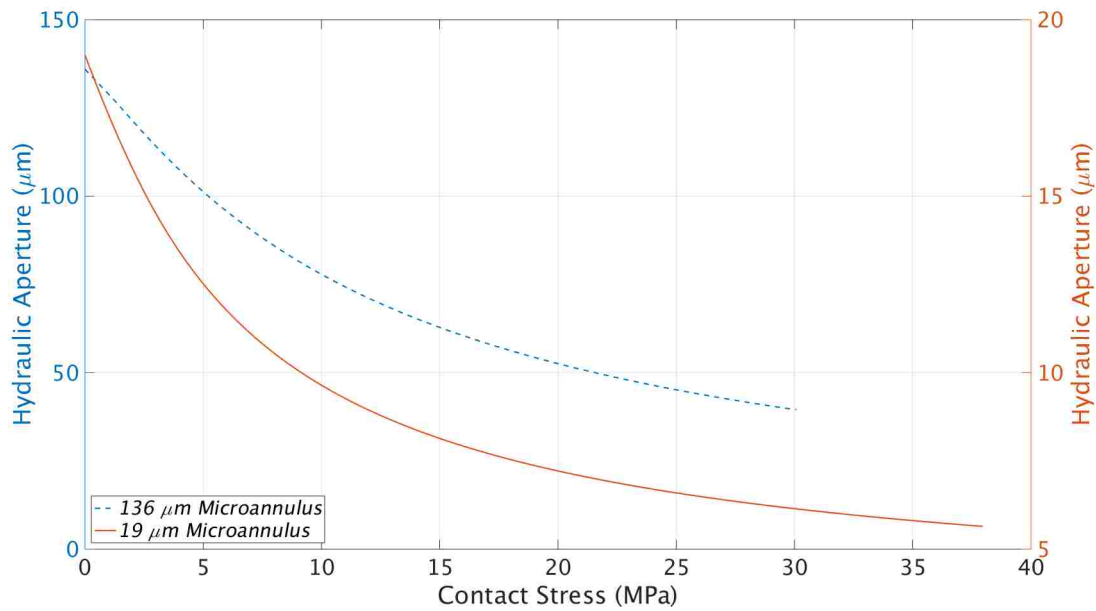
Figure 4.12: 136 μm and 19 μm microannulus joint hydraulic aperture and contact stress relationship

4.3.4 Discussion

When comparing laboratory and numerical results of the microannulus' aperture closure, slight variability in response to confining pressure is noticed. The final state of closure results for the large (136 μm) and small (19 μm) microannulus shown in figures 4.7 and 4.8 deviate approximately 4 μm and 0.2 μm respectively between laboratory and numerical results. Therefore, as the microannulus gap decreases in size, the difference in laboratory and numerically measured hydraulic apertures at the final state of confinement lessens. As such, it is appropriate to consider ways in which the microannulus was in-appropriately modeled.

As previously discussed, the "cubic law" is used to obtain an estimation of the hydraulic aperture, which in turn can be assumed equivalent to the mechanical aperture. Under high flow rates and large apertures, it is a good assumption that the mechanical and hydraulic aperture are equivalent. However, this assumption can break down when fracture aperture approaches the scale of the surface roughness (Iwai, 1976; Renshaw, 1995). In this study, the surface roughness between the steel casing and cement sheath was accounted for by adjusting the stiffness based on the model of Bandis et al. (1983). Therefore, the comprehensive description of the microannulus entails embedding the microannulus roughness features in the model. However, by accounting for the surface roughness as a fitting coefficient, it is possible that the in-homogeneous nature of the surface roughness present along the microannulus flaw can provide a more consistent representation of hydraulic aperture closure. Explicitly incorporating the surface roughness in a model of microannulus behavior would require characterizing and parametrizing the surface roughness, which may be difficult.

Laboratory data error could be present in the assumption that the microannulus behaves as a purely hydraulic aperture and is averaged along the flaw circumfer-

ence. Additionally, the deformation of the hydraulic aperture is estimated by the stress normal to the fracture plane (i.e. microannulus). Joint parametrization using laboratory data assumed that the joint normal stress is equivalent to the confining pressure, while numerical simulations used the stress normal to the fracture plane.

Numerical model error could be present in an insufficient definition of material behavior, e.g. the cement sheath, or in the geometrically homogeneous definition of the microannulus joint along the circumference of the cement sheath and steel casing interface. The numerical implementation for the microannulus behaves in response to normal joint behavior in a hyperbolic manner as discussed by Bandis et al. (1983). Future studies should also consider the joints response to shear loading (in addition to normal loading) as presented by Souley et al. (1995). To numerically model shear response, shear stress and shear displacement data on a laboratory wellbore will be needed for constitutive model parametrization.

Hysteresis

Hysteresis affects can alter the joint aperture during the loading and unloading phase (Souley et al., 1995). However, the Kayenta constitutive model implemented for the joint does not have history dependent properties. The numerical and laboratory results of this phenomenon are shown in figure 4.13.
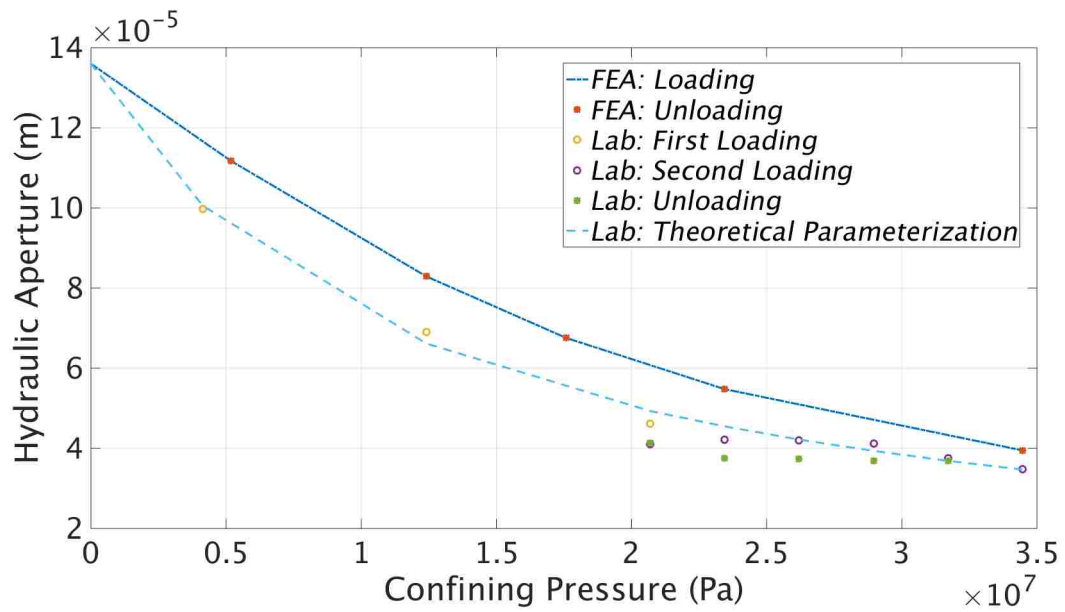
Figure 4.13: Laboratory measurements and numerical model comparison of hysteresis effects on the 136 μm microannulus joint.

Microannulus Sensitivity

The joint model used to describe the microannulus behavior requires three laboratory derived model inputs (in addition to geometerical specification), two of which describe the mechanical behavior as discussed in section 4.2.3 and 4.3.2; the parameters that describe mechanical behavior being "CKN01" (Kni) and "VMAX1" (Vmax) while the geometrical property of joint spacing is described through the "SPACE" variable. Because there is only a single joint spacing across the microannulus, this variable is simply the width, or initial aperture, of the microannulus.

The mechanical properties of the 136 μm microannulus were deviated by an order of magnitude, both increased in decreased, to better investigate the sensitivity of the joint model and discover if a different set of parameters can better describe the observed joint behavior. Figure 4.14 shows this behavior where "X_o" (naught) denotes the laboratory derived parameter for that variable was implemented, while "X_{up}" and "X_{down}" denotes the variable was perturbed by an order of magnitude higher and lower respectively. An example of this implementation is shown in table 4.2.

Table 4.2: An example of how laboratory derived parameters are altered for joint sensitivity analysis

Model Adjustment	Figure Symbol	Value
CKN01	K_{ni}	8.62E+10
VMAX	V_m	1.36E-4
$CKN01_{up}$	Kni_{up}	8.62E+11
$VMAX_{down}$	Vm_{down}	1.36E-5
$CKN01_{down}$	Kni_{down}	8.62E+9
$VMAX_{up}$	Vm_{up}	1.36E-3
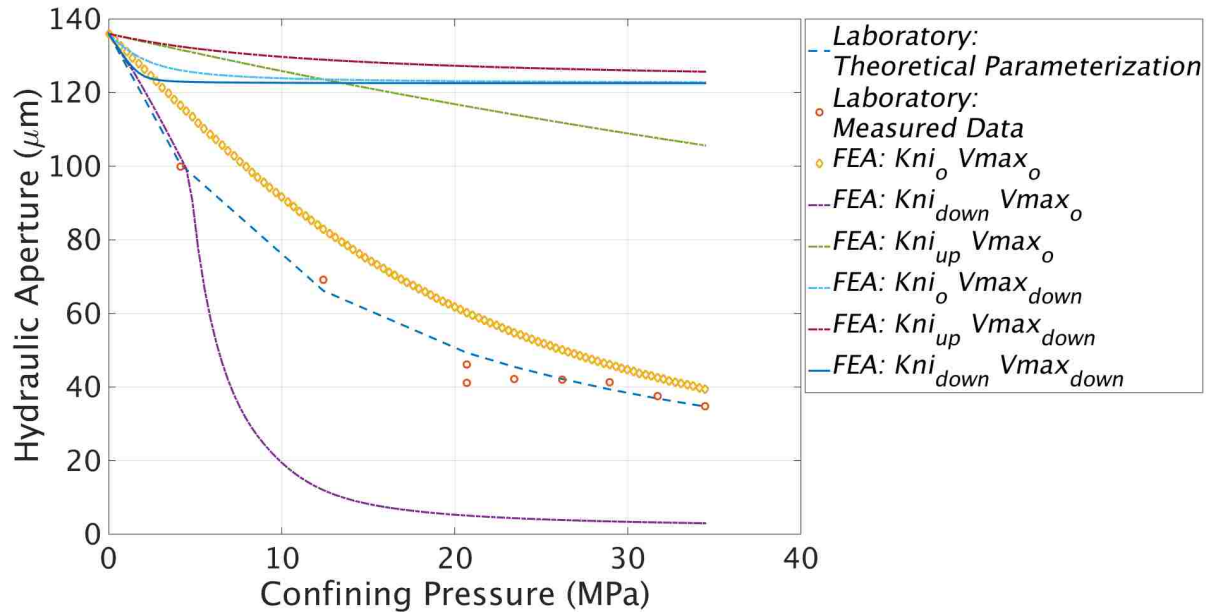
Figure 4.14: Sensitivity analysis on laboratory derived parameters (Vm and Kni) used for constitutive model parametrization of the joint.

The results obtained from the sensitivity analysis are given in figure 4.14. When Kni_{up} and $Vmax_{down}$ are used in the model, the hydraulic aperture is stiff and has limited closure upon change in confinement. In contrast, when Kni_{down} and $Vmax_{naught}$ are used in the model, the hydraulic aperture is soft and has the highest closure upon change in confinement. The laboratory derived parameters are most closely represented by the theoretical derived parameters (Kni_{naught} and $Vmax_{naught}$) of hydraulic aperture closure upon confinement. Figure 4.15 shows how the representation of hydraulic aperture can become non-physical.
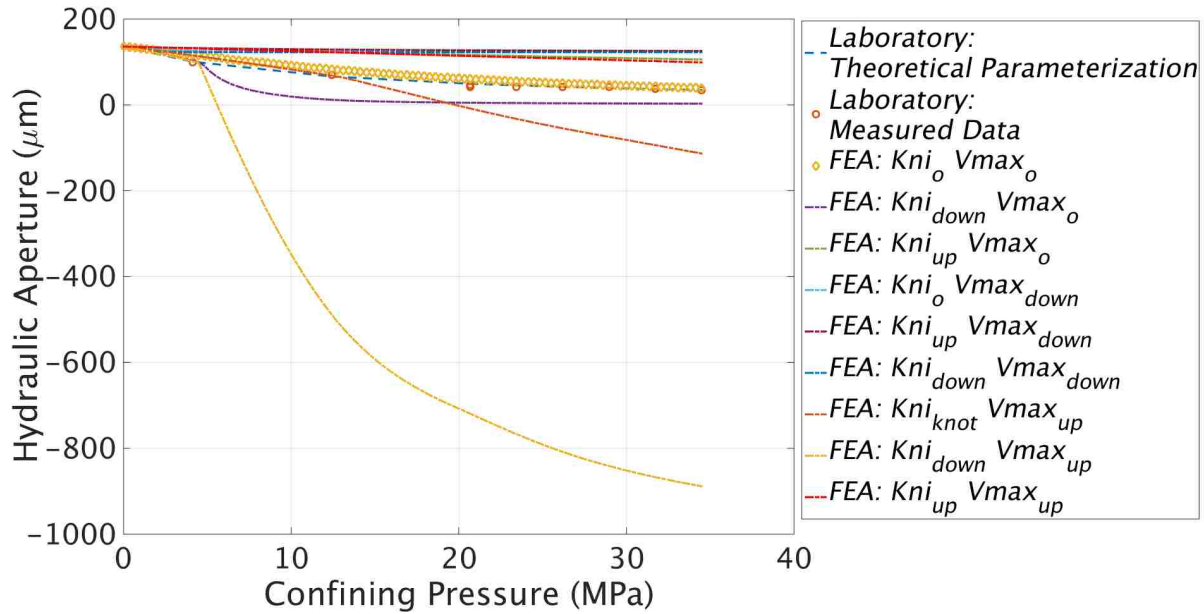
Figure 4.15: Sensitivity analysis on laboratory derived parameters (Vm and Kni) used for constitutive model parametrization of the joint.

By increasing the maximum closure by an order of magnitude ($Vmax_{up}$) and implementing stiffness parameters of Kni_o or Kni_{down}, the hydraulic aperture goes negative in figure 4.15. Therefore, when the maximum closure is increased by an order of magnitude this model exhibits an unphysical configuration of the joints ability to close beyond that of its original size. However, by increasing the stiffness an order of magnitude (Kni_{up}), physical (i.e. positive) measurements of hydraulic aperture are obtained in an unphysical representation of maximum closure ($Vmax_{up}$).

Forward Prediction

The numerical models, whose behavior is parametrized from laboratory data, have thus far been demonstrated for the same confining pressure loading conditions imposed in the laboratory to obtain the data. To substantiate the model, it is necessary to apply loading conditions on the numerical model other than those by which they

are derived and compare these results to laboratory measurements.   Figure 4.16
shows the 136 μm microannulus with a constant confining pressure of 13.78 MPa
with an increasing internal casing pressure, where deviation between numerical and
experimental data is maintained below 3 μm.
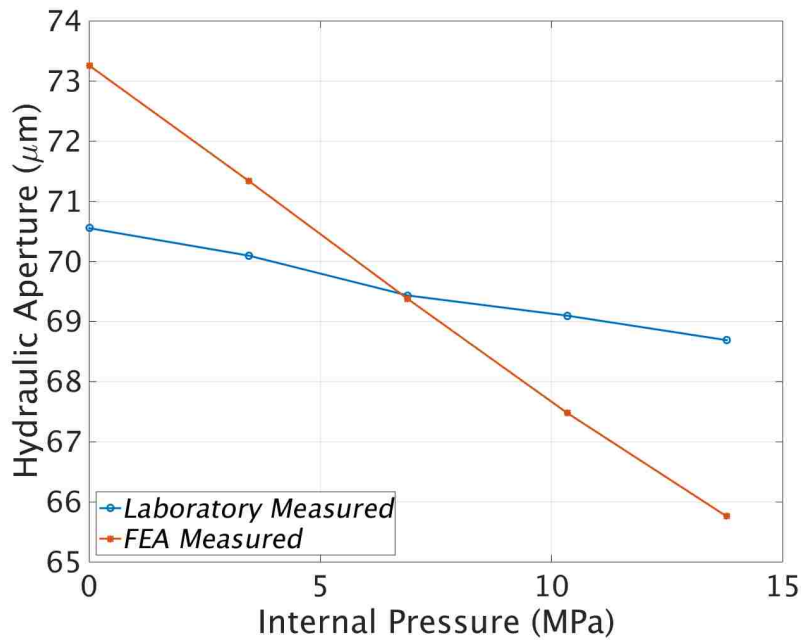
Figure 4.16: Forward prediction of the axisymmetric laboratory wellbore 136 μm
microannulus; results are shown with increasing internal pressure against a
confining pressure of 13.78 MPa

The contrasting behavior for between numerical and experimental data for the
19 μm shown in figure 4.17 is hypothesized to be a result of a radial fracture in
the laboratory wellbore. It is prevalent that the laboratory expression of hydraulic
aperture erroneously increases with an increasing internal pressure and constant
confining pressure of 4.14 MPa while the numerical data for the 19 μm behaves
in a non-fractured and theoretically hyperbolic decreasing manner.
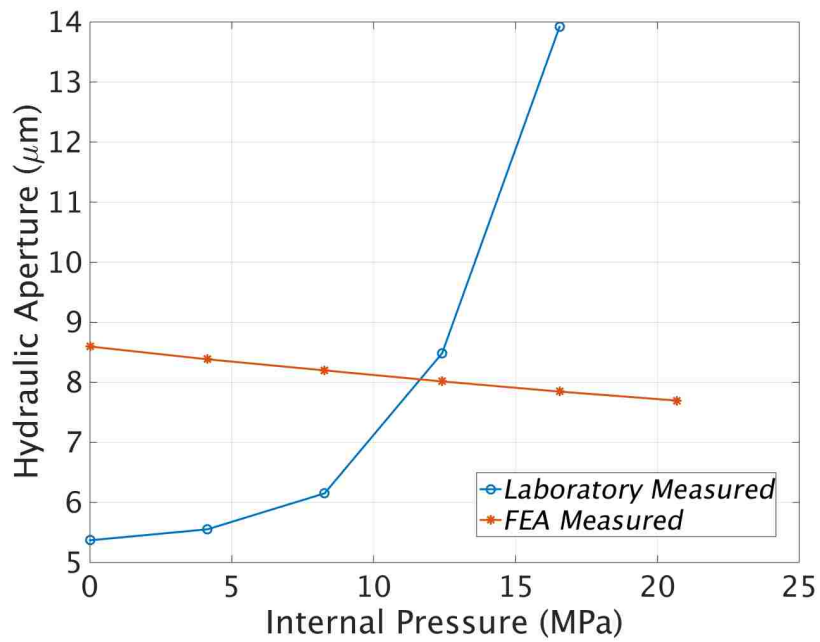
Figure 4.17: Forward prediction of the axisymmetric laboratory wellbore 19 μm microannulus; results are shown with increasing internal pressure against a confining pressure of 4.14 MPa.

Chapter 5

Conclusions and Recommendations

5.0.1 Parametric Study

The microannulus region to the casing-cement interface was modeled as perfectly bonded, frictional, or open, either around the entire circumference or over a portion of it. Repair materials were modeled in the microannulus region as an elastic-plastic epoxy nano-composite material and various cement constitutive models including elastic, elastic-plastic, and the "Kayenta" CAP plasticity constitutive model. Loading combinations of internal casing pressure and external confining pressure were applied to the full scale and axisymmetric laboratory wellbore model.

By conducting simulations with a range of material properties and loading conditions, the importance of material properties in a microannulus space between the steel casing and cement sheath was determined to be significant for mechanical integrity of the wellbore system (e.g. thermal and chemical induced stresses were not considered). When a wellbore is subject to elevated external confining and internal casing pressures experienced in-situ, microannulus flaws in-between the steel casing and cement sheath can lead to failure within the cement sheath. These defects may

lead to pathways for CO_2 migration out of reservoir storage. The novolac epoxy with carbon nanotubes injected into the flaw space of the microannulus proved to be ductile enough to withstand the proposed conditions without failing. Having the ability to sustain levels of stress with increasing deformation limits the potential for high permeability pathways in the wellbore system.

The major conclusions are:

- Repairing the slotted flaw with an elastic-plastic epoxy material, the epoxy supports levels of stress, accompanied with increased levels of plastic strain, beyond that of an elastic-plastic cement. Also, strain concentrations occur at the edges of the repair material in the slotted flow.

- Internal stress affects the stress state in cement, where an internally pressurized wellbore produces a higher Von Mises stress at the same level of confinement.

- The constitutive model implemented to define the model is shown to have significant ramifications to material response. For example, a stiffer response than that of the elastic-plastic cement constitutive model was observed when the cement sheath is characterized with the Kayenta CAP plasticity constitutive model.

- The elastic-plastic epoxy filled repair material maintains a higher state of stress than that of a Kayenta cement repaired microannulus when the cement sheath is loaded in confinement. The plastic strain in the cement sheath adjacent to the repair material is not significantly different relative to varying repair materials.

- Tied contact between the nodes of dissimilar materials accurately simulates the material boundary under axisymmetric loading conditions. That is, frictional

interaction between the material interfaces was shown to be non-consequential due to the uniform loading conditions of the laboratory wellbore pressure vessel system.

- The microannulus region exhibits a higher equivalent stress for a thin casing compared to thick casing, however this effect was minor.

The recommendations for future work are:

- Repeat the analysis with radial fractures in the cement. Damage models such as XFEM or phase-field methods in Sierra Solid Mechanics can be used to model the cement sheath failure by explicit cracks.

- Implement a temperature dependent framework for material response.

- The model for the microannulus should be evaluated to determine if it captures change in aperture as a function of pore pressure.

    – This shall be a continuum approach to calculate effective stress, the difference between externally applied stresses and internal pore pressure; where pore pressure has effects on rock strength, frictional strength, and elastic moduli.

    – Implementing a user-subroutine, this pore pressure will systematically update the principal stresses and implement the Kayenta constitutive material model to accurately simulate in-situ conditions and provide more sophisticated constitutive laws for cement behavior. For example, Kayenta has the capability to implement the Biot constant for an effective stress calculation, which provides an exact form of volumetric strain through implementation of the drained bulk modulus of porous rock and bulk modulus of solid grains.

- Show the microannulus joint model effects on a large scale wellbore system containing multiple stratigraphic rock formations and injection from CO_2 sequestration operations. The response of this microannulus flaw can also be shown in a repaired state using the proposed nanocomposite epoxy wellbore seal repair material.

5.0.2 Modeling the Microannulus as a Fracture

Large and small microannulus flaws were created along the casing-cement interface of laboratory wellbore specimens. Flow measurements were interpreted by means of the Forchheimer's equation, which also permits an interpretation of permeability. The permeability on laboratory wellbore specimens with imposed flaws were then interpreted in terms of hydraulic aperture of the microannulus using the so-called cubic law (a widely used idealization for fracture flow). Stiffness and maximum closure of the joint can be inferred from hydraulic aperture closure as a function of confinement measured for the laboratory wellbore system. These parameters are used to parametrize the numerical constitutive model for various joint sizes.

Laboratory estimations of hydraulic aperture upon loading of the cement sheath and closure of the microannulus can be reasonably represented via numerical simulation. This computational capability allows for modeling a variation of flawed systems that contain complex physics including varying stiffness with applied confinement; where sample preparation and testing can otherwise be a laborious process. These methods can provide significant application to the science of wellbore integrity.

The major conclusions are:

- Representing the microannulus with a joint model provides a means to predict the hydraulic aperture under varying conditions which in turn can be inter-

Chapter 5. Conclusions and Recommendations

preted as permeability.

- The hyperbolic change in joint normal stiffness can be numerically extracted as a function of contact normal stress across the face of the microannulus. The hydraulic aperture and joint stiffness can be defined in terms of contact stress in the microannulus, in addition to the state of confining pressure by which laboratory parameters were derived.

- Numerical modeling of the microannulus must be case specific when using the joint characterization method proposed by Bandis et al. (1983). That is, it is possible to obtain non-physical results if the stiffness, initial joint spacing, and the maximum joint closure are not parametrized to the discrete microannulus of interest.

- It is possible to forward predict the hydraulic aperture when undergoing arbitrary internal casing and external confinement loading scenarios upon parametrization under the framework proposed by Bandis et al. (1983) (assuming a non-fractured regime).

The recommendations for future work are:

- Surface roughness variation between the large and small scale microannuli could be present due to the varying methods used to create flaws. While Bandis et al. (1983) suggest that the joint closure is not likely size dependent, they state the most crucial component to joint stiffness is surface roughness. Therefore, a better understanding of the surface roughness created by varying techniques to create the microannulus can provide insight into the material response.

- Attempt to create a single constitutive element comprising the mechanical aspects of the entire wellbore system. This will involve up scaling the joint frac-

ture model, where the stiffness of the wellbore system systematically changes as a function of stress.

- The joint's response to shear loading, in addition to normal loading, should be considered in future studies. To numerically model shear response, shear stress and shear displacement data on a laboratory wellbore is needed for constitutive model parametrization.

Appendices

Appendix A

Bed Slipping Rock Formation

The final component sealant repair material evaluation uses a wellbore-scale model. Wellbore modeling is being used to quantify the stresses and strains that sealant repair materials will face in the wellbore environment. The material properties of the developed nanocomposites were obtained in the bench-scale laboratory experiments and corresponding analyses. The field scale model provides the stress-strain environment that will be applied to the wellbore. This data will also be used as input for the wellbore model to predict the response of the synthesized nanocomposites. Two separate wellbore-scale models have been developed during this study. The first model includes steel casing(s); cement surrounding the casing(s); and formation rock around everything, and was designed to evaluate the stresses induced on casing materials under shear loading (Gomez et al., 2013; Matteo et al., 2014). The computational domain included two different bedded geologic media with a horizontal slip plane between them as seen in figure A.1.

Displacement boundary conditions arising from slippage along the slip interface were imposed on the boundaries of the wellbore model to simulate shearing and
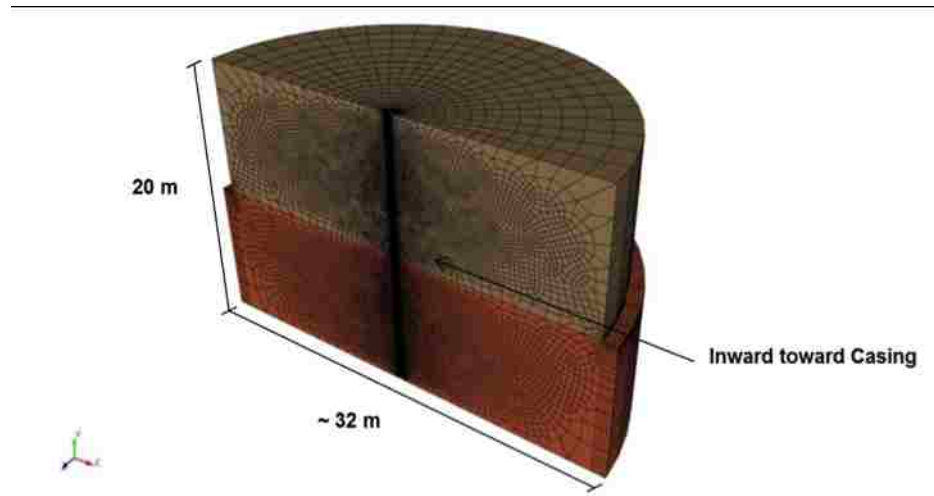
Figure A.1: Simplified mesh used to develop and test simulation code

parting along a bedding plane cutting through the well axis. The interface is treated as a slip surface at the top or bottom of a layer. The two rock formations subject to slippage and the associated wellbore cement, steel, and epoxy system are highlighted in figure A.2. Vertical profiles of predicted Von Mises stress and equivalent plastic strain (EQPS) are shown in figures A.3 and A.4.

Additional studies were performed by inserting Kayenta constitutive model cement material parameters inside of the microannulus region, creating a perfect bond between the steel and cement interfaces. Under the loading conditions of the slipping bed rock system, stress at the cement/casing interface is greater when the yield stress of cement is low as shown in figures A.5 and A.6. This second wellbore model contains a similar steel casing and cement-or-epoxy annulus representation for an entire length of borehole that matched the 100-m-spaced borehole columns of the field-scale model.

Model results indicate that an epoxy filled microannulus does not reach yield stress whereas a cement microannulus experiences considerable yield which may lead to failure. Thus, under these conditions, a microannulus repaired with an epoxy

based material would be able to better withstand wellbore conditions, suggesting improved zonal isolation. The next step in this analysis process is to transfer the computed stress, strain, pore pressure, and displacement histories for each borehole column in the field-scale model to the wellbore-scale model to evaluate the effects on the cement and nanocomposite epoxy. Kayenta mechanical properties will be developed for the epoxy from the suite of laboratory bench-scale tests that are still in progress.

Appendix A. Bed Slipping Rock Formation
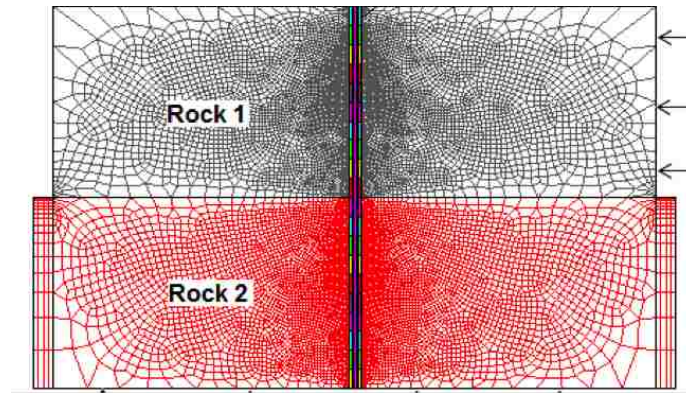
(a)
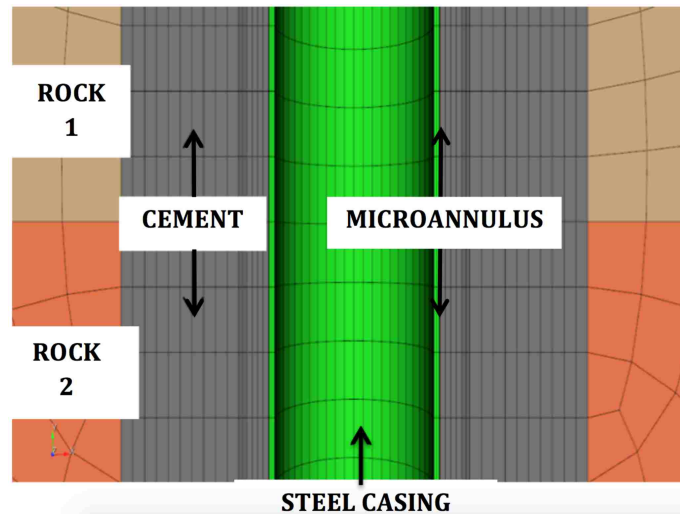
(b)

(c)

Figure A.2: The mesh includes well casing, cement sheath, open annular region, and rock formation. The open annular region or microannulus can represent a flaw (annular gap), intact cement, or epoxy.
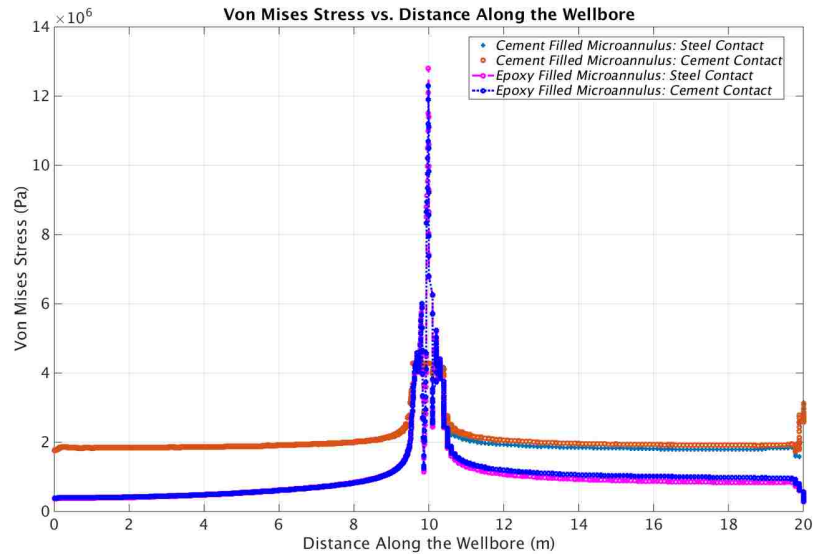
Figure A.3: Von Mises Stress results plotted along the wellbore microannulus. The cases presented include the microannulus filled with cement and epoxy, analyzed on their respective contact surfaces.
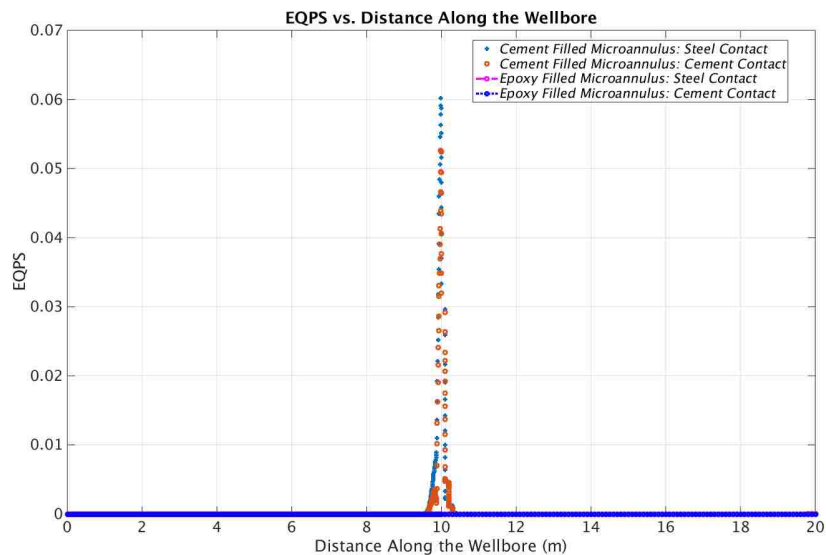
Figure A.4: Equivalent Plastic Strain (EQPS) results plotted along the wellbore microannulus. The cases presented include the microannulus filled with cement and epoxy, analyzed on their respective contact surfaces.
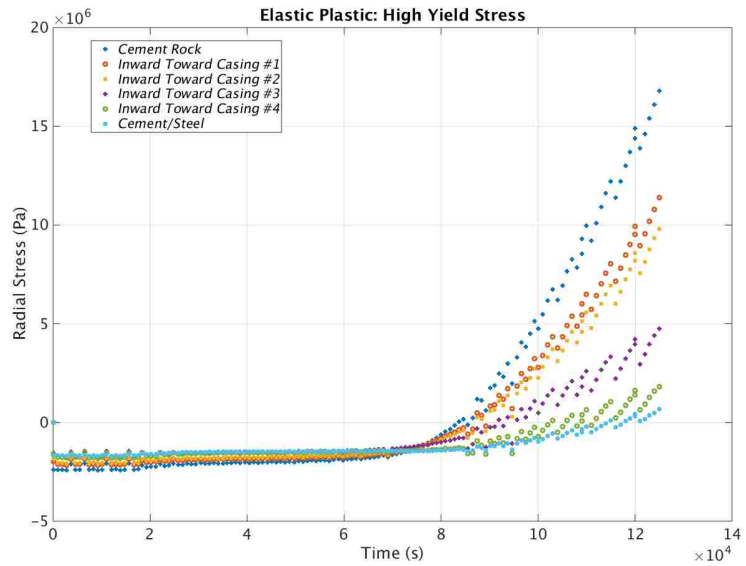
Figure A.5: Modeling results under elastic-plastic conditions with a cement microannulus for a cement with a high yield stress.
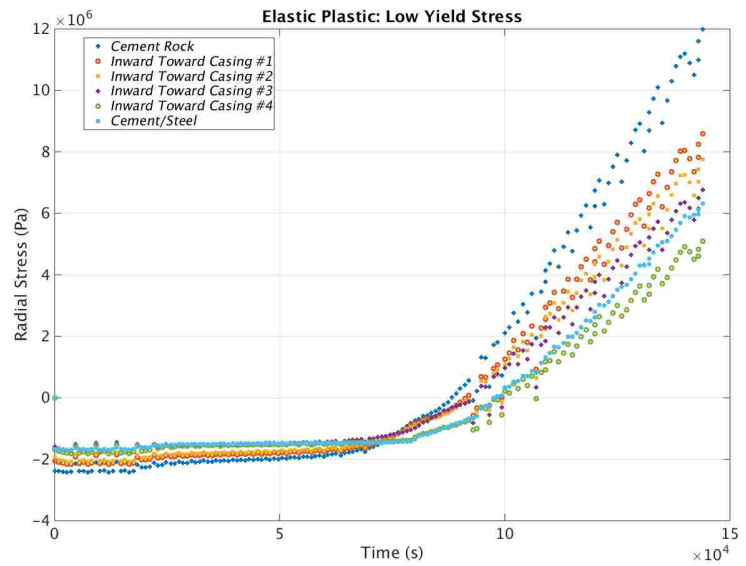
Figure A.6: Modeling results under elastic-plastic conditions with a cement microannulus for a cement with a low yield stress, indicating the importance of the yield stress model employed.

Appendix B

Stress Characterization

Principal stress components are often portrayed in such a way that they are independent of a coordinate system and therefore unaffected by coordinate transformation as means to describe modes of failure surfaces. These states of stress are known as stress invariants and are shown in equations B.4, B.5, and B.6. The physical interpretation of the stress invariants is such that I_1 is related to the average of the three normal stresses (hydrostatic component), I_2 is related to Von Mises Stress as a deviatoric stress (always positive) , and I_3 is used in relation to the deformation gradient (Brannon et al., 2009).

$$\sigma_{ij} = \begin{vmatrix} \sigma x & \tau xy & \tau xz \\ \tau xy & \sigma y & \tau yz \\ \tau xz & \tau yz & \sigma z \end{vmatrix}$$

Hydrostatic stress tensor:

$$\sigma_{\mathrm{m}} = \frac{1}{3}(\sigma_{\mathrm{x}} + \sigma_{\mathrm{y}} + \sigma_{\mathrm{z}}) \tag{B.1}$$

Appendix B. Stress Characterization

Deviatoric stress tensor:

$$S_{ij} = \begin{vmatrix} \sigma x - \sigma m & \tau xy & \tau xz \\ \tau xy & \sigma y - \sigma m & \tau yz \\ \tau xz & \tau yz & \sigma z - \sigma m \end{vmatrix} \tag{B.2}$$

The principal stress in which the shear stress are zero, therefore only normal stresses remain which leads to the following equation B.3 :

$$\sigma^3 - I_1\sigma^2 + I_2\sigma - I_3 = 0 \tag{B.3}$$

Invariants of the stress tensor I_1, I_2, I_3:

$$I_1 = \sigma_x + \sigma_y + \sigma_z = tr(\sigma) \tag{B.4}$$

$$I_2 = (\sigma_x\sigma_y + \sigma_y\sigma_z + \sigma_z\sigma_x) - \tau_{xy}^2 - \tau_{yz}^2 - \tau_{zx}^2 \tag{B.5}$$

$$I_3 = (\sigma_x\sigma_y\sigma_z - \sigma_x\tau_{yz}^2 - \sigma_y\tau_{xz}^2 - \sigma_z\tau_{xy}^2) + 2\tau_{xy}\tau_{xz}\tau_{yz} = det(\sigma) \tag{B.6}$$

$$J_2 = \frac{1}{6}[(\sigma_x - \sigma_y)^2) + (\sigma_y - \sigma_z)^2) + (\sigma_z - \sigma_x)^2] + \tau_{xy}^2 + \tau_{yz}^2 + \tau_{zx}^2 \tag{B.7}$$

Pure hydrostatic pressure can not affect yield in the cap surfaces described in Mohr-Coulomb and Drucker-Prager, as their surfaces are open. However, a capped

106

or closed yield surface inhibits hydrostatic pressure to induce permanent deformation (Brannon et al., 2009).

Appendix C

Input Deck Highlights

C.1   Model Parameters

C.1.1   General Material Parameters

Elastic Steel

```
begin property specification for material mat_steel_el
    density = 7860.
  begin parameters for model elastic
     youngs modulus = 2.0E11  #200.0 Gpa or 29E6 psi (std
        ↪  for ASTM-A36 structural steel)
     poissons ratio = 0.3
   end parameters for model elastic
  end property specification for material mat_steel_el
```

Elastic Plastic Epoxy

```
begin property specification for material mat_epoxy    #
   ↪   Use Cement for placeholder
  density = 1225 # DOW 1g/ml=1000kg/m3
  begin parameters for model elastic_plastic
    youngs modulus = 19e9  #Pa
    poissons ratio = 0.22
    yield stress = 80E6   # Pa #1.28e8
    hardening modulus = 0.0 # Pa
    beta = 0.5
  end parameters for model elastic_plastic
end property specification for material mat_epoxy
```

Elastic Cement

```
begin property specification for material mat_cem_el
  density = 2030  # kg/m3 STANDARD
  begin parameters for model elastic
     youngs modulus = 4.0E9
    poissons ratio = 0.19
  end parameters for model elastic
end property specification for material mat_cem_el
```

Elastic Plastic Cement

Appendix C. Input Deck Highlights

```
begin property specification for material mat_cem_elpl
   ↪    ##Possibly look into kc_concrete model
   ↪ implementation (grep->lupe)
  density = 2030  # STANDARD
    begin parameters for model elastic_plastic
      youngs modulus = 4.0E9
      poissons ratio = 0.19
  yield stress = 4.277E6 # Pa (620 psi)
  hardening modulus = 0.0 # Pa
  beta = 0.5
  end parameters for model elastic_plastic
end property specification for material mat_cem_elpl
```

C.1.2   Kayenta Material Parameters

The primary Kayenta variables used to describe the cement sheath and joint sets are briefly described as (Brannon et al., 2009):

- B0: linear elastic bulk modulus

- G0: linear elastic shear modulus

- RJS: Joint spacing (meters)

- RKS: Join shear stiffness (Pa/meter)

- RKN: Pa/Meter

- A1: Constant term in the fitting function for the meridional profile: yield stress in shear

110

Appendix C. Input Deck Highlights

- A2: Curvature decay parameter in the fitting function for the meridional profile

- A3: Parameter in the shear limit meridional fit function: Change rate of Elasticity

- A4: High-pressure meridional slope parameter in the fit function

- P0: Value of I1 at the onset of pore collapse for hydrostatic compression of virgin material. This parameter will be negative (compression).

- P1: One third of the slope of a porosity vs. pressure crush curve at the elastic limit

- P3: Asymptote (limit) value of the absolute value of the plastic volume strain. This parameter is approximately equal to the initial porosity in the material and may be inferred from hydrostatic crush data

- T1-T7: Primary rate dependence parameter in the Duvaut-Lions overstress model

- CR: (Prop22, symbol R): Dimensionless shape parameter that allows porosity to affect shear strength. equals the eccentricity (width divided by height) of the elliptical cap function, so it is the ratio. Low number neglects effect

The softening parameters implemented are defined as:

- STRENI: Initial high-pressure strength intercept

- STRENF: Final high-pressure strength intercept

- PEAKI1I: Theoretical initial tensile limit of I_1

- PEAKI1F: Theoretical failed tensile limit of I_1. Failed material with no tensile strength have a value of zero

- SOFTENING: Time to failure parameter. Constant strain-to-failure is implemented by setting the value to 3

- FAIL0: Marks point at which material has lost half of its original stiffness and is halfway between the intact and fully damaged strength capacity

- FAIL1: Softening speed, large value (>30) denotes quick softening or gradual softening if small (<5)

- FAIL2: Constant equivalent strain-at-failure

The joint specific material parameters implemented are defined as:

- CKN: initial joint normal stiffness (stress/length)

- VMAX: maximum joint closure (length)

- SPACE: joint spacing (length)

- SHRSTIFF: joint shear stiffness (stress/length)

- U: the direction normal to the joint

- V: the direction along the joint

- W: perpendicular to both U and V (orthogonal system)

An example of characterizing the joint model parameters for computational modeling:
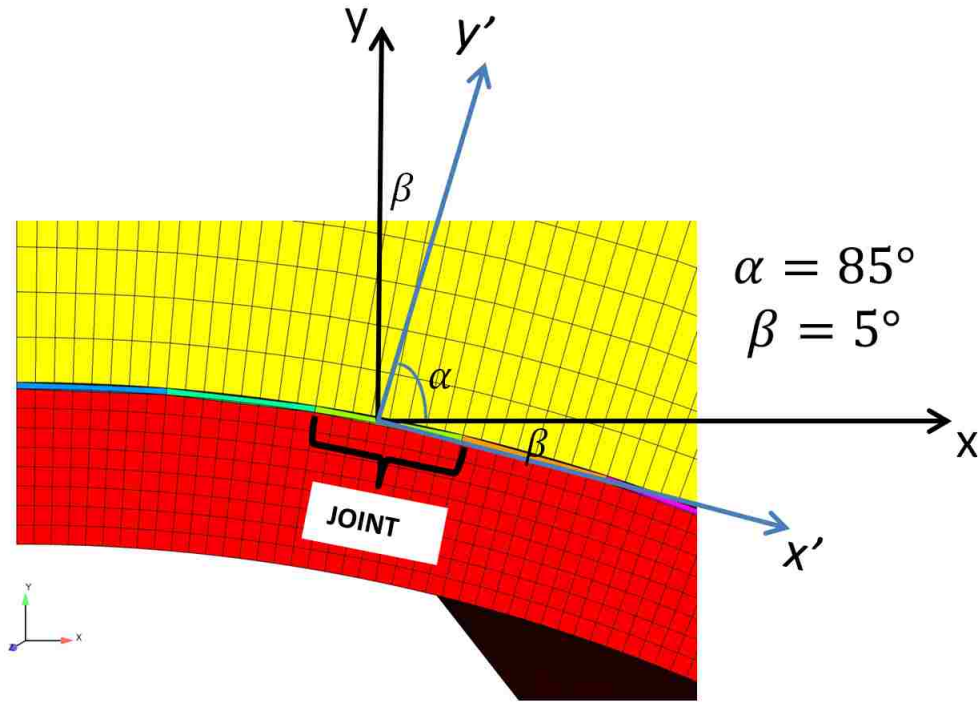
Figure C.1: Geometrical assumptions shown for a unique interfacial fracture element of the joint set

Table C.1: Parametrization shown for the interfacial fracture element of the joint set in figure C.1

Symbol	Value	Units
CKN01	8.62E+10	$\frac{stress}{length}$
VMAX1	1.36E-04	Length
SPACE1	0.000136	Length
U1	cos(85) = 0.08715	N/A
U2	sin(85) = 0.9962	N/A
U3	0.0	N/A
V1	cos(5) = 0.9962	N/A
V2	sin(5) = -0.08715	N/A
V3	0.0	N/A
W1	0.0	N/A
W2	0.0	N/A
W3	cos(85) = 1.0	N/A

Portland Cement

```
begin property specification for material KayentaCement
    density = 2030
    biots coefficient = 1.0 #K << Ks --> ~= 1
#Note: E=(9KG)/(3K+G), K:bulk mod and G:Shear Mod,
#K=1.0954e10,G=7.5434e9-->E=1.84e10
#E=4.0e9, v=0.19 --> G=1680672269 ~1.7E9 Pa K=2150537634
  ↪ ~2.2E9 Pa
#E=7.0e9, v=0.19 --> G=2941176471 , K=3763440860
    begin parameters for model Kayenta
#b0 b1 b2 g0 g1 g2 are elastic parameters
     B0 = 6.0e9  # Pa
    #B0 = 2150537634  # Pa (Elastic Model Equivalent
      ↪ Value)
    #B0 = 1.0954e10  # Pa (Pre-Parametrized Repository
      ↪ Value)
     B1 = 0 # Pa
     B2 = 0 # Pa
     B3 = 0.0 # Pa
     B4 = 0.0 # Dimensionless
     G0 = 4.0e9 # Pa
    #G0 =  1680672269 # Pa (Elastic Model Equivalent
      ↪ Value)
    #G0 = 7.5434e9 # Pa (Pre-Parametrized Repository
      ↪ Value)
     G1 = 0 # Dimensionless
     G2 = 0.0 # 1/Pa
```

```
        G3 = 0.0 # Pa
        G4 = 0.0 # Dimensionless
#a1 a2 a3 a4 and psi are limit surface parameters
        A1 = 4.35e8 #4.26455e8 # Pa
        A3 = 4.2e8 #4.19116e8 # Pa
        A2 = 7.51e-10 # 1/Pa
        A4 = 1.0e-10 # Dimensionless
#p0 p1 p2 are crush parameters
        P0 = -1.95520e8 # Pa
        P1 = 1.2354e-9 # 1/Pa
        P2 = 0.0 # 1/Pa^2
        P3 = 0.01 #0.065714 # strain
        CR = 12.0
        HC = 0.0 # Pa
# t1 through t7 are zero therefore no rate sensitivity
        T1 = 0.0 # sec
        T2 = 0.0 # 1/sec
        T3 = 0.0 # Dimensionless
        T4 = 0.0 # 1/sec
        T5 = 0.0 # Pa
        T6 = 0.0 # sec
        T7 = 0.0 # 1/Pa
        J3TYPE = 3
        A2PF = 0
        A4PF = 0
        CRPF = 0
        RKPF = 1
```

115

```
#adagio_rtest/materials/lame/kayenta/kayenta_fail/
  ↪ kayenta_fail.i
      STRENI = 30E9
      STRENF = 30E6
      PEAKI1I = 1.E+99
      PEAKI1F = 1.E+99
      SOFTENING = 3
      FAIL0 = 1.0 #
      FAIL1 = 0.5
      FAIL2 = 0.1
    End parameters for model Kayenta
  end property specification for material KayentaCement
```

Interfacial Microannulus Joints

```
 begin property specification for material interfacialKay
    density = 2030
    biots coefficient = 1.0 #K << Ks --> ~= 1
    begin parameters for model Kayenta
       B0 = 1.0954e10  # Pa
       B1 = 0 # Pa
       B2 = 0 # Pa
       B3 = 0.0 # Pa
       B4 = 0.0 # Dimensionless
       G0 = 7.5434e9 # Pa
       G1 = 0 # Dimensionless
       G2 = 0.0 # 1/Pa
```

```
        G3 = 0.0 # Pa

        G4 = 0.0 # Dimensionless

        A1 = 4.26455e8 # Pa

        A2 = 7.51e-10 # 1/Pa

        A3 = 4.19116e8 # Pa

        A4 = 1.0e-10 # Dimensionless

        P0 = -1.95520e8 # Pa

        P1 = 1.2354e-9 # 1/Pa

        P2 = 0.0 # 1/Pa^2

        P3 = 0.065714 # strain

        CR = 12.0 # Dimensionless

        HC = 0.0 # Pa

        T1 = 0.0 # sec

        T2 = 0.0 # 1/sec

        T3 = 0.0 # Dimensionless

        T4 = 0.0 # 1/sec

        T5 = 0.0 # Pa

        T6 = 0.0 # sec

        T7 = 0.0 # 1/Pa

        J3TYPE = 3 # Dimensionless

        A2PF = 0

        A4PF = 0

        CRPF = 0

        RKPF = 1
#Reminder: U is the direction normal to the joint
#          V is the direction along the joint
```

```
#            W is perpendicular to both , since we are
  ↪ dealing with the orthogonal system
#CKN = initial joint normal stiffness ( stress / length )
#VMAX = maximum joint closure ( length )
#SPACE = joint spacing ( length )
#SHRSTIFF = joint shear stiffness ( stress / length )
#01 , 02 , or 03 to indicate the joint normal direction


#136 micron microannulus
CKN01 = 8.62 E10

VMAX1 = 1.36 E -4

SPACE1 = 0.000136


#19 micron microannulus
CKN01 = 4.032 E11

VMAX1 = 1.56 E -5

SPACE1 = 0.000019


#100 micron microannlus
CKN01 = 8.62 E10

VMAX1 = 1.36 E -4

SPACE1 = 0.000100



# JOINT 1
U1 = 1.0

U2 = 0.0
```

```
U3 = 0.0
V2 = -1.0
V1 = 0.0
V3 = 0.0
W1 = 0.0
W2 = 0.0
W3 = 1.0
#JOINT2
U1 = 0.9966
U2 = 0.0826
U3 = 0.0
V2 = -0.9966
V1 = 0.0826
V3 = 0.0
W1 = 0.0
W2 = 0.0
W3 = 1.0
#JOINT3
U1 = 0.9864
U2 = 0.1646
U3 = 0.0
V2 = -0.9864
V1 = 0.1646
V3 = 0.0
W1 = 0.0
W2 = 0.0
W3 = 1.0
```

```
#JOINT4
U1 = 0.9694
U2 = 0.2455
U3 = 0.0
V2 = -0.9694
V1 = 0.2455
V3 = 0.0
W1 = 0.0
W2 = 0.0
W3 = 1.0
#JOINT5
U1 = 0.9458
U2 = 0.3247
U3 = 0.0
V2 = -0.9458
V1 = 0.3247
V3 = 0.0
W1 = 0.0
W2 = 0.0
W3 = 1.0
#JOINT6
U1 = 0.9158
U2 = 0.4017
U3 = 0.0
V2 = -0.9158
V1 = 0.4017
V3 = 0.0
```

```
W1 = 0.0
W2 = 0.0
W3 = 1.0
#JOINT7
U1 = 0.8785
U2 = 0.4759
U3 = 0.0
V2= -0.8785
v1= 0.4759
V3 = 0.0
W1 = 0.0
W2 = 0.0
W3 = 1.0
#JOINT8
U1 = 0.8372
U2 = 0.5469
U3 = 0.0
V2 = -0.8372
V1 = 0.5469
V3 = 0.0
W1 = 0.0
W2 = 0.0
W3 = 1.0
#JOINT9
U1 = 0.7891
U2 = 0.6142
U3 = 0.0
```

```
V2 = -0.7891
V1 = 0.6142
V3 = 0.0
W1 = 0.0
W2 = 0.0
W3 = 1.0
#JOINT10
U1 = 0.7357
U2 = 0.6773
U3 = 0.0
V2 = -0.7357
V1 = 0.6773
V3 = 0.0
W1 = 0.0
W2 = 0.0
W3 = 1.0
#JOINT11
U1 = 0.6773
U2 = 0.7357
U3 = 0.0
V2 = -0.6773
V1 = 0.7357
V3 = 0.0
W1 = 0.0
W2 = 0.0
W3 = 1.0
#JOINT12
```

```
U1 = 0.6142
U2 = 0.7891
U3 = 0.0
V2 = -0.6142
V1 = 0.7891
V3 = 0.0
W1 = 0.0
W2 = 0.0
W3 = 1.0
#JOINT13
U1 = 0.5469
U2 = 0.8372
U3 = 0.0
V2 = -0.5469
V1 = 0.8372
V3 = 0.0
W1 = 0.0
W2 = 0.0
W3 = 1.0
#JOINT14
U1 = 0.4759
U2 = 0.8795
U3 = 0.0
V2 = -0.4759
V1 = 0.8795
V3 = 0.0
W1 = 0.0
```

```
W2 = 0.0
W3 = 1.0
#JOINT15
U1 = 0.4017
U2 = 0.9158
U3 = 0.0
V2 = -0.4017
V1 = 0.9158
V3 = 0.0
W1 = 0.0
W2 = 0.0
W3 = 1.0
#JOINT16
U1 = 0.3247
U2 = 0.9458
U3 = 0.0
V2 = -0.3247
V1 = 0.9458
V3 = 0.0
W1 = 0.0
W2 = 0.0
W3 = 1.0
#JOINT17
U1 = 0.2455
U2 = 0.9694
U3 = 0.0
V2 = -0.2455
```

Appendix C. Input Deck Highlights

```
V1 = 0.9694
V3 = 0.0
W1 = 0.0
W2 = 0.0
W3 = 1.0
#JOINT18
U1 = 0.1646
U2 = 0.9864
U3 = 0.0
V2 = -0.1646
V1 = 0.9864
V3 = 0.0
W1 = 0.0
W2 = 0.0
W3 = 1.0
#JOINT19
U1 = 0.0826
U2 = 0.9966
U3 = 0.0
V2 = -0.0826
V1 = 0.9966
V3 = 0.0
W1 = 0.0
W2 = 0.0
W3 = 1.0
#JOINT20
U1 = 0.0
```

```
U2 = 1.0
U3 = 0.0
V1 = 1.0
V2 = 0.0
V3 = 0.0
W1 = 0.0
W2 = 0.0
W3 = 1.0
    End parameters for model Kayenta
  end property specification for material interfacialKay
```

Bibliography

Bandis, SC, AC Lumsden, and NR Barton (1983). "Fundamentals of rock joint deformation". In: *International Journal of Rock Mechanics and Mining Sciences & Geomechanics Abstracts*. Vol. 20. 6. Elsevier, pp. 249–268.

Bear, Jacob (2013). *Dynamics of fluids in porous media*. Courier Corporation.

Bellabarba, Mario, Hélène Bulte-Loyer, Benoit Froelich, Sylvaine Le Roy-Delage, Robert van Kuijk, Smaine Zeroug, Dominique Guillot, Nevio Moroni, Slavo Pastor, and Augusto Zanchi (2008). "Ensuring zonal isolation beyond the life of the well". In: *Oilfield Review* 20.1, pp. 18–31.

Benson, Sally M and David R Cole (2008). "CO2 sequestration in deep sedimentary formations". In: *Elements* 4.5, pp. 325–331.

Bois, Axel-Pierre, Andre Garnier, Francois Rodot, Jeremie Saint-Marc, and Nicolas Aimard (2011). "How to prevent loss of zonal isolation through a comprehensive analysis of microannulus formation". In: *SPE Drilling & Completion* 26.1, pp. 13–31.

Bois, Axel-Pierre, André Garnier, Grégory Galdiolo, and Jean-Benoît Laudet (2012). "Use of a mechanistic model to forecast cement-sheath integrity". In: *SPE Drilling & Completion* 27.02, pp. 303–314.

Bonett, Art and Demos Pafitis (1996). "Getting to the root of gas migration". In: *Oilfield Review* 8.1, pp. 36–49.

BIBLIOGRAPHY

Boresi, Arthur Peter, Richard Joseph Schmidt, and Omar M Sidebottom (1993). *Advanced mechanics of materials.* Vol. 5. Wiley New York.

Brannon, R, A Fossum, and O Strack (2009). "KAYENTA:Theory and User's Guide". In: *Sandia Report.* Vol. 2009-2282. Sandia National Labs, p. 186.

Brearden, William and Robert Lane (1961). "Engineered Cementing Operations to Eliminate WOC Time". In: *Drilling and Production Practice.*

Carey, J William, Kayla Lewis, Sharad Kelkar, and George A Zyvoloski (2013). "Geomechanical Behavior of Wells in Geologic Sequestration". In: *Energy Procedia* 37, pp. 5642–5652.

Ferla, A, A Lavrov, and E Fjær (2009). "Finite-element analysis of thermal-induced stresses around a cased injection well". In: *Journal of Physics: Conference Series.* Vol. 181. IOP Publishing, p. 012051.

Forchheimer, Philipp (1901). "Wasserbewegung durch boden". In: *Z. Ver. Deutsch. Ing* 45.1782, p. 1788.

Gasda, Sarah E, Stefan Bachu, and Michael A Celia (2004). "Spatial characterization of the location of potentially leaky wells penetrating a deep saline aquifer in a mature sedimentary basin". In: *Environmental geology* 46.6-7, pp. 707–720.

Ghabezloo, Siavash, Jean Sulem, and Jérémie Saint-Marc (2009). "Evaluation of a permeability–porosity relationship in a low-permeability creeping material using a single transient test". In: *International Journal of Rock Mechanics and Mining Sciences* 46.4, pp. 761–768.

Gomez, SP, S.R. Sobolik, MN Matteo, JC Stormont, MR Taha, and TA Dewers (2013). "Geomechanical Modeling to Predict Wellbore Stresses and Strains for the Design of Wellbore Seal Repair Materials". In: *American Geophysical Union Fall Meeting 2013, San Francisco, CA, USA.* American Geophysical Union (AGU).

BIBLIOGRAPHY

Gray, Kenneth, Evgeny Podnos, and Eric Becker (2009). "Finite-element studies of near-wellbore region during cementing operations: Part I". In: *SPE drilling & completion* 24.1, p. 127.

Haider, MG, Jay Sanjayan, and PG Ranjith (2012). "Modeling of a Well-bore Composite Cylinder System For Cement Sheath Stress Analysis In Geological Sequestration of CO2". In: *46th US Rock Mechanics/Geomechanics Symposium.* American Rock Mechanics Association.

Horton, Robert L, John W Powell, William E Foxenberg, and David Kippie (2005). *Remediation treatment of sustained casing pressures (SCP) in wells with top down surface injection of fluids and additives.* US Patent 6,959,767.

Iwai, Katsuhiko (1976). "Fundamental studies of fluid flow through a single fracture". PhD thesis. University of California, Berkeley.

Jackson, Robert B (2014). "The integrity of oil and gas wells". In: *Proceedings of the National Academy of Sciences* 111.30, pp. 10902–10903.

Kang, Mary (2014). "CO2, methane, and brine leakage through subsurface pathways: Exploring modeling, measurement, and policy options". PhD thesis. Thesis, Princeton University.

Kang, Mary, Ejeong Baik, Alana R Miller, Karl Bandilla, and Michael Celia (2015). "Effective permeabilities of abandoned oil and gas wells: Analysis of Data from Pennsylvania". In: *Environmental science & technology.*

Klimczak, Christian, Richard A Schultz, Rishi Parashar, and Donald M Reeves (2010). "Cubic law with aperture-length correlation: implications for network scale fluid flow". In: *Hydrogeology Journal* 18.4, pp. 851–862.

Kutchko, Barbara G, Brian R Strazisar, David A Dzombak, Gregory V Lowry, and Niels Thaulow (2007). "Degradation of well cement by CO2 under geologic sequestration conditions". In: *Environmental science & technology* 41.13, pp. 4787–4792.

BIBLIOGRAPHY

Litynski, John T, Scott M Klara, Howard G McIlvried, and Rameshwar D Srivastava (2006). "The United States Department of Energy's regional carbon sequestration partnerships program: A collaborative approach to carbon management". In: *Environment international* 32.1, pp. 128–144.

Liu, Hui-Hai, Jonny Rutqvist, and James G Berryman (2009). "On the relationship between stress and elastic strain for porous and fractured rock". In: *International Journal of Rock Mechanics and Mining Sciences* 46.2, pp. 289–296.

Lomize, GM (1951). "Flow in fractured rocks". In: *Gosenergoizdat, Moscow* 127, p. 197.

Mainguy, M, P Longuemare, A Audibert, and E Lécolier (2007). "Analyzing the risk of well plug failure after abandonment". In: *Oil & Gas Science and Technology-Revue de l'IFP* 62.3, pp. 311–324.

Martinez, Mario J, Pania Newell, Joseph E Bishop, and DZ Turner (2013). "Coupled multiphase flow and geomechanics model for analysis of joint reactivation during CO_2 sequestration operations". In: *International Journal of Greenhouse Gas Control* 17, pp. 148–160.

Matteo, Edward N and George W Scherer (2012). "Experimental study of the diffusion controlled acid degradation of Class H Portland cement". In: *International Journal of Greenhouse Gas Control* 7, pp. 181–191.

Matteo, EN, SR Sobolik, SP Gomez, P Newell, JC Stormont, MR Taha, and Dewers TA (2014). "Modeling the Materials Response of Wellbore Seal Materials during In-Situ Loading". In: *13th Annual Conference on Carbon Capture Utilization and Sequestration, Pittsburgh, PA, USA*. Carbon Capture, Utilization, and Storage (CCUS).

Metcalf, Arthur S, Donald L Purvis, and Shannon Stilwell (2009). "Wellbore re-entries and repairs: practical guidelines for cementing new casing inside existing casing". In: *Drilling contractor* 65.6.

BIBLIOGRAPHY

Nordbotten, Jan Martin, Michael Celia, and Stefan Bachu (2004). "Analytical solutions for leakage rates through abandoned wells". In: *Water Resources Research* 40.4.

— (2005a). "Injection and storage of CO2 in deep saline aquifers: Analytical solution for CO2 plume evolution during injection". In: *Transport in Porous media* 58.3, pp. 339–360.

Nordbotten, Jan Martin, Michael Celia, Stefan Bachu, and Helge Dahle (2005b). "Semianalytical solution for CO2 leakage through an abandoned well". In: *Environmental science & technology* 39.2, pp. 602–611.

Pacala, Stephen and Robert Socolow (2004). "Stabilization wedges: solving the climate problem for the next 50 years with current technologies". In: *science* 305.5686, pp. 968–972.

PetroWiki (2012a). *Remedial cementing.*

— (2012b). *Remedial cementing.*

— (2012c). *Remedial cementing.*

Philippacopoulos, AJ and ML Berndt (2001). "Mechanical property issues for geothermal well cements". In: *Transactions Geothermal Resources Council*, pp. 119–124.

Ravi, K, M Bosma, and O Gastebled (2002). "Safe and economic gas wells through cement design for life of the well". In: *SPE Gas Technology Symposium*. Society of Petroleum Engineers.

Ravi, K, M Bosma, and L Hunter (2003). "Optimizing the Cement Sheath Design in HPHT Shearwater Field". In: *SPE/IADC Drilling Conference*. Society of Petroleum Engineers.

Renshaw, Carl E (1995). "On the relationship between mechanical and hydraulic apertures in rough-walled fractures". In: *Journal of Geophysical Research: Solid Earth (1978–2012)* 100.B12, pp. 24629–24636.

Rocha-Valadez, Tony, A Rashid Hasan, Sam Mannan, and C Shah Kabir (2014). "Assessing Wellbore Integrity in Sustained-Casing-Pressure Annulus". In: *SPE Drilling & Completion* 29.01, pp. 131–138.

Roylance, David (2001). "Pressure Vessels". In: *Department of Materials Science and Engineering, Massachusetts Institute of Technology, Cambridge*.

Rusch, David and Michael Romano (2004). "Internal repair of pipeline leaks using pressure-activated sealant". In: *SPE Eastern Regional Meeting*. Society of Petroleum Engineers.

Rusch, David W, Fred Sabins, and John Aslakson (2005). "Microannulus leaks repaired with pressure-activated sealant". In: *Journal of petroleum technology* 57.1, pp. 58–60.

Sarkar, Sudipta, Nafi Toksoz, and Daniel Burns (2004). *Fluid flow modeling in fractures*. Tech. rep. Massachusetts Institute of Technology. Earth Resources Laboratory.

Shakirah, Saidin (2008). "A new approach for optimizing cement design to eliminate microannulus in steam injection wells". In: *International Petroleum Technology Conference*. International Petroleum Technology Conference.

Shi, Zhifei, Taotao Zhang, and Hongjun Xiang (2007). "Exact solutions of heterogeneous elastic hollow cylinders". In: *Composite Structures* 79.1, pp. 140–147.

SIERRA Solid Mechanics Team (2011). *Sierra/SolidMechanics 4.22 User's Guide*. SAND Report 2011-7597. Albuquerque, NM and Livermore, CA: Sandia National Laboratories.

Souley, M, F Homand, and B Amadei (1995). "An extension to the Saeb and Amadei constitutive model for rock joints to include cyclic loading paths". In: *International journal of rock mechanics and mining sciences & geomechanics abstracts*. Vol. 32. 2. Elsevier, pp. 101–109.

Stormont, JC (2014). *Quarterly Report: Wellbore Seal Repair Using Nanocomposite Materials.* Q4 YR2: Submitted to the U.S. DOE National Energy Technology Laboratory. The University of New Mexico.

Stormont, JC, Ahamd, J Ellison, MR Taha, and EN Matteo (2015). "Laboratory measurements of flow through wellbore cement-casing microannuli". In: *ARMA 15-294, Proceedings of the 49th US Rock Mechanics-Geomechanics Symposium, San Francisco, CA, USA.* American Rock Mechanics Association.

Taha, MR (2015). *Wellbore Seal Repair Using Nanocomposite Materials.* Unpublished raw data. The University of New Mexico.

Teodoriu, Catalin, Christian Kosinowski, Mahmood Amani, Jerome Schubert, and Arash Shadravan (2013). "Wellbore Integrity and Cement Failure at HPHT Conditions". In: *International Journal of Engineering* 2.2, pp. 2305–8269.

Thiercelin, MJ, Bernard Dargaud, JF Baret, and WJ Rodriguez (1997). "Cement design based on cement mechanical response". In: *SPE annual technical conference and exhibition.* Society of Petroleum Engineers.

Ugwu, Ignatius Obinna (2008). "Cement fatigue and HPHT well integrity with application to life of well prediction". PhD thesis. Texas A&M University.

Wang, Wei (2014). "Emergence of Delamination Fractures around Casing and Its Stability". PhD thesis. University of Wyoming.

Witherspoon, PA, JSY Wang, K Iwai, and JE Gale (1980). "Validity of cubic law for fluid flow in a deformable rock fracture". In: *Water resources research* 16.6, pp. 1016–1024.